EPFL

Fluorogenic probes for live-cell imaging

Aleksandar SALIM

École
polytechnique
fédérale
de Lausanne

2020

Acknowledgements

Hello there, dear reader! This part of the thesis is dedicated to expression of my personal gratitude to the people which were part of my PhD journey.

First, I would like to start with a serious expression of gratitude towards my professors, Kai and Pierre. Two intellectual giants that allowed me to train in both of their science bootcamps. Thank you for giving me the chance to develop myself and for believing in me. Kai and Pierre wanted me to learn, among other things, rigor, preciseness and structure. Three words that will haunt me until the end of my stay on Earth. I was obsessed by them. I dreamt of them. Thank you for instilling in me the highest of standards for all of the three. I may still take a long time to reach these, but the trajectory and awareness is there. Also, I would like to thank you both for giving me time to develop in my own pace. I fought many battles during my PhD, and in retrospect I realize that time was the most valuable thing you both offered me. From the bottom of my soul and with a smile on my face, THANK YOU.

Further, I want to thank my lab mates (both Lausannian (both Kai's and Pierre's lab) & Heidelbergish ones) for your scientific help. Darn! You bloody creatures of darkness, I could not have done it without you! Each one of you made my journey to the underground and back much more bearable. Some of you thought me rigor, some preciseness, but no one except Yoda and the Dragon could have taught me structure. Even they gave up many times. Yoda is Helen and the Dragon is Michelle, btw ;). Also, thank you for sharing my successes and pains. Each time I broke myself (yeah that happened several times), you were there to help me pick myself up and rebuild into a better person. Thank you for sharing the depths of bottles and long exhausting nights of bar explorations. Thank you for all long discussions we had, and Qyu and I are sorry if we bored you to death. Thank you for putting up with my blunt and non-filtered humour, aka unsuccessful jokes; #nofilter. And thank you for all of you who managed to come to our wedding, I really hope you had a thoroughly shocking experience. Hopefully, a positive one. Finally, thank you for becoming my friends. Cheesy I know, but that's how I roll, :emoji with fancy glasses with strong beat music in the background:. I really hope nobody reads this.

Thirdly, I want to thank my wife and family. Yes, I have a wife and she is real. And no, the dude I talk to in the toilet is a small gnome from the other world, he just tells me stories about the imaginary world. Yes, my wife, she is awesome! I don't care I'll do it in Serbian; Hvala ti ljubavi što veruješ u mene. Hvala ti što si pored mene. Hvala ti za neprekidne razgovore. Hvala ti za one stvari koje ne smeju biti napisane. Hvala ti si mi najbolji prijatelj i moram priznati da se baš radujem našem zajedničkom životu u tom ludom Londonu. Volim te. I na kraju želeo bih da se zahvalim svojoj porodici; majci, tati, sestri, bratu i bratu. Bez vas nikada ne bih bio na ovom mestu gde pokušavam da živim svoje snove. Tatko, gledajući u tvoju hrabrost našao sam moju da odem u beli svet. Majka uz tebe sam naučio da prihvatim ljude i volim ih punim srcem. Volim vas i hvala vam na tome. Braćo mali šilibajzeri i najdraža sestro, volim vas i uvek ću biti uz vas. I kako bih vas nervirao i kako bih vas gurao. A ponajviše vam želim da nađete hrabrost da se borite sami za sebe. Dragi moji završih ovaj deo puta. Idemo dalje, gradimo. Radujem se novim avanturama.

Abstract

The development of novel fluorogenic probes and their use in live-cell imaging lead to a plethora of discoveries in biological research. Herein I report on novel red fluorogenic probes for live-cell super-resolution microscopy of various cellular organelles.

First, I describe a new silicon rhodamine fluorophore termed SiR595. As most other SiR derivatives, SiR595 exists in an equilibrium between two chemical forms, a fluorescent zwitterion and a non-fluorescent spirolactone. Compared to regular SiR, the equilibrium of SiR595 is shifted towards the non-fluorescent, uncharged spirolactone. When coupled to appropriate targeting ligands, the resulting SiR595-based probes show high cell permeability. Furthermore, SiR595-based probes are fluorogenic as binding to their targets shifts the equilibrium towards the fluorescent zwitterion. I took advantage of these properties to develop novel red fluorogenic probes for live-cell imaging of Halo-tagged proteins, microtubules, F-actin and DNA. I was furthermore able to show that all of these probes are compatible with live-cell STED nanoscopy.

Furthermore, I developed fluorogenic probes for live cell imaging of centrosomes. The centrosome is the principal microtubule-organizing center in animal cells. We targeted polo-like kinase 4 (Plk4), a serine/threonine-protein kinase, which localizes to centrioles throughout the cell cycle. To label Plk4 in live cells, we used Centrinone, a potent inhibitor of Plk4. Conjugating Centrinone to SiR595, I obtained and characterized several fluorogenic SiR595-Centrinone probes. SiR595-Centrinone probe labels overexpressed GFP-Plk4(K41M) during live-cell imaging and could be used to characterize the spatial distribution of GFP-Plk4(K41M) using live-cell STED nanoscopy. While the here introduced probes for Plk4 are not bright and fluorogenic enough to detect endogenous Plk4, the work provides the foundation for the development of such probes.

Keywords

Résumé

Le développement de nouvelles sondes fluorogéniques et leur utilisation en imagerie cellulaire ont conduit à d'innombrables découvertes en recherche biologique. Je présente ici de nouvelles sondes fluorogéninques émettant dans le rouge pour des utilisations en microscopie à haute résolution sur divers organites cellulaires.

Tout d'abord, je décris un nouveau fluorophore de type rhodamine basé sur du silicium et appelé SiR595. Comme la plupart des autres dérivés SiR, SiR595 existe dans un équilibre entre deux formes chimiques : un zwitterion fluorescent et une forme spirolactone non fluorescente. Comparé à la SiR standard, cet équilibre est en faveur de la spirolactone non fluorescente et non chargée pour SiR595. Le couplage chimique de SiR595 à des ligands de ciblage appropriés permet de développer des sondes à haute perméabilité cellulaire. Ces sondes sont fluorogènes: l'interaction avec leur cible déplace l'équilibre vers la forme zwitterionique, fluorescente. Ces nouvelles sondes émettent dans le rouge et permettent d'imager en cellule vivante des protéines fusionnées à Halo, les microtubules, la F-actine et l'ADN. Enfin, j'ai pu montrer que ces sondes sont compatibles avec l'imagerie cellulaire dite STED nanoscopie.

J'ai également développé des sondes fluorogéniques pour l'imagerie du centrosome de cellules vivantes. Le centrosome est le principal centre d'organisation des microtubules dans les cellules animales. J'ai ciblé la kinase de type polo 4 (Plk4), une sérine-thréonine protéine kinase, qui se localise aux centrioles au cours du cycle cellulaire. Pour marquer Plk4 en cellules vivantes, J'ai utilisé la Centrinone, un puissant inhibiteur de Plk4. En combinant Centrinone à SiR595, j'ai obtenu et caractérisé plusieurs sondes fluorogènes (SiR595-Centrinone). En condition de surexpression de GFP-Plk4 (K41M), la sonde SiR595-Centrinone a permis d'imager Plk4 en cellules vivantes et pourraient être utilisés pour caractériser la distribution spatiale de GFP-Plk4 (K41M) par microscopie STED. Bien que les sondes introduites ici pour Plk4 ne soient pas suffisamment brillantes et fluorogènes pour détecter la Plk4 endogène, ces travaux établissent les bases d'un futur développement de telles sondes.

Mots-clés

Fluorophores, Fluorogénicité, Sondes fluorogéniques, Imagerie de cellules vivantes, STED, Centrosomes, Plk4

Contents

1 Introduction

1.1 Fluorescence Microscopy

Optical microscopy has proven to be a very useful tool for the observation of bimolecular structures and processes. Among other microscopy techniques, the expansion of fluorescence microscopy over the last 50 years has revolutionized how researchers observe biological processes and dynamics at the single cell level. Fluorescence microscopy is based on the collection of light emitted by fluorophores that are used to label targets of interest. The development of exogenous fluorescent molecules (see below) allowed observations of targets such as proteins, lipids or ions providing us with a view into complex cellular dynamics.[1-4]

Fluorescent microscopy is intrinsically limited in terms of its resolution. The resolution is defined as the shortest distance between two points that can be distinguished by the observer or a camera. When a light beam is focused on a point object it forms a blurred point-like distribution termed point spread function (PSF). The size of the PSF is limited by the diffraction limit of light (~250 nm in the lateral axis). In recent years, improvement of detector technologies, development of image analysis methods, and discovery of specialized dye properties allowed for the observation of fluorescent signals at sub-diffraction level. Two conceptually different methodologies have emerged as the leading workhorses for imaging below the resolution limit, single-molecule localization microscopy (SMLM) and stimulated emission depletion microscopy (STED).[5-7] The common feature between the two techniques is the control of fluorescent and non-fluorescent state of fluorophores. This allows selective observation of only a subset of fluorophores resulting in an image with higher resolution. SMLM is based on the observation of single-molecule fluorescent emissions originating form stochastic blinking of fluorophores.[8-10] Molecules that are found within sub-diffraction distance are observed at different time points which allows for the calculation of their localization. The localization is determined by fitting the detected spatial distribution of photons. The image is then reconstructed from the determined localizations of each molecule to achieve resolutions of commonly 20-30 nm. The second technique to circumvent the diffraction limit of light is STED. STED uses a doughnut shaped laser to deplete a subset of excited fluorophores to the ground state trough stimulated depletion.[11] In that way only a subset of fluorophores is observed and the fluorescence collected forms an image with resolutions of 30-50 nm in X-Y dimensions. These techniques have revolutionized the way we observe biological processes leading to various discoveries of cellular structures and its dynamics.[5, 12-14]

1.2 Fluorescence

The Jablonski diagram (Fig 1) describes the electronic states of a molecule and transitions between them elicited by the interaction of the molecule with electromagnetic radiation (here mostly in the UV-Vis range). When a fluorophore absorbs light of a defined wavelength electrons are excited from their ground state (Fig 1, S_0) to higher energy electronic states (Fig 1, S_1 or S_2). In each electronic state the electron can be found at different vibrational energy levels (Fig 1, Gray lines). An electron in an excited state can dissipate its energy through various pathways. One part of the electron's energy is rapidly (10^{-12}-10^{-10} s) released through solvent-mediated relaxation (Fig 1, VR) to the lowest vibrational energy level of the first or second singlet electronic state (Fig 1, S_1 or S_2). In addition, the excited electron can relax from a higher excited state (Fig 1, S_2) to a lower excited state (Fig 1, S_1) through internal conversion (Fig 1, IC). A fluorophore in its
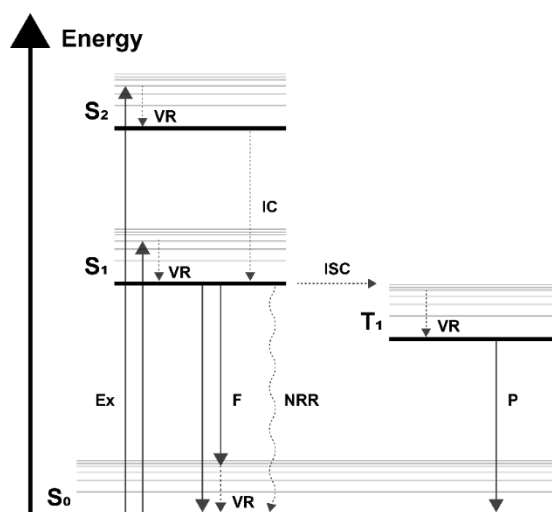
Figure 1. Jablonski diagram depicting different processes that occur upon excitation of a fluorophore. S_0 – ground electronic state; S_1, S_2- Excited electronic states; T_1- Triplet state; Ex- excitation/absorption; F- fluorescence; P- phosphorescence; VR- vibrational relaxation; NRR-

S_1 state can return to the ground state through two main processes, a radiative pathway known as fluorescence (Fig 1, F) and non-radiative relaxation (Fig 1, NRR). During fluorescent relaxation a fluorophore releases the excess of its energy trough emitting a photon of lower wavelength (5-50 nm) than absorbed. The lifetime of this process is in the nanosecond range (10^{-10}-10^{-7} s). The shift between absorbed and emitted light is termed Stoke's shift and is due to loss of energy through rapid vibrational relaxation (Fig 1, VR). The relaxation of fluorophores through NNR pathways does not lead to emission of light. Excited fluorophores can also undergo intersystem conversion (Fig 1, ISC) to a non-fluorescent triplet excited state (Fig 1, T_1). Triplet states are typically high in energy and have long lifetimes (10^{-6} to 10^{-4} s). Relaxation processes from triple states (Fig 1, T_1) to the ground state (Fig 1, S_0) is termed phosphorescence (Fig 1, P) during which the emission of light occurs. Perpetual ISC electron transfers to triple states leads to blinking of the fluorophore due to longer time needed for the triplet state to relax. Also, fluorophores in triple states can undergo different chemical reactions which lead to the irreversible damage of the fluorophore, termed bleaching.[4]

Based on the underlying electronic processes described in the Jablonski diagram, we are able to define physical measures, such as fluorescence lifetime and quantum yield, which are used to characterize fluorescent molecules. Quantum yield represents the ratio of emitted photons over absorbed photons. The fluorescence lifetime is defined as the average time a fluorophore spends in the excited state before it relaxes to the ground state. The perfect fluorophore should have a quantum yield near unity, hence the fluorophore efficiently emits photons. Although, in recent years with the expansion of super-resolution microscopy, researchers use molecule that intrinsically blink for techniques that encompasses single-molecule localization microscopy. Finally, the fluorophore should be chemically sturdy and resistant to oxido-reductive reactions to minimize bleaching of fluorophore. [4, 14]

1.3 Fluorophores

In recent years, the development of novel fluorophores has revolutionized fluorescence microscopy and its use in characterization of biological processes. Many fluorophores are used in fluorescence microscopy such as synthetic organic molecules[14-16], fluorescent proteins[17-20], and nanoparticles[21-22]. In this thesis we will focus on the use of synthetic organic molecules. Fluorophores are characterized by a set of different properties such as absorption maximum, emission maximum, extinction coefficient and quantum yield.[4] The extinction coefficient is defined as the intrinsic ability of the substance to attenuate light at a certain wavelength. It is also connected to the concentration of a solution via the Lambert-Beer law.[4] All of these properties are intrinsic to the structure of the fluorophore and by modifying the structure one can tune them to obtain different properties of fluorophores. The main classes of fluorescent molecules can be separated based on their structural scaffolds that include coumarins, boron dipyrromethene (BODIPY) dyes, fluoresceins, rhodamines, oxazines, and cyanines.[14, 16, 23]

To discuss the spectral properties of the dyes and the effect of structural changes we will use rhodamines as an example. So far, rhodamines were modified by changing the substituents on the aniline part of the xanthene core, by the exchange of the oxygen by other elements and by introducing halogens to the xanthene core.[14, 23] Modification of the anilines on the xanthene core can lead to significant shifts of spectral properties of the dyes (Fig 2 A). Rhodamine 110 (R110, 496/517 nm; ε = 74000 M^{-1} cm^{-1}; Φ = 0.88) and TMR (548/572 nm, ε = 78000 M^{-1} cm^{-1}, Φ = 0.45) are two of the most used dyes of the rhodamine family. One can notice that methylation of the anilines results in a bathochromic shift (an absorbance shift towards higher wavelengths) of ~50 nm (Fig 2A).[23] If the aniline nitrogens are fused with the xanthene core, as it is the case with rhodamine 101 (R101, 574/603 nm, 95000, Φ = 0.45)[24-25], a bathochromic shift occurs for another ~20 nm (Fig 2A). Interestingly, when the oxygen atom in the xanthene core is exchanged by other elements such as carbon or silicon (Fig 2B), significant bathochromic shifts are caused (Fig 2B). In particular, exchanging oxygen in TMR with carbon (carbopyronines (610CP,), 606/626 nm, ε = 121000 M^{-1} cm^{-1}, Φ = 0.52)[26] and silicon (silicon-rhodamines (SiRs), 643/662 nm, ε = 141000 M^{-1} cm^{-1}, Φ = 0.41)[27], leads to a bathochromic shift of ~55 nm and ~95 nm, respectively. Combining these strategies and further optimization of these molecules resulted in the development of exceptionally bright and photostable dyes such as Abberior STAR 635P (**6**) or very far-red shifted dyes such as SiR700 (**7**), which are successfully used in fluorescence microscopy.[28-29]

Besides changing spectral properties, structural modification can lead to change in photostability and the brightness of fluorophores. For example, introduction of CH_2CF_3 to the aniline or fluorine atoms to the 2' and 7' position of the xanthene core of rhodamines leads to increased photostability.[30] Also, beside the spectral shift the fusion of the aniline to the xanthene core leads to better photostability and brightness. Combining these strategies was exploited during the development of dyes such as Abberior STAR 635P that is routinely used in STED microscopy.[31] Finally, the exchange of the dimethyl amino group in TMR with a four-membered azetidine ring can increase brightness and photostability.[32] This strategy was utilized by the Lavis group to develop a whole new spectrum of dyes termed Janelia Fluors.[32-33]
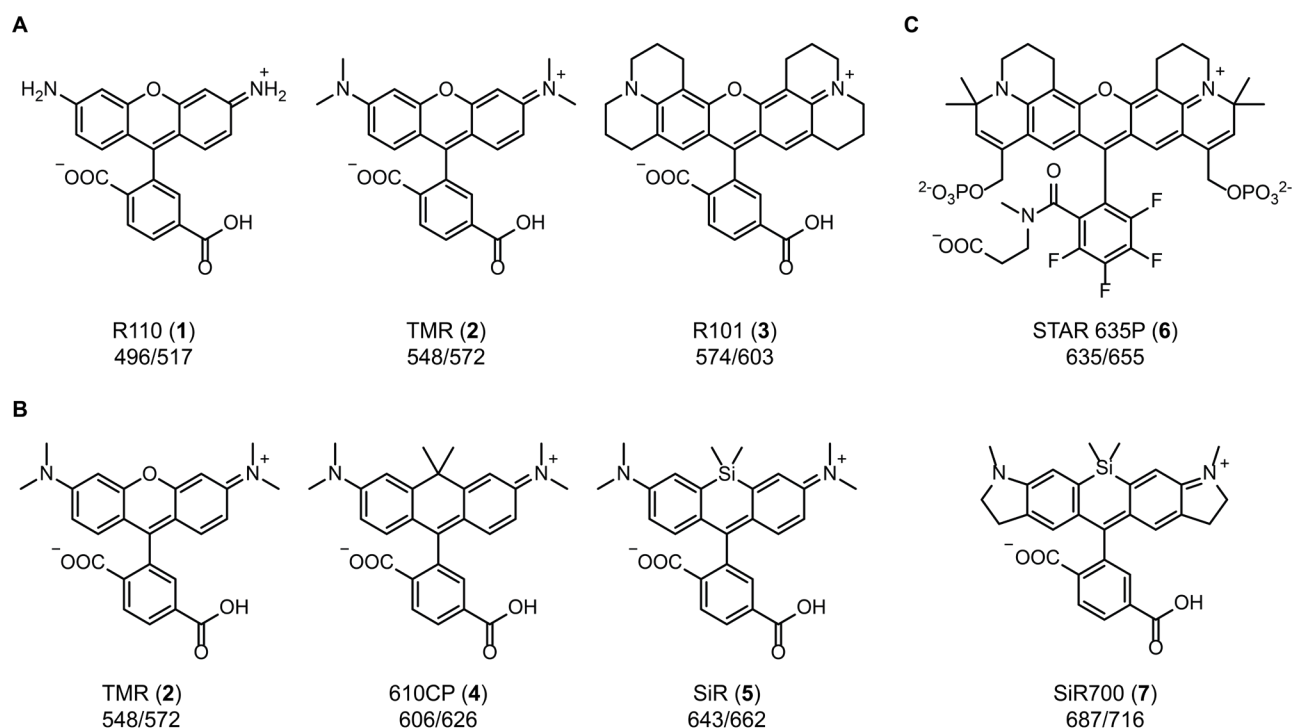
Figure 2. A. The effect of structural modifications on the aniline part of the xanthene core on the spectral properties of rhodamines. **B.** The effect of exchange of oxygen to carbon and silicon on the spectral properties of rhodamine-like dyes. **C.** Representative fluorophores with combined effects discussed in text; The numbers below the name of the dye represent absorption and emission maxima

1.4 Fluorogenicity

Fluorogenicity of fluorophores is defined as the ability to increase the fluorescence signal upon interaction with its target. So far many different strategies have been utilized for the development of fluorogenic fluorophores.[34] Here two main strategies relevant for live-cell labeling are discussed. In the first one, the fluorophore exists in a dynamic equilibrium between a fluorescent and a non-fluorescent form. This equilibrium can be shifted by changing the environment around the fluorophore. To exemplify this the case of SiR650 will be discussed in more detail. SiR650 exists in two forms, the fluorescent and non-fluorescent (Fig 3A).[27] The non-fluorescent form, in which SiR650 forms a spirolactone, is predominant in aqueous solution. The change of environment such as addition of surfactants or interaction of SiR650 with protein surfaces, shifts the equilibrium to the zwitterionic fluorescent form (Fig 3A). By conjugating SiR650 to different targeting ligands one can obtain fluorogenic probes for specific targets (Fig 3B). The spirolactone equilibrium and magnitude of fluorescence increase upon interaction of the probe with its target depends on the probe itself. For example, SiR650-Actin is a probe obtained by conjugating SiR650 to jasplakinolide, a potent actin polymerization inducer.[35] The probe labels F-actin and it has a 100-fold increase of fluorescence upon interaction with its target.[36] Furthermore, it is thought that certain SiR-probes form non-fluorescent aggregates which are believed to quench the fluorescence of SiR650.[37] It is hypothesized that upon interaction of the probe with its target, SiR650 shifts towards the zwitterionic form due to the steric constraints and stabilization by polar protein surfaces (Fig 3C). The binding of the probe also leads to the breakage of aggregates formed by SiR650-probes.[27] Due to their fluorogenicity, the probes have very low background signal during live-cell imagining allowing imaging without prior washing steps.[36] Harnessing these properties, different probes for live-cell imaging have been developed, which includes probes labeling SNAP-tag[27], HaloTag[27], F-actin[36], microtubules[36], DNA[38], lysosomes[28], plasma membrane, endoplasmic reticulum

(ER)[39], Golgi[39] and BACE1[39]. The concept was further exploited on rhodamines, carbopyronines, germanorhodamines and rhodols.[26, 33, 40-41]

Another strategy for generating fluorogenic probes is based on the release of a fluorescence quencher upon the interaction with the target. The quencher such as tetrazine **10** is usually conjugated to the fluorophore and tetrazine can quench the fluorescence through either long-range dipole-dipole interaction or through bond energy transfer.[42-43] Tetrazine can then react with strained alkenes and alkynes, such as **11** which are usually incorporated into proteins of interest (POI) as unnatural amino acids. Upon reaction of tetrazine with the strained alkyne the quenching effect is lost and the fluorescence of the fluorophore is restored. This strategy has its own technical problems such as the low efficiency of incorporation of unnatural amino acids.

A   **Spirolactone equilibrium**   **B**   **SiR650-probe illustration**

Non-fluorescent   **Fluorescent**

C   **Non-fluorescent**   **Fluorescent**

Free fluorogenic probe   **Bound fluorogenic probe**
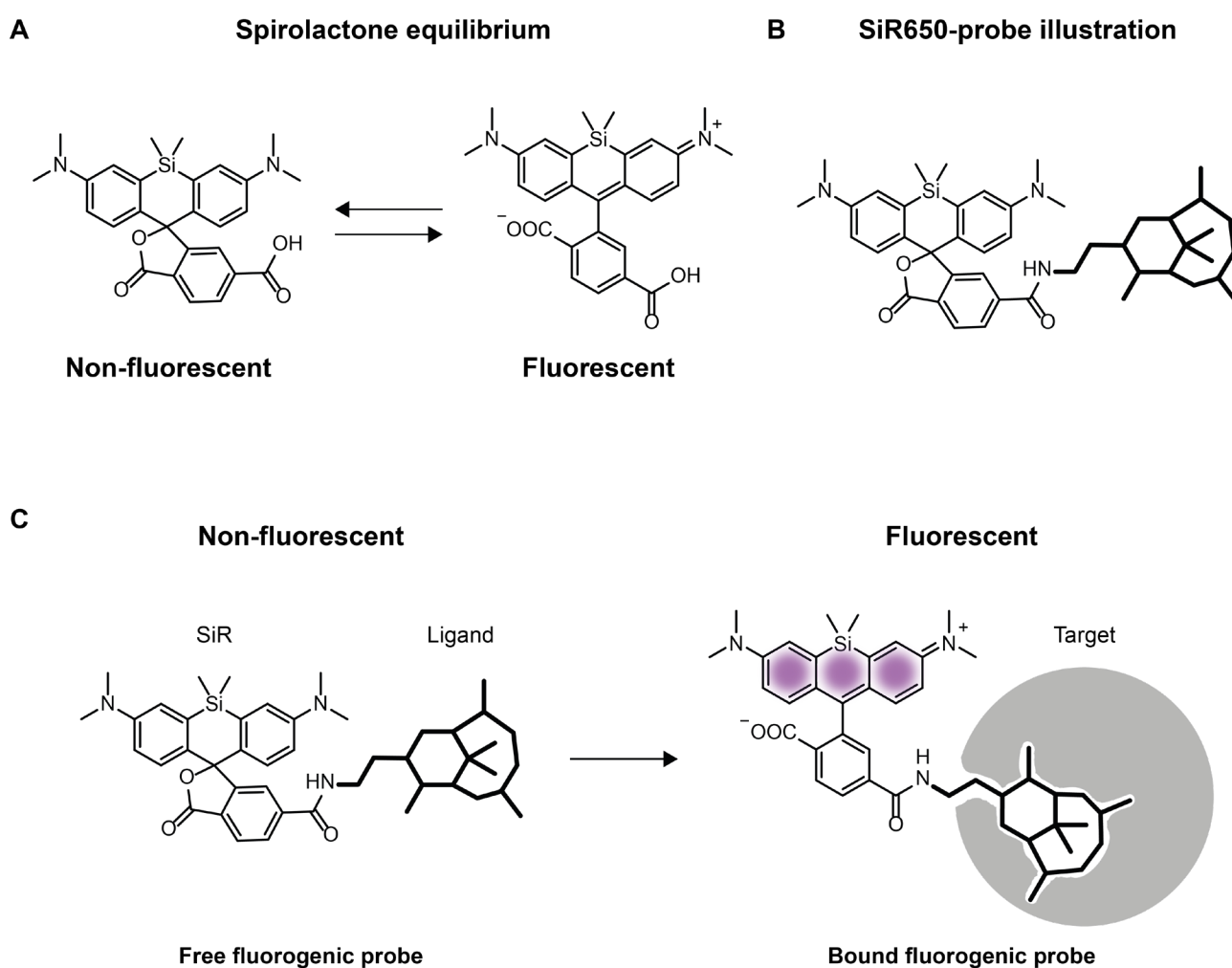
Figure 3. A. SiR650 spirolactone equilibrium between the non-fluorescent and fluorescent form. **B.** Illustration of a SiR650-probe consisted of SiR650 fluorophore, linker and targeting ligand. **C.** Representation of fluorogenic response of SiR650-probe upon binding to the target

1.5   Permeability

One of the main issues of live-cell labeling with organic fluorophores is the permeability of fluorescent probes. These problems are mostly circumvented by fixation of cells and subsequent use of antibody staining protocols to deliver the fluorophore to the target of choice. In addition, different approaches have been developed which allow passage of the fluorescent probes themselves to the intracellular space, such as permeabilization[44], bead loading[45], microinjection and cell squeezing[46]. Nevertheless, these approaches are often invasive and often the best strategy for delivery is to rely on intrinsic cell permeation pathways. The main mechanisms of cell permeation are passive diffusion, active transport and endocytosis pathways (Fig 4).[47] Small organic molecules can permeate cells trough passive diffusion, relying on a concentration gradient between the extracellular matrix and the cytoplasm. Endocytosis as a pathway to the inner cell requires acid tolerant fluorophore probes due to acidification of late endosomal vesicles.[47] If molecules are protonated during the acidification of endosomes, it is hard to achieve an efficient endosomal release. In that case, small molecules are trapped and localized to the late endosomes and lysosomes. In order to maximize the probability of a drug permeating the cell membrane, medicinal chemists have established a set of guidelines known as Lipinski's rules.[48] The drug should not have more than five hydrogen bond donors and no more than ten hydrogen bond acceptors. The molecular weight should be lower than 500 and the partition coefficient (log P (octane/water)) should not be smaller than 5. Finally, the drug should have balanced polarity vs hydrophobicity; polar enough to be soluble in water and hydrophobic enough to permeate the cell membrane. Most fluorophores have been optimized for better photo-physical properties and not for cellular permeability. Fluorogenic fluorophores, such as SiR in its non-fluorescent spirolactone form are highly cell permeable (Fig 4)[49]. This property was harnessed and utilized to develop a variety of cell permeable probes for live-cell imaging (see chapter 1.4).
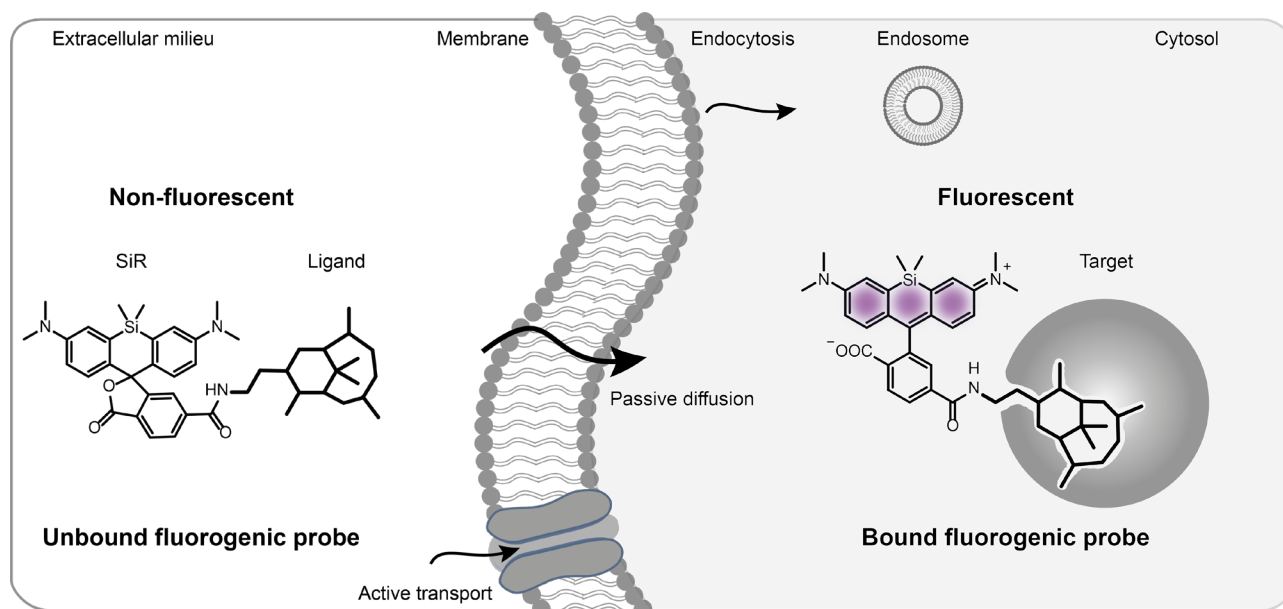
Figure 4. Depiction of the three main cellular uptake pathways of small molecules. Also, a depiction of a SiR650-probe in its spirolactone form permeating to the intracellular matrix followed by interaction with the target and its fluorogenic response.

1.6   Labeling

Conventionally, biologists use antibody labeling techniques to probe and follow processes of their interest. The fixation of cells which is often required during antibody labeling protocols does not allow for temporal observation of the process or the structure of interest. Also, fixation can introduce artifacts of the observed structures leading to false observations.[50] With the development of SRM techniques these problems became even more emphasized due to the higher requirements for precision of labeling. Another common tool for imaging of cellular processes is the use of fluorescent proteins (FPs) that can be genetically encoded and expressed as a fusion protein w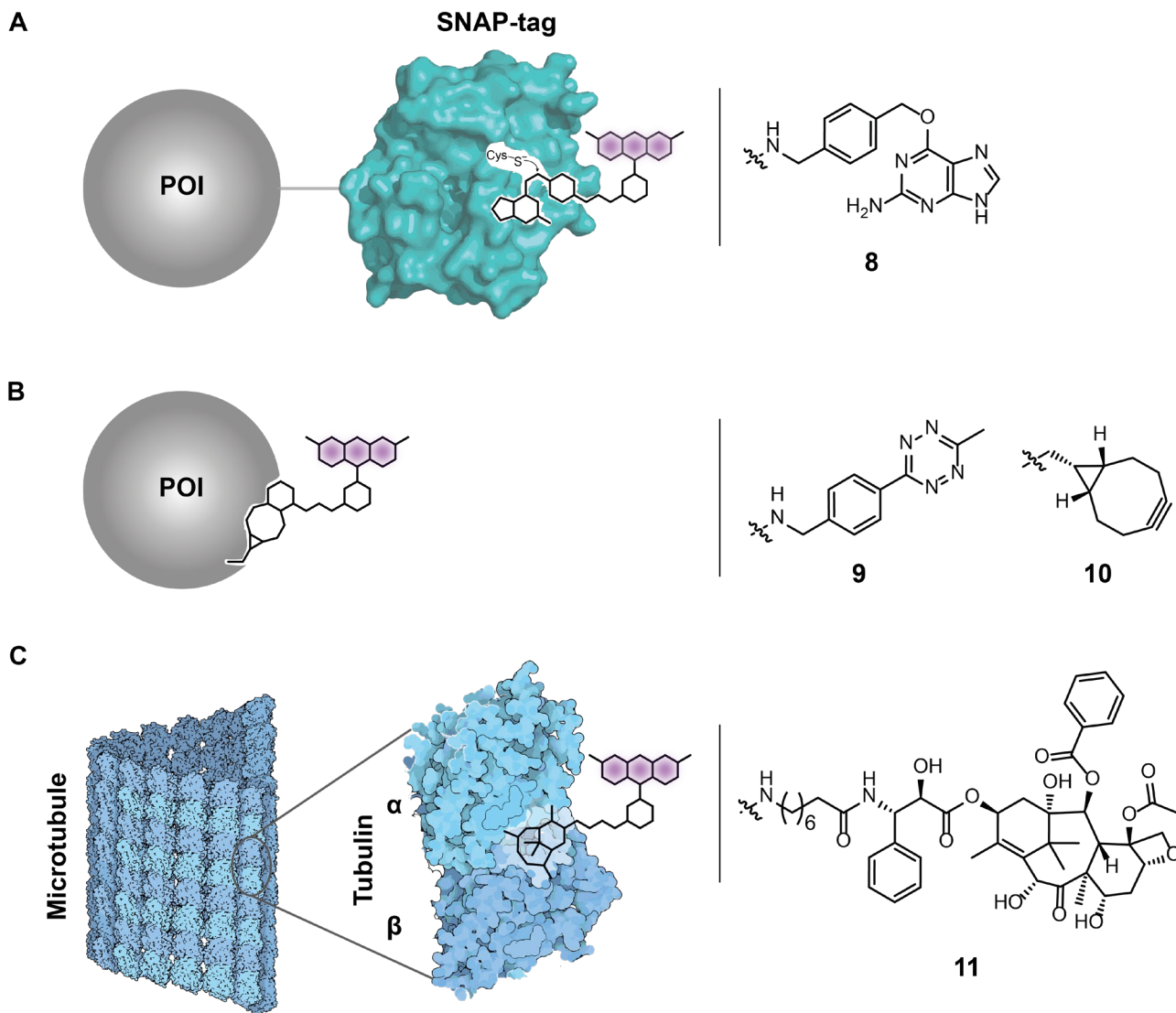ith the protein of interest (POI). Numerous applications of FPs have been reported and their use has transformed the field of cellular biology.[18, 20, 51] Herein we will discuss the use of techniques for labeling with small-molecule fluorescent probes, such as use of self-labeling proteins, small polypeptides and small molecule probes.

The most commonly used approach to label proteins with organic fluorescent probes involves expressing the POI with a small polypeptide or protein (termed tag) as a genetic fusion. These tags undergo a bioorthogonal reaction with the fluorescent probe. SNAP-tag was one of first reported tags that possessed the specificity and the speed of labeling required for live-cell labeling.[52] The mechanism of reaction involves the thiol located in SNAP-tag's active site that can undergo an irreversible reaction with benzyl guanine derivatives resulting in a covalent bond between SNAP-tag and the fluorophore (Fig 5A). Until now, SNAP-tag has been used in various applications resulting in labeling different proteins and different cellular compartments.[53-54] Beside SNAP-tag other protein tags for covalent labeling have been developed, the most used are HaloTag[55] and CLIP-tag[56]. In addition, tags such as eDHFR[57] that can bind to fluorescent probes non-covalently, or systems that utilize enzyme activity such as lipoic acid ligase to transfer the desired label, can be used for fluorescent labeling.[58] One of the disadvantages of using tags is the influence of the tag on the POI. The size of SNAP-tag (20 kDa) and HaloTag (33 kDa) is about 3-4 nm and it can affect the function and localization of POI. Also, one should note that the overexpression of tagged proteins can lead to artifacts such as mislocalization during imaging of the POI.[59] With the recent advances with genome editing one can circumvent overexpression problems by producing knock-in cell lines that express tagged POI at endogenous levels. To avoid the use of large tags, one can use the incorporation of unnatural amino acids into a POI.[60-61] Encoded unnatural amino acids containing a bioorthogonal handle such as strained alkynes **10**, can be incorporated at desired positions in a POI (Fig 5B). The POI carrying the strained alkyne can then react with a suitable reaction partner such as tetrazine **9** that is conjugated to a fluorophore (Fig 5B). This approach gives the freedom of choice for the position of the fluorescent label and the use of unnatural amino acid leads to minimal perturbation of POI. Nevertheless, the use of this method it is still cumbersome and so far it is not used routinely as a method for live-cell imaging.[60-61] In addition, these methods require genetic engineering to obtain labeling of POI which is sometimes not possible or can induce artifacts. Also, the expansion and use of SRM requires more precise and specific labeling. To achieve these requirements and to avoid genetic engineering direct labeling of POI with fluorescent label would be an ideal scenario.

In recent years, the discovery of fluorogenic fluorophores has led to the development of fluorogenic probes that can directly label POIs.[28, 36-38] The probe consists of a ligand, a linker and a fluorogenic fluorophore (Fig 3B). The ligand can be a small molecule that has a high binding affinity as well as good selectivity towards the POI. Also, the optimal ligand should not lose affinity by derivatization and conjugation to a fluorophore. Examples of such ligands are jasplakinolide, a potent inducer of actin polymerization, and docetaxel **11**, a potent microtubule stabilizing agent.[35, 62] These molecules were conjugated to SiR650 to obtain SiR650-Actin and SiR650-Tubulin, powerful fluorogenic probes that successfully label F-actin and microtubules in live-cells

(Fig 5C). So far, a variety of probes have been developed using natural products or synthetic drugs as ligands. The main drawback of this approach is that the binding of the probe to the POI can affect the function of the POI. As mentioned above jasplakinolide is an actin polymerization inducer and docetaxel leads to microtubule stabilization affecting the dynamics of the cytoskeleton in live cells.

Figure 5. A. POI expressed as fusion protein with SNAP-tag labelled with benzyl guanine derivative **8.** SNAP-tag is presented as surface map obtained from PDB: 3KZY. **B.** Representation of POI labelled with tetrazine conjugate to a fluorophore. POI is expressed with unnatural amino acid **10** followed by labelling with tetrazine **9. C.** Small molecule probe binding to microtubules. Small molecule represents a targeting moiety, in this case docetaxel **11**. Microtubule is represented as model obtained from PDB: 3J2U, while α/β subunits of tubulin are presented as surface map obtained from PDB: 1FFX.

1.7   Centrosomes

Centrioles are microtubule-based structures with numerous functions in proliferation, cell division, polarity and signalling[63-64]. Together with its surrounding protein matrix, termed pericentriolar material (PCM), they form a functional organelle called centrosome (Fig 6A).[63-64] Centrosomes are considered to be the main microtubule-organizing centre (MTOC) of animal cells, forming the microtubule-based spindle during mitotic division, when they are located at the spindle poles. Fully mature centrioles can anchor to the plasma membrane during the G1 phase of the cell cycle where they function as basal bodies and can be used as scaffolds to form cilia and flagella.[64] Centrioles are found in most animals and their defects can lead to a range of diseases.[65]
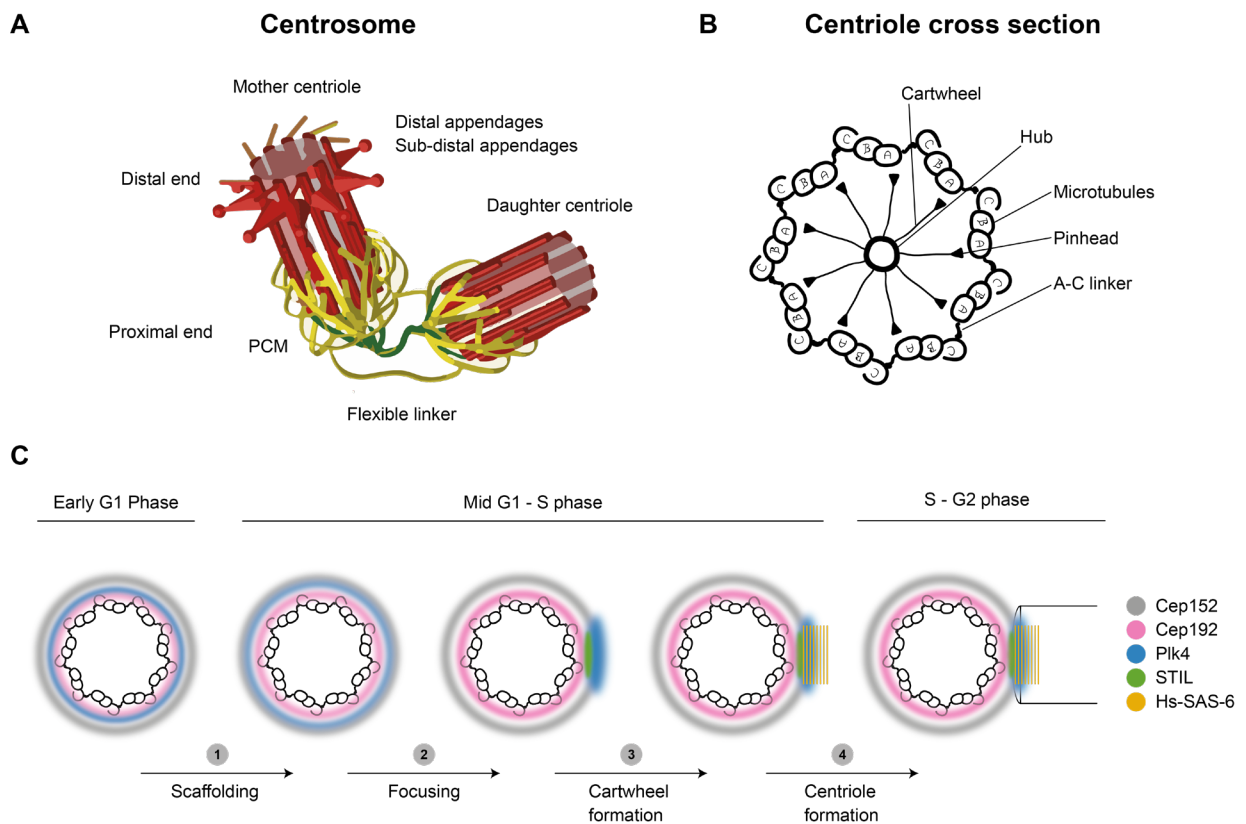
Figure 6. A. Centrosomes consist of two centrioles connected with a flexible linker and surrounded by PCM (adapted from review Silibourne & Bornens, 2010).[66] **B.** Representation of centriole cross section showing proximal microtubule triplets (A, B, C) connected with each other through a A-C linker; a cartwheel consisting of hub, spokes and pinhead made out of HsSAS-6. **C.** A hypothetical model summarizing steps of centriole formation[63-64]

The centrosome consists of two centrioles surrounded by PCM. Centrioles themselves have a barrel like structure, ~500 nm long and ~250 nm wide (Fig 6A).[67] In human cells, the main body of the centriole is built of microtubules; at the proximal (bottom) part nine sets of microtubule triplets are found, and nine sets of microtubule doublets make up the distal (top) part (Fig 6A & B). These microtubules are arranged in a characteristic nine-fold radial symmetry. The microtubule triplet is made out of 13-protofilament A-tubules and 10-protofilament B- and C-tubules, where the A-tubule from one triplet is connected to a C-tubule of another triplet through an A-C linker (Fig 6A & B).[63-64, 68] Also, the distal part of mature centrioles contains subdistal and distal appendages (Fig 6A & B). These appendages are used for centriole anchoring to the plasma membrane to form cilia and flagella.[64]

In proliferating cells, centrioles duplicate once per cell cycle. This is a tightly regulated process and it is synchronized with the cell cycle. During G1 phase of the cell cycle, the cell contains two centrioles (mother and daughter centriole), which are connected by a flexible linker at their proximal parts. The centriole duplication cycle starts during G1/S by the generation of two additional centrioles, initially called procentrioles. They lay perpendicular to the mother and daughter centrioles very near to their proximal end. Procentriole elongation occurs throughout the S and G2 phases, when the newly formed centriole is ~400 nm long. In late G2, the flexible linker that connects the two parental centrioles is lost and two newly formed centrosomes migrate to the opposite sides of nucleus from where they can guide the assembly of the mitotic spindle. During mitosis, each procentriole disengages from its parental centriole and loses its cartwheel. Each centriole pair is then inherited by one daughter cell where a new a flexible linker is formed between the proximal parts of the centrioles to finalize the centriole duplication cycle.[63-64]

1.8 Centriole formation

The centriole is a complex macromolecular structure consisting of many proteins.[69] However, only few proteins play essential roles during the onset of centriole biogenesis; in human cells, these are Cep192, Cep152, Plk4, STIL, HsSAS-6 and CPAP.[63-64]

Centriole biogenesis can be separated into several key steps. Firstly, the scaffold around centriole barrel is formed which leads to recruitment of the Plk4-STIL module (Fig 6C, step 1-2). The Plk4-STIL module forms a single focus from which the cartwheel formation is initiated (Fig 6C, step 3). Following cartwheel formation, the nucleation and elongation of centrioles occurs (Fig 6C, step 4).

The torus encircles the proximal part of the parental centriole and comprises several proteins, among which Cep152/Cep63/Cep57 are known to be most crucial (Fig 6C).[59, 70] First, Cep192 localizes to a barrel around the parental centriole and through its N-terminus interacts with the cryptic polo box (CPB) of Plk4.[71-72] Depletion of Cep192 leads to a severe but not full failure of centriole assembly.[71-72] Cep152 localizes to the torus, encompassing the Cep192-containing barrel at the proximal part of the parent centriole, with its recruitment being promoted by Cep192.[59, 73] One should note that dual depletion of Cep192 and Cep152 prevents the recruitment of Plk4 leading to more severe defects in centriole assembly then depletion of each protein alone .[71-72] Cep152 also binds to the CPB of Plk4, and this dual interaction of Plk4's CPB with Cep152 and Cep192 enables PlK4 to switch scaffolds from the Cep192-containing barrel to the Cep152-containing torus (Fig 6C, step 1).[74] Finally, Cep192 is needed for the presence of Cep152 and PlK4 on the torus, while Cep152 is required for focussing of PlK4 (Fig 6C, step 2).[71-72, 74] This intricate web of interactions allows accurate and timely focussing of Plk4 which is essential for the onset of the centriole biogenesis.

Following the scaffolding step on the proximal part of the centriole, Plk4, STIL and HsSAS-6 play a critical role in the onset of centriole assembly and cartwheel formation (Fig 6C).[63, 75] During the G1/S transition, Plk4 relocalizes from the entire Cep152 torus to focus onto a single point (Fig 6C, step 2).[76] This location is thought to be the site of procentriole formation. This focusing mechanism can be partially explained by tight regulation of Plk4 levels (see below).[66] Also, it is thought that Plk4 interaction and phosphorylation with STIL enables the formation of a single focus of Plk4 during the onset of centriole biogenesis (see below). These fine-tuned interactions allow for the successful formation of a Plk4-STIL module that builds a platform for binding of HsSAS-6 and subsequent cartwheel formation (Fig 6C step 3).

HsSAS-6 comprises a globular domain on the N-terminus, a long coil-coil domain and an unstructured region at the C-terminus.[77-78] It forms homodimers that can oligomerize to form a ring (diameter of ~22 nm) with

nine spokes that emerge from the ring with an angle of ~40°.[77-78] These assemblies are considered to be the building blocks of the cartwheel and the fact that HsSaS-6 self-assembles into these oligomers is thought to be critical for the nine-fold radial symmetry of centrioles.[77-78] The ring assemblies then stack onto each other to form the cartwheel, perpendicularly to the proximal part of the parent centriole.[63-64] The thickness of one ring is ~ 4.5 nm in height, while cryo-electron microscopy (EM) studies of *Trichonympha*'s centriole show that the spacing of the rings in the cartwheel is ~8.4 nm.[77-79] Also, *in-vitro* reconstitution of *Chlamydomonas reinhardtii* CrSAS-6 assemblies show the same vertical spacing.[80] Interestingly, work with *Chlamydomonas* SAS-6 suggest that the cartwheel only partially determines the nine-fold symmetry of centrioles, and it is believed that the A-C linker is also involved in setting the nine-fold symmetry.[81]

Once the cartwheel is made, CPAP together with its binding partners Cep135, Cep120 and SPICE1, are involved in the regulation and assembly of the centriolar microtubule wall (Fig 6C, step 4).[63] CPAP is thought to play a key role in regulating the length of the centriole.[82-84] CPAP interacts with Cep135 and together they interact with the wall of centriolar microtubules.[85] The overexpression of CPAP and its binding partner Cep120 leads to the formation of overelongated centrioles.[83, 86] CPAP also interacts with microtubules through two domains. One of these is a 20-amino acid long so-called SAC domain that can interact with β-tubulin found in microtubules.[87-88] It is thought that this SAC domain caps the microtubules and serves as a control mechanism ensuring slow growth of centriolar microtubules[87-88]

The final step of centriole formation is the recruitment and formation of microtubules. Centriolar microtubules are exceptionally stable in comparison to the cytoplasmic microtubules. The cause of such stability of centriole is not fully understood, although it is hypothesized that it is due to extensive posttranslational modifications of α/β-tubulin, such as polyglutamination and acetylation.[89-90]

1.9   Polo-like kinase 4

One of the most important proteins involved in centriole biogenesis is Polo-like kinase 4 (Plk4), also termed SAK, a serine/threonine protein kinase that belongs to the family of polo-like kinases (Plk).[66, 91] Plk4 has 970 amino acids and consists of an N-terminal kinase domain followed by two polo boxes located towards the C-terminus (Fig 7). Such topology is characteristic for the Plk family, and the polo boxes usually serve as targeting determinants as well as regulators of kinase activity. In the case of Plk4, one polo box is larger and it is termed crypto polo box (CBP) and consists of two polo boxes(Fig 7).[66, 91-92] The CBP has multiple functions, such as roles in dimerization, localization and substrate determination of Plk4. [66, 91]
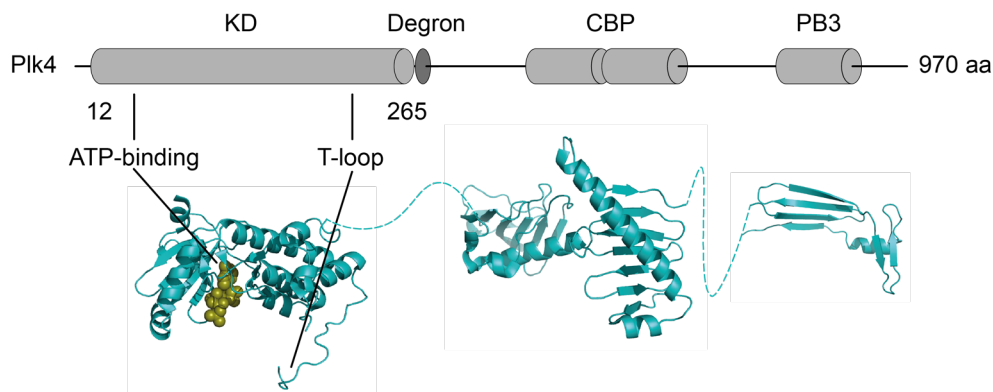
Structural representation of Plk4

Figure 7. Structural representation of Plk4 with crystal structures of different protein parts. KD – Kinase domain (PDB: 3COX), CBP-Crypto-polo box (PDB: 4N9J), PB3- Polo-box 3 (PDB: 5lhy).

Probably because Plk4 has a key role in the onset of centriole formation, its activity and protein amounts are tightly regulated. Through the CPB domain, Plk4 forms a homodimer.[93] The kinase domain of one Plk4 molecular phosphorylates the serine and/or threonine of another one through trans-autophosphorylation.[93] These amino acids reside in the degron region of Plk4. These phosphorylations generate a binding site for the ubiquitin ligase complex member β-TrCP, that subsequently ubiquitinates Plk4, which thus becomes targeted to the proteasome for degradation.[94-97] Mutation of serine and/or threonine to alanine prevents phosphorylation in this region, and subsequently interferes with binding of ubiquitin ligase, leading to a more stable form of Plk4. The consequences of this are higher concentrations of Plk4 at centrosomes, which leads to centriole amplification in cells.[95-96, 98] To reduce degradation of Plk4, cells can counteract its activity by expression of a protein phosphatase 2A as found in *D. melanogaster*.[99] Throughout the cell cycle, phosphatase 2A activity fluctuates and has the highest activity during mitosis, during which Plk4 is stabilized by its interaction with phosphatase 2A enabling its function during cell division.[99] These findings suggest that the amounts of Plk4 need to be tightly regulated and it is highly dependent on its trans autophosphorylation activity and of that of phosphatase 2A.

Upon the scaffolding event (see previous section), Plk4 interacts with STIL's coil-coil domain through its PB3 and linker 1 region.[100] This interaction induces trans-autophosphorylation of Plk4 at the kinase's activation loop.[101] The activation of Plk4 leads to degradation of the excess Plk4, in a feedback loop. The Plk4 that was previously localized as a ring around centriole now forms a dot-like shaped signal following STIL-Plk4 interaction.[102-103] Upon binding of Plk4 to STIL, Plk4 phosphorylates the STAN motif of STIL.[102, 104-105] These phosphorylation events eventually allow binding of HsSaS-6 followed by formation of the centriolar cartwheel.[102, 104-105]. An interesting question that follows is how STIL and Plk4 coexist throughout centriole onset and formation regardless to the STIL's activation of Plk4. One possible explanation is that the PLK4– STIL interaction protects Plk4 from degradation by interfering with β-TrCP recognition and/or phosphorylation of its degron motif.[75] Supporting this hypothesis, overexpression of STIL leads to multiple centrioles forming around the mother centriole.[76, 100] In such circumstances, Plk4 forms a ring around the mother centriole. Plk4 ring formation also occurs when STIL is overexpressed as a mutant that lacks the STAN domain, even though amplification of centrioles is not triggered in this case.[76, 100] These findings indicated that STIL is sufficient to stabilize Plk4 and seems to ensure the high activity of Plk4 that is needed for the onset of centriole biogenesis.[75]

Finally, the mechanism of symmetry breaking of Plk4 towards one focus is still not fully understood. As discussed before, one model suggests that STIL protects the active Plk4 from its degradation which allows the formation of single focus. Another model suggests that the ability of Plk4 to self-organize into supramolecular assemblies protects Plk4 from its degradation. [103, 106] Also, the location choice for the focus formation is assumed to be random, although this is still not clear. Hence, further investigations on mechanisms that govern these processes are required.

2 The aims of the thesis

The objective of this project was to develop fluorogenic probes for live-cell labeling of organelles. We were interested in developing ligand-based probes for direct labeling of proteins and organelles as exemplified by SiR650-Tubulin and SiR650-Actin. We approached this challenge from two different directions. On the one hand we worked on novel fluorogenic fluorophores in a spectral region distinct from SiR650. On the other hand, we sought to develop probes for previously inaccessible targets.

The molecule SiR595 was discovered in our lab and we sought to characterize and understand its peculiar spirolactone equilibrium and investigate how we could harness its properties for the development of novel probes. We aimed to develop probes that would complement the available SiR650 probe family but would nonetheless be compatible with live-cell SRM techniques.

The centrosome as one of the crucial organelles involved in microtubule nucleation represents an interesting target. A live-cell fluorogenic probe for centrioles or centriolar proteins could enable to study this organelle in live-cells in greater detail than previously possible. In the first part of the project we identified a suitable small molecule inhibitor that targets a centriolar protein. We focused on Plk4 as a target and as targeting ligand we used a potent Plk4 inhibitor (Ki = 0.6 nM) named Centrinone .[107] Based on Centrinone we aimed to synthesize fluorogenic probes that are able to label Plk4 in live cells. Due to the near sub-diffraction dimensions of centrioles it is crucial that the developed probes are compatible with SRM techniques. The final part of the project was to use these probes and observe Plk4 localization and dynamics throughout the cell cycle.

3 Silicon-Rhodamine 595

The development of fluorogenic probes has revolutionized the way we observe biological processes in live cells. Hence development of novel fluorogenic fluorescent molecules, as well as fluorogenic probes is of high importance for further development of live-cell imaging as discussed in Introduction. Herein we report the novel fluorogenic molecule termed silicon-rhodamine595 (SiR595) as well as full characterization of this molecule. Furthermore, we report novel fluorogenic probes derived from SiR595 labelling F-actin, microtubules, DNA in live-cells.

3.1 SiR595-6'-COOH

SiR595-6'-COOH (**14**) was synthesized by using the synthetic route depicted in Scheme 1. Compound **12**, which was obtained from a commercial partner (AAT Bioquest, >95%), was reacted with iminodibenzophenone using standard Buchwald coupling reaction conditions to obtain compound **13** in 65 % yield. Compound **13** was further deprotected and hydrolysed in TFA containing 5 % of water to obtain SiR595-6-COOH (**14**) in 77 % yield.
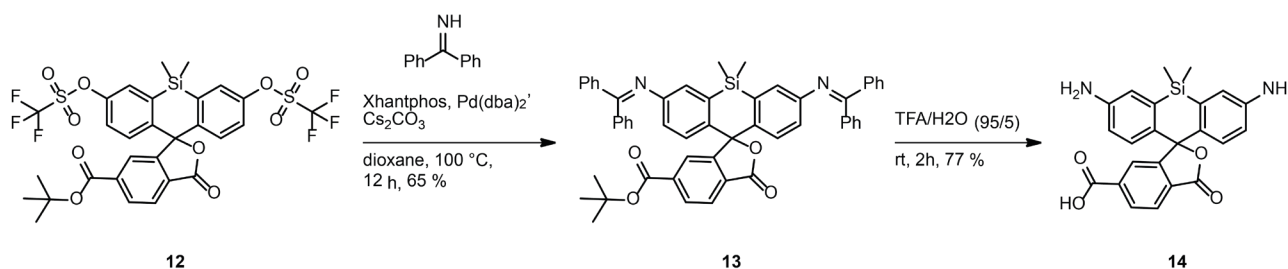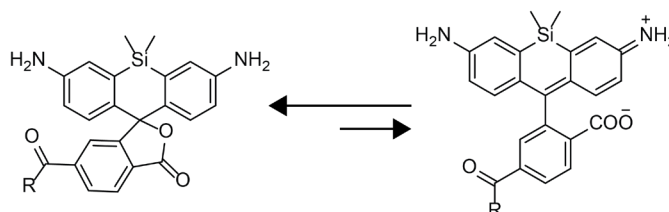

Scheme 1. Synthetic route to SiR595-6'-COOH (**14**)

Following the synthesis, we examined the spectral properties of SiR595. SiR595 exhibits extinction and emission maxima at 590 nm and 615 nm, respectively (Fig 8B and C). Extinction coefficient and quantum yield were measured to be 75000 M^{-1} cm^{-1} and 0.50, respectively (Fig 8B). Fluorescence life time of the dye is in the region of 3.2-3.5 ns measured under three different conditions (Fig 8B). The measured properties of SiR595-6'-COOH were comparable with reported dyes used in this spectral region.[14, 23, 36] Furthermore, because of structural similarities with previously reported rhodamine-like dyes, we assumed that SiR595-6'-COOH exists in solution in spirolactone equilibrium.[27] We also hypothesized that the free aniline groups on the xanthene part would lead to a shift of the equilibrium toward more closed non-fluorescent form (Fig. 8A). Absorbance spectra measurements indicated that SiR595-6'-COOH is indeed fully closed in Tris buffer (pH = 7.4), as well as in the presence of SDS. Surfactants such as SDS or CHAPS have previously been reported by us and others[36, 108] to shift the spirolactone equilibrium of rhodamine-like dyes to the open form. Since the presence of SDS did not allow a full shift to the open form, we used acidified ethanol with 0.1 % TFA (Fig. 8C).[108] Next we used dioxane titrations to assess the effect of the dielectric constant of the solvent on the spirolactone equilibrium of SiR596-6'-COOH. Dioxane titrations (Fig. 8D) indicated that SiR595-6'-COOH's spirolactone does not open in pure water which has the highest dielectric constant in our experiments. These findings corroborate the hypothesis that SiR595-6'-COOH is predominantly found in its non-fluorescent closed form. Previously reported fluorogenic dyes were aimed to have dielectric constants in the region of SiR650 ($D_{0.5}$ ~ 60) which was hypothesized to be essential for the fluorogenicity of dyes. In contrast, we speculated that more closed spirolactone form would yield lower background during live-cell imaging as well as better cell permeability. We speculated that if SiR595 is found in probes, the conformational constrains

upon binding of these probes to the target protein would still lead to spirolactone opening. This concept was harnessed and expanded in our lab with a recently published paper.[109] To further investigate this hypothesis and the utility of SiR595-6'-COOH we have synthesized probes aiming to label HaloTag, SNAP-tag, F-Actin, microtubules and DNA. During the preparation of this thesis Lavis lab have reported SiR595 and our results are in accordance with the reported data.[110]

A

Silicon-Rhodamine 595

Spirolactone equilibrium

B

	λ_{max} abs (nm)	λ_{max} em (nm)	E_{max} (M^{-1} cm^{-1})[1]	D_{50}[2]	τ (ns)[3]	QY[1]
SiR595	595	620	75000	0	3.2/3.3/3.5	0.5
SiR650	652	667	120000	59	2.6/3.0/3.2	0.4

[1] E_{max} was measured in ethanol in presence of 0.1 % TFA; [2] Dioxane titrations were performed with 3 µM solution of the dye
[3] Fluorescence lifetime measurements of 200 nM dye solutions were made in TBS / TBS with 0.1 % SDS/ EtOH with 0.1 % TFA, respectively.

C

Excitation & Emission spectra of SiR595 & SiR650

D
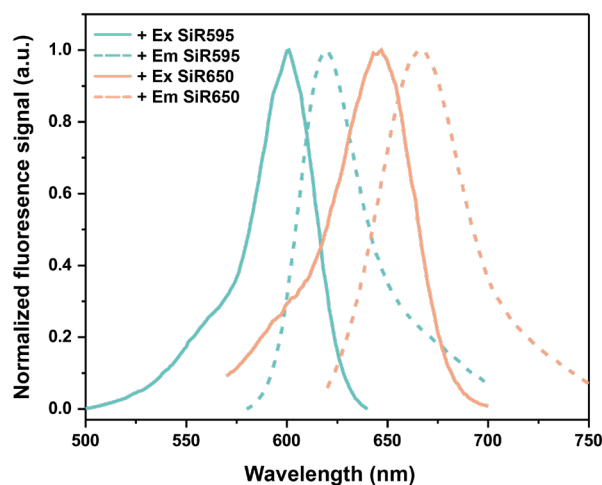
Dioxane titrations of SiR650 and SiR595

Figure 8. A. Spirolactone equilibrium of SiR595-6'-COOH; **B.** Table of photophysical characterization of SiR595-6'-COOH and SiR650-6'-COOH. **C.** Extinction and emission spectra of SiR595-6'-COOH; **D.** Dioxane titrations of SiR595-6'-COOH and SiR650-6'-COOH.

3.2   SiR595-Halo

SiR595-Halo **17** was synthesized by amide coupling (Scheme 2). SiR595-6'-COOH **14** was activated by employing TSTU followed by reaction with previously deprotected HaloTag ligand **15** to obtain SiR595-Halo **16** in 55 % yield.

Scheme 2. Synthetic route to SiR595-Halo **16** probe

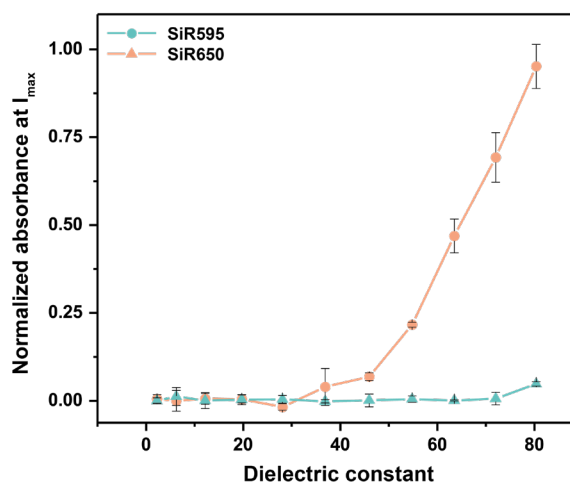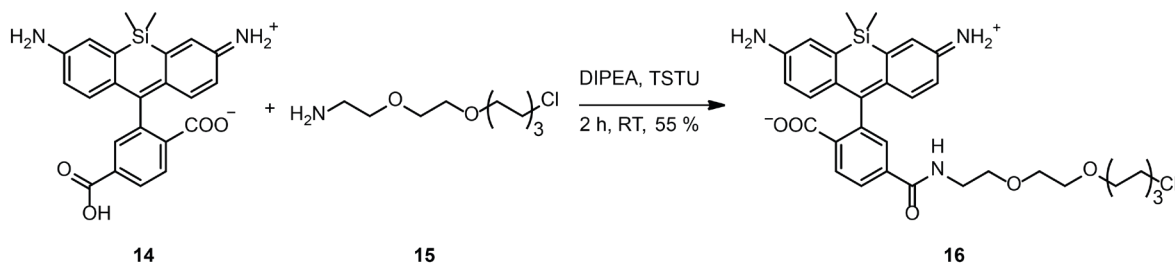First we evaluated the fluorogenicity of SiR595-Halo (Fig 8A). Visible spectra measurements show that SiR595-Halo probe is fluorogenic (Fig 9C) with an absorbance increase of 13-fold upon reaction with HaloTag protein showing that HaloTag protein shifts the spirolactone to an open form of SiR595 (Fig 8A). We also observed that SiR595-Halo spirolactone can be opened in the presence of SDS with an absorbance increase of 17-fold. We speculate that due to the hydrophobic part of halo ligand, SiR595-Halo can anchor itself in formed micelle by SDS (8.2 mM (0.24 %) in water) which leads to the opening of SiR595. Over all SiR595-Halo shows better signal to background ratio than SiR650-Halo (Fig 9C and 9D) which can be attributed to the lower background opening of SiR595-Halo spirolactone. Furthermore, SiR595-Halo was tested for its utility in live-cell imaging by confocal microscopy. We used U2OS cells induced by doxycycline to express Cep41-HaloTag fusion protein. Cep41 is a centrosomal protein and it is reported to localize to interphase microtubules and centrosomes.[111] We incubated SiR595-Halo with U2OS cells expressing Cep41-HaloTag and observed specific fluorescence signal characteristic to microtubules (Fig 9E). These observations show that SiR595-Halo readily passes through the cell membrane and successfully labels HaloTag without significant background during imaging. Next, we measured the fluorogenicity of SiR595-Halo in comparison to SiR650-Halo in live-cell confocal imaging. Doxycycline induced U2OS cells expressing H2B-HaloTag as a fusion protein were incubated with SiR595-Halo or SiR650-Halo in presence of verapamil (Fig 8F). Without prior washout of the fluorophores, we measured florescence signal in the nucleus and beside the nucleus using same size of region of interest (ROI). These measurements indicate that SiR595-Halo has better (61 ± 4) fluorogenic response than SiR650-Halo (42 ± 6) under the tested conditions. Also, due to the low background of SIR595-Halo can be imaged without prior wash. Results are in concordance with *in vitro* visible spectra measurements (Fig 9C & D). Following confocal imaging, using previously described conditions we labelled Cep41-HaloTag with SiR595-Halo and tested the probe's utility in live-cell STED imaging. We successfully imaged labelled Cep41-HaloTag protein bound to microtubules with an average diameter of 72 ± 2 nm (FWHM ± s.e.m., n = 26) of Cep41-HaloTag bound to microtubules. These results are in the expected size region of previous reports of Cep41 labelled microtubule size measured by STED microscopy.[27, 112] According to the cryo-electron microscopy, the size of microtubule is ~25 nm.[113] Mikhaylova et al. reported that using SMLM they measured the average sizes of microtubules labelled with nanobodies (39.3 ± 0.8 nm), only primary antibody (54.0 ± 1.2 nm) and in combination of primary and secondary antibody (61.7 ± 0.8 nm).[112] Hence, we believe that obtained size of microtubules is larger due labelling of protein associated to microtubules and not microtubules itself. Also, due to the large spectral distance from the STED laser (775 nm), the dyes in this spectral region are not depleted efficiently that leads to lower resolution measurements.
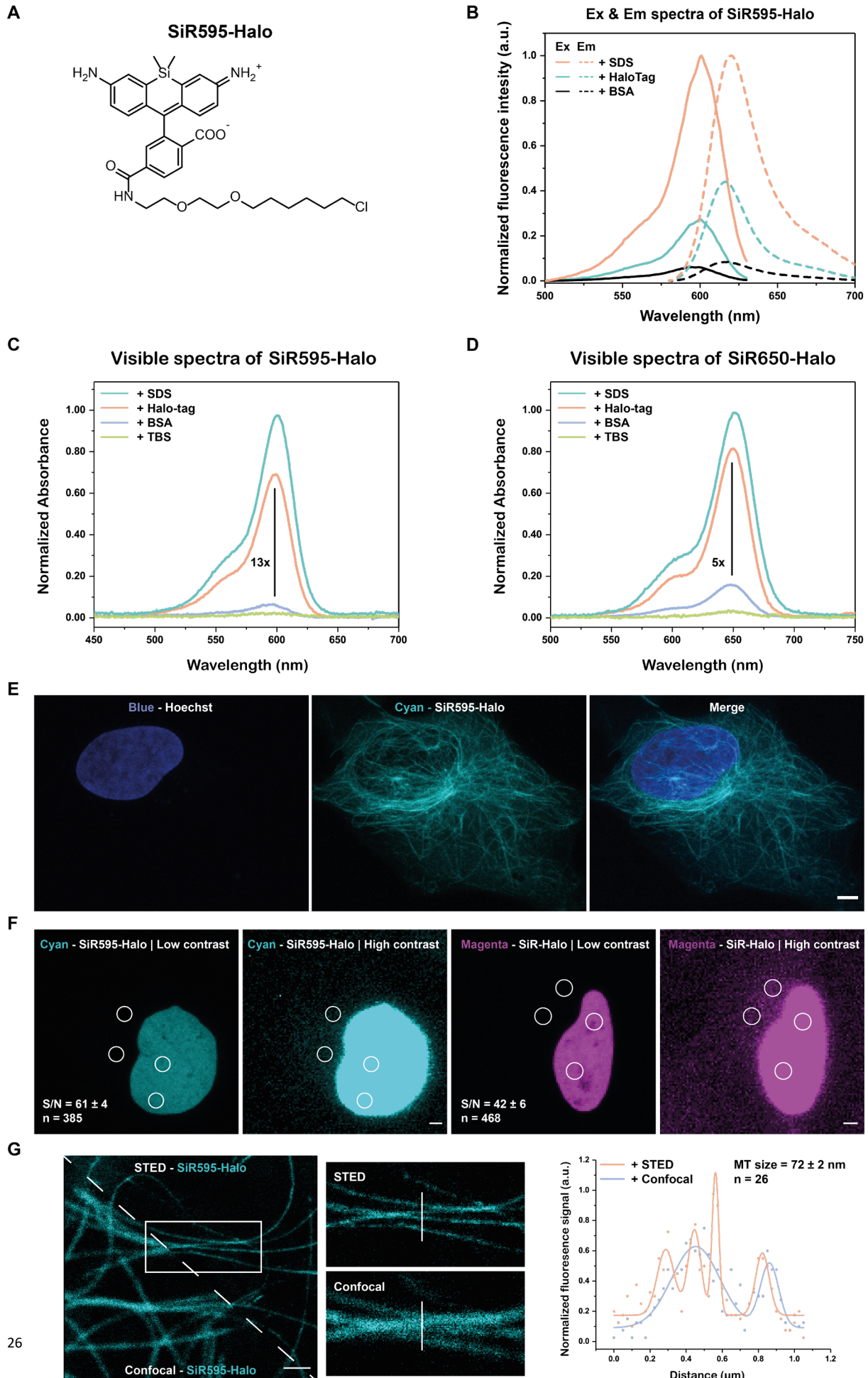
A

SiR595-Halo

B

Ex & Em spectra of SiR595-Halo

C

Visible spectra of SiR595-Halo

D

Visible spectra of SiR650-Halo

E

F

G

Figure 9. A. Structure of SiR595-Halo; **B.** Excitation and emission spectra of SiR595-Halo in different conditions; **C. & D.** Visible spectra measurements of SiR595-Halo and SiR650-Halo in presence of SDS and upon reaction with HaloTag. **E.** Live-cell confocal imaging of doxycycline induced U2OS cells to express Cep41-HaloTag and labelled with SiR595-Halo (1 μM) for 1h. Scale bar; 5 μm. **F.** Doxycycline induced U2OS cells expressing H2B-HaloTag incubated for 1h with SiR595-Halo (250 nM) or SiR650-Halo (250 nM) in presence of verapamil (10 μM). Cells were imaged without prior wash. Fluorescence signal was measured always with same size ROI, and signal from each nucleus and background from cell was measured least twice. Signal to background results are represented as mean ± s.d. **G.** STED and confocal imaging of doxycycline induced U2OS cells to express Cep41-HaloTag incubated for 1h with SiR595-Halo (1 μM). Orange rectangle represents zoomed area. Orange and blue line represent region of fluorescence signal compared in graph on the right. (right) Intensity line profile of microtubules imaged by confocal (blue) and STED(orange) microscopy. Scale bar: 1 μm.

3.3 SIR595-Actin

SiR595-Actin **19** was synthesized using an established synthetic route[36], depicted in Scheme 3. SiR595-6'-COOH **14** was activated by employing TSTU in basic conditions followed by reaction with 6-aminohexanoic acid to obtain compound **17** in 55 % yield. Upon purification compound **17** was activated with TSTU and reacted with deprotected jasplakinolide **18** to obtain SiR595-Actin **19**.
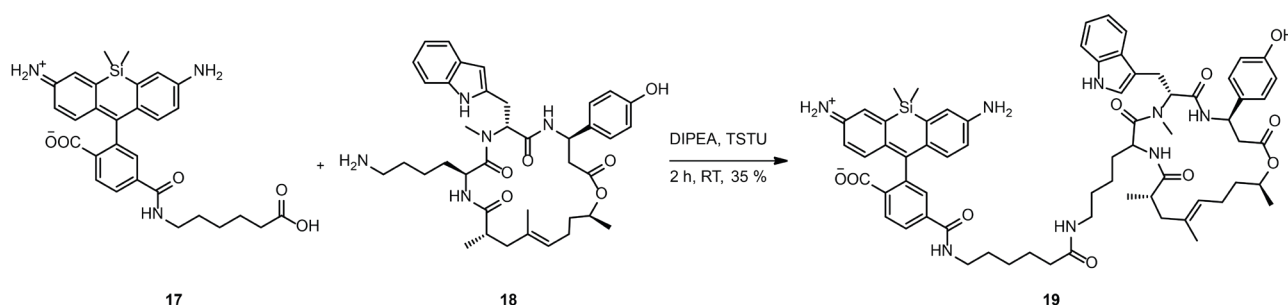
Scheme 3. Synthetic route to SiR595-Actin **19**.

To assess the fluorogenicity of SiR595-Actin (Fig 10A) we measured the absorbance and fluorescence signal increase in presence of surfactant SDS and upon interaction with the target protein, F-actin (Fig 10B, C and D). Measurements show that SiR595-Actin is indeed fluorogenic, showing moderate absorbance increase (25 ± 2 absorbance fold increase) upon interaction with F-actin, which is inferior to the absorbance increase of SiR650-Actin (54 ± 3 absorbance fold increase). At the same time, SiR595-Actin shows strong fluorescence increase (219 ± 2 fluorescence fold increase) upon biding of F-actin, which is a small improvement to measurements obtained for SiR650-Actin (171 ± 4 fluorescence fold increase) (Fig 10C and D). In the presence of SDS, both probes, SiR595-Actin (81 ± 3 absorbance fold increase) and SiR650-Actin (72 ± 2 absorbance fold increase) showed similar absorbance fold increase. Also, the fluorescence increase in the presence of SDS followed similar trends obtaining 625 ± 12 and 267 ± 18 fold of fluorescence increase for SiR595-Actin and SiR650-Actin. One should note that better signal to background ratios of SiR595-Actin probe can be attributed to very low signal in the presence of BSA. Next, we investigated the performance of SiR595-Actin in live-cell conditions. We incubated SiR595-Actin with Ref52 cells stably expressing Lifeact-GFP as reference marker. Confocal imaging showed that SiR595-Actin labels F-actin in live cells (Fig 10E). Also, SiR595-Actin shows moderate co-localization (Pearson's coefficient of 0.56) with Lifeact-GFP as an F-actin marker. Moderate Pearson's coefficient can be attribute to Lifeact's high background in cells due to its overexpression, while SiR595-Actin has very low background and the signal comes only from filamentous actin and not from unpolymerized free G-Actin. These observations also show that SiR595-Actin is cell permeable and fluorogenic; and due to its low background imaging was possible without prior washout. Furthermore, we evaluated the possibility of multicolour imaging of SiR595 and SiR650 fluorophore in combination with GFP. Simultaneous acquisitions of SiR595 and SiR650 multicolour imaging was possible with minimal crosstalk between the channels (Fig 10B and F). As an example we obtained three colour images of Ref52 cells

expressing Lifeact-GFP labelled with SiR595-Actin and SiR650-Tubulin (Fig 10F). We next assessed the utility of SiR595-Actin for STED microscopy imaging. We again used Ref52 cells expressing Lifeact-GFP labelled with SiR595-actin and SiR650-Tubulin to successfully obtain dual colour live-cell STED images using only one depletion laser (775 nm) for both fluorophores (Fig 11A). Images confirm that SiR595-Actin is compatible with STED imaging as well as live-cell dual colour STED imaging. Furthermore, to exemplify the utility of SiR595-Actin we imaged the periodical arrangement of the actin cytoskeleton in the axon and dendrites of neurons which were previously reported be ~190 nm.[36, 114] Specifically, we used hippocampal neurons isolated from rats labelled with SiR595-Actin and neurofascin as an axonal marker (Fig 11B and Appendix 7.1). As expected, STED imaging showed characteristic axonal rings separated from each other by 194 ± 9 nm (n = 13), which is in concordance with previously published work (Fig 11B and C).[36, 114]
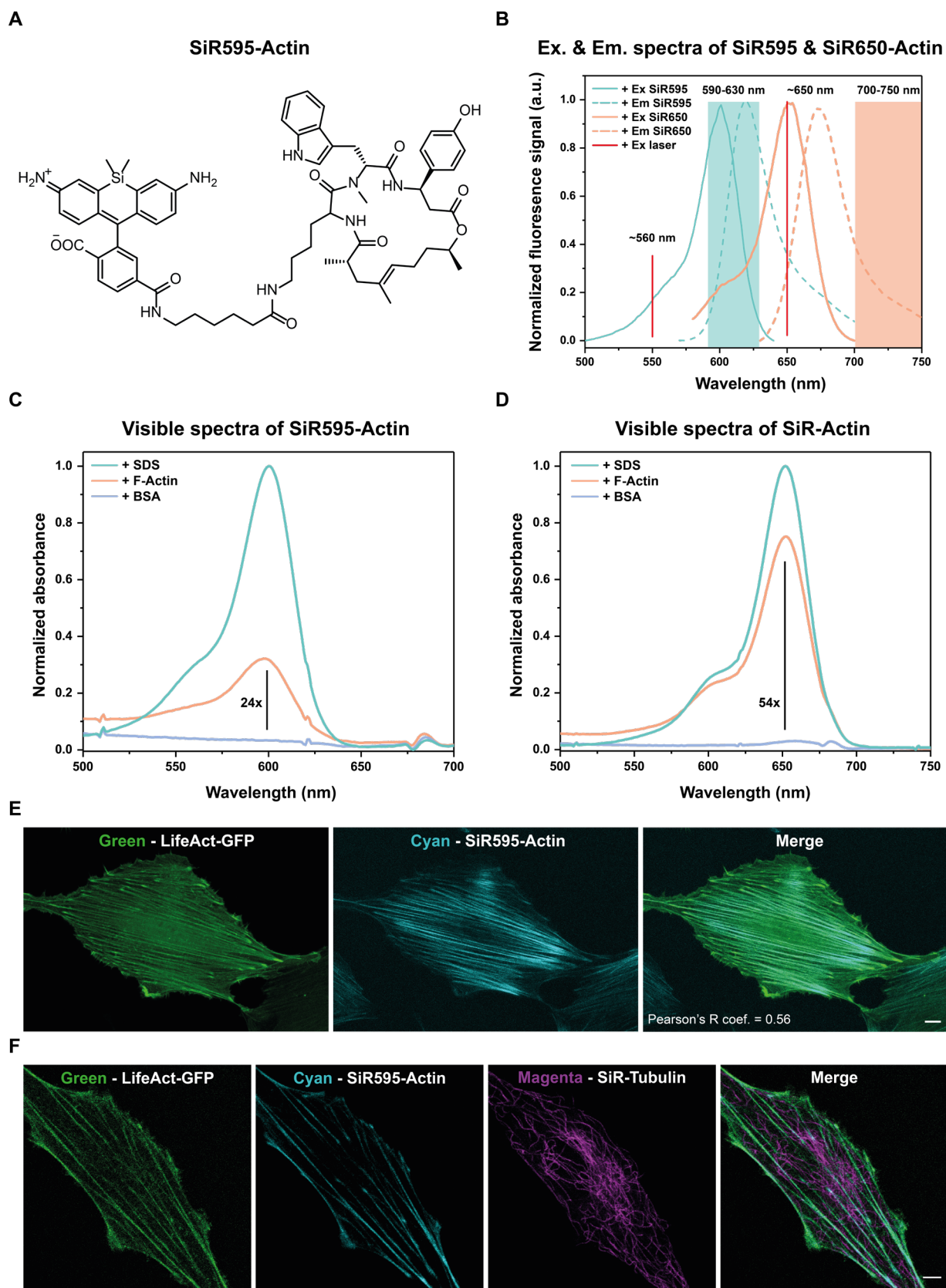
Figure 10. **A.** Structure of SiR595-Actin. **B.** Excitation and emission of SiR595-Actin and SiR650-Actin. Red lines exemplify excitation lasers used in confocal multicolour imaging; **C & D.** Visible spectra measurements of SiR595-Actin and SiR650-Actin probes in presence of SDS and upon interaction of F-Actin. **E.** Confocal imaging of Ref52 cells expressing Lifeact-GFP incubated for 1h with SiR595-Actin (500 nM). Pearson's R coefficient was calculated on maximum intensity Z- projection of two channels. Scale bar, 5 µm. **F.** Ref52 cells expressing Lifeact-GFP incubated for 1h with SiR595-Actin (500 nM) and SiR650-Tubulin (500 nM). Scale bar, 5 µm.
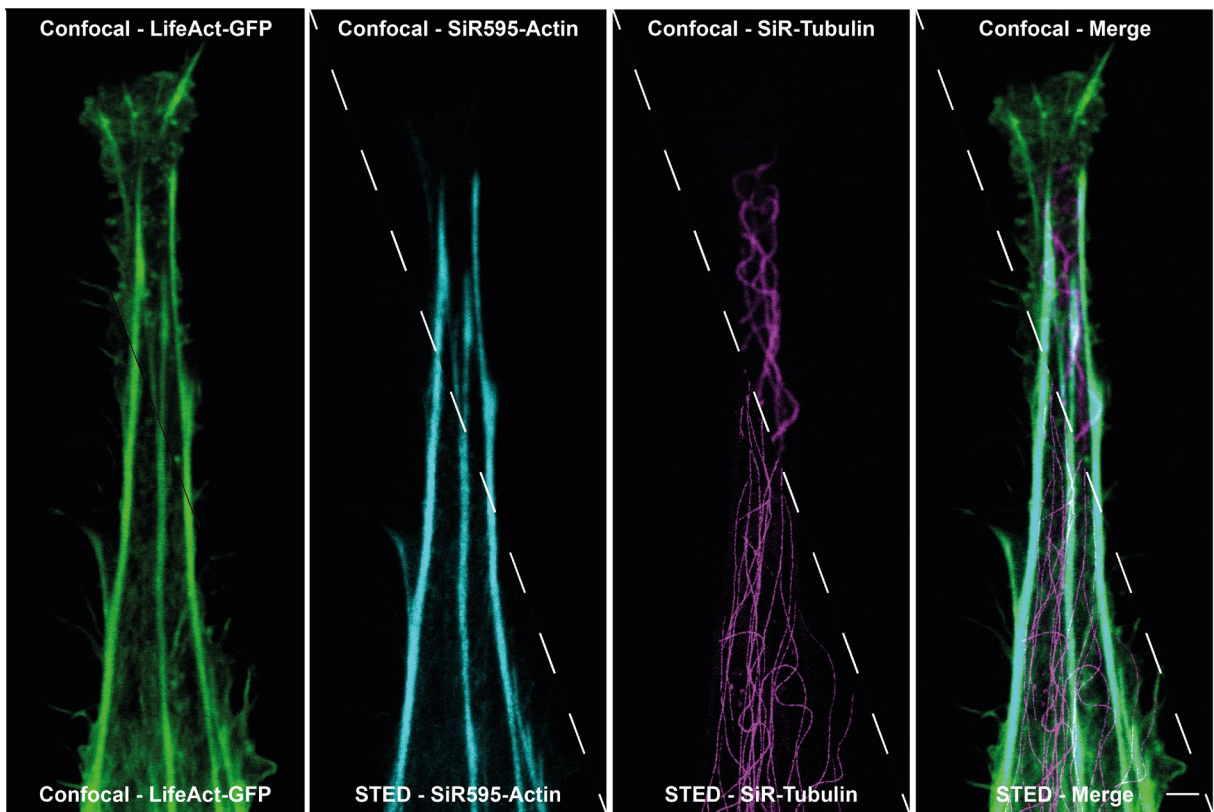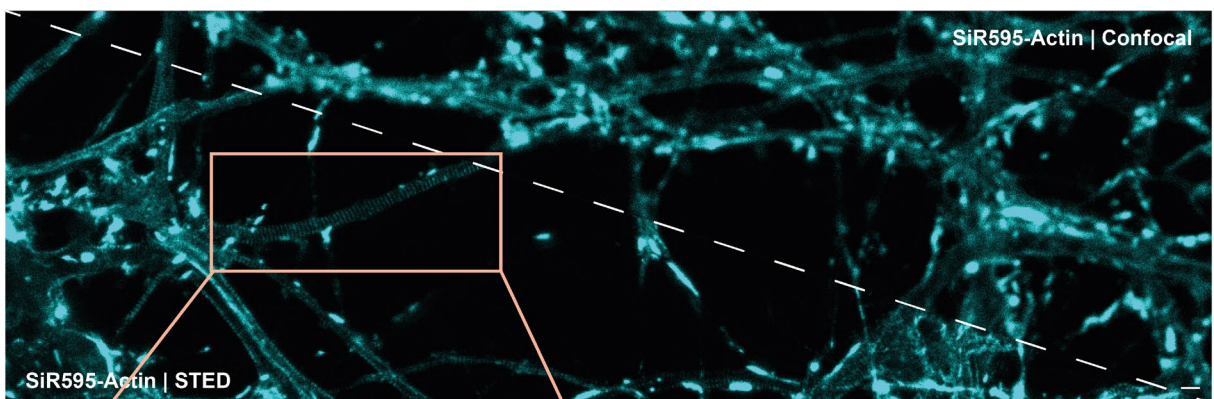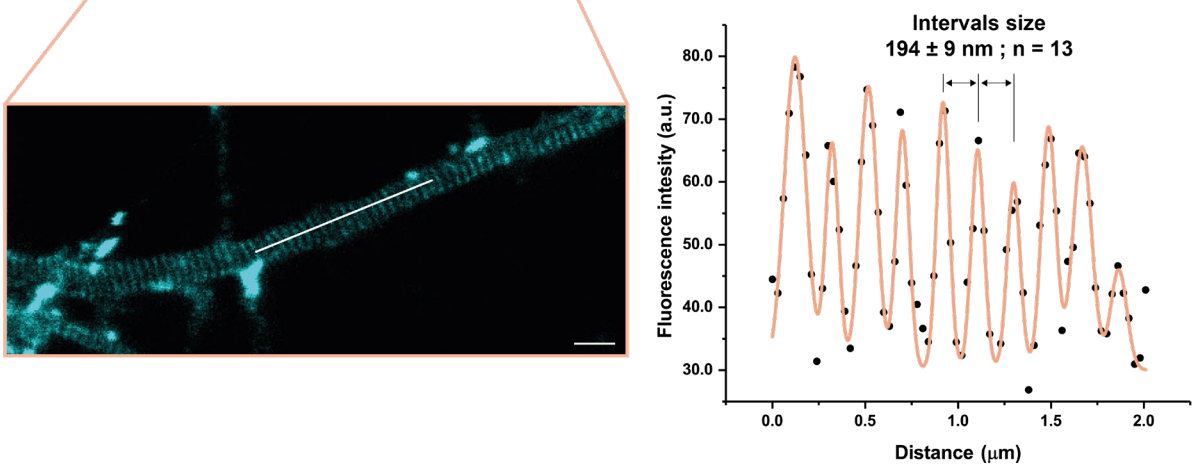
Figure 11. A. STED imaging of Ref52 cells expressing Lifeact-GFP incubated for 1h with SiR595-Actin (500 nM) and SiR-Tubulin (500 nM). Scale bar, 2 μm; **B.** Live STED imaging of Rat hippocampal neurons cultured for 22 days, and labelled with nanobody with Alexa

488 labelling neurofascin (15 min.) as axonal marker (see Appendix 7.2) and incubated with SIR595-Actin (1 μM); **C.** (left) Zoomed STED image of axon labelled with SiR595-Actin revealing the axonal rings. White line represents region of quantification in the graph on right. (right) Quantification of axonal ring distance. Distance is represented as mean ± s.d.

## 3.4 SiR595-Cabazitaxel

We set out to develop SiR595-based fluorogenic probes that label microtubules. Using previously reported strategies we used microtubule inhibitors called docetaxel, cabazitaxel and larotaxel to synthesize microtubule labelling probes (Scheme 4).[36-37] These molecules are derivatives of Taxol, a well-known cytotoxic drug that bind microtubules and stabilizes them.[62] These inhibitors bind to microtubules and prevent depolymerisation of microtubules by stabilizing the microtubule structure.[62] Using previously published routes[36-37] depicted in Scheme 4, we first synthesized compound **20**, which was then activated using TSTU in presence of base which was then independently reacted with deprotected docetaxel **11a**, cabazitaxel **11b** and larotaxel **11c** (Fig 12A).[37] Products **22a-c** were successfully obtained in ~35 % yields.
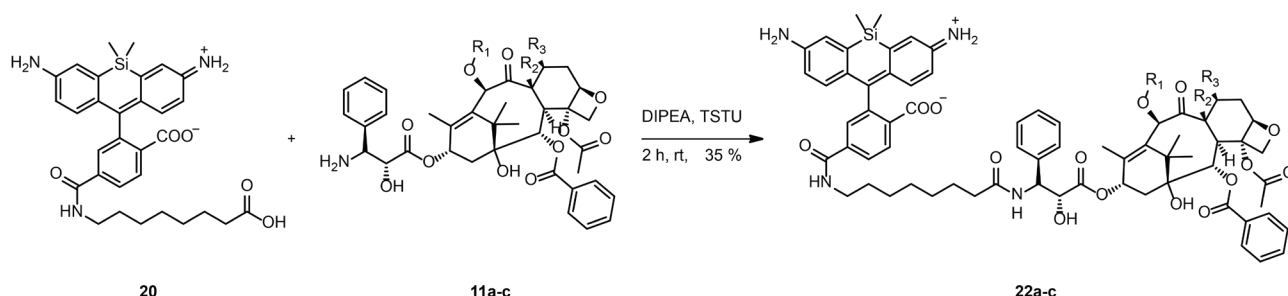
Scheme 4. Synthetic route towards SiR595-Tubulin probes **22a-c**

First, we measured the fluorescence fluorogenic response of the synthesized probes (Fig 12A) in two *in-vitro* conditions, first the fluorescence increase upon addition of SDS in TBS buffer and second upon binding of the probes to polymerized microtubules (Fig 12B, Table 3; Appendix 7.1, Fig 18). Measurements show that upon addition of SDS, the SiR595-Larotaxel (555 ± 15) has a higher fluorescence increase than SiR595-Cabazitaxel (254 ± 18), SiR595-Docetaxel (99 ± 5), and SiR650-Docetaxel (35 ± 2). When the probes bind to microtubules, SiR595-Cabazitaxel (34 ± 2) has better fluorescence fluorogenic response than SiR595-Docetaxel (13 ± 2), SiR595-larotaxel (21 ± 1) and SiR-docetaxel (15 ± 1) (Fig 12B, Table 3). We hypothesize that the lower solubility of larotaxel leads to a lower fluorogenic response of SiR595-Larotaxel upon interaction with microtubules.[37]

A   **SiR595-Tubulin probes**

	R_1	R_2	R_3
Docetaxel	-H	-OH	-CH$_3$
Cabazitaxel	-CH$_3$	-OCH$_3$	-CH$_3$
Larotaxel	-C(O)CH$_3$	-CH$_2$-	
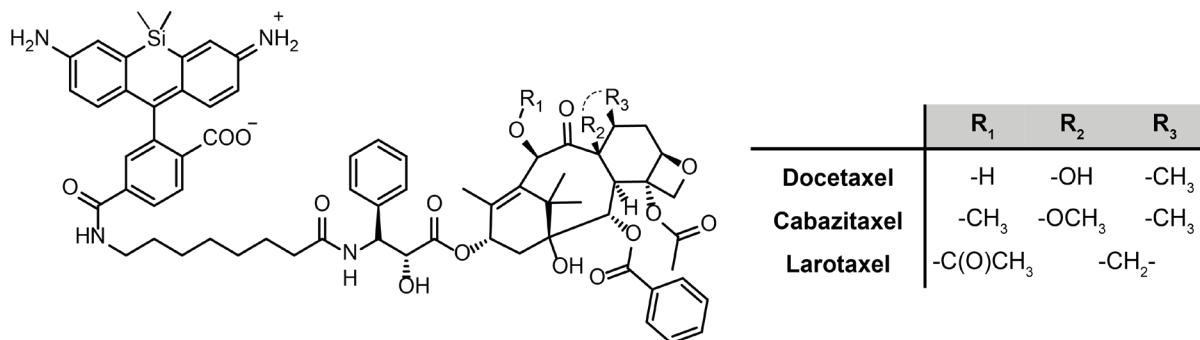
B

	SiR650-Docetaxel	SiR595-Docetaxel	SiR595-Cabazitaxel	SiR595-Larotaxel
Target / BSA	15 ± 1	13 ± 2	34 ± 2	21 ± 1
SDS / BSA	35 ± 2	99 ± 5	254 ± 18	555 ± 15

Figure 12. A. Structures of microtubule inhibitors derived SiR595 microtubule probes. **B.** Table containing fluorescence fluorogenic responses of synthesized probes in presence of SDS and upon interaction with microtubules. Results represent the ratio of $F_{(+SDS)}/F_{(+BSA)}$ or $F_{(+target)}/F_{(+BSA)}$; n=3.

Based on *in-vitro* measurements we decided to use SiR595-Cabazitaxel for *in-cellulo* labelling experiments. We tested whether SiR595-Cabazitaxel can label microtubules in live-cells. As an example, we incubated HeLa cells with SIR595-cabazitaxel and SiR650-Actin and imaged them by confocal microscopy. During confocal imaging we observed the characteristic patterns of microtubules and F-actin demonstrating the utility of SiR595-cabazitaxel (Fig 13A), as a well as compatibility of SiR595 with SiR650 for dual colour confocal imaging (Fig 12B). One should emphasize again that due to characteristically low background of the probes, both SiR595-cabazitaxel and SiR595-Actin, imaging was possible without prior washing of cells. Furthermore, we assessed the utility of SiR595-Cabazitaxel for STED microscopy. We used HeLa cells labelled with SIR595-Cabazitaxel and SiR650-Actin to demonstrate successfully live-cell dual colour STED microscopy (Fig 13C). To demonstrate the gain of resolution with STED, we measured the full width at half maximum (FWHM) of microtubule filaments. FWHM of microtubule filaments obtained by STED imaging of were determined to be 58 ± 13 nm (n = 17), which is in concordance with previously published measurements with carbopyronine-cabazitaxel (FWHM = 57± 16 nm), a dye in a similar spectral region as SiR595.[37] The size of microtubule filaments has been shown to be ~20 nm by cryo-electron microscopy.[37] The highest resolution (29 ± 11 nm) of microtubules filaments obtained by live-cell STED imaging was using SiR650-Cabazitaxel.[37] We speculate that due to the large spectral distance from the STED laser (775 nm) the dyes in this spectral region are not depleted efficiently which leads to weaker performance during imaging.

Figure 13. A. Confocal imaging of HeLa cells incubated for 1h with SiR595-Cabazitaxel (250 nM) and SiR650-Actin (500 nM). Cells were imaged in phenol free DMEM media on confocal microscope without prior wash. Scale bar, 5 μm. **B.** STED and con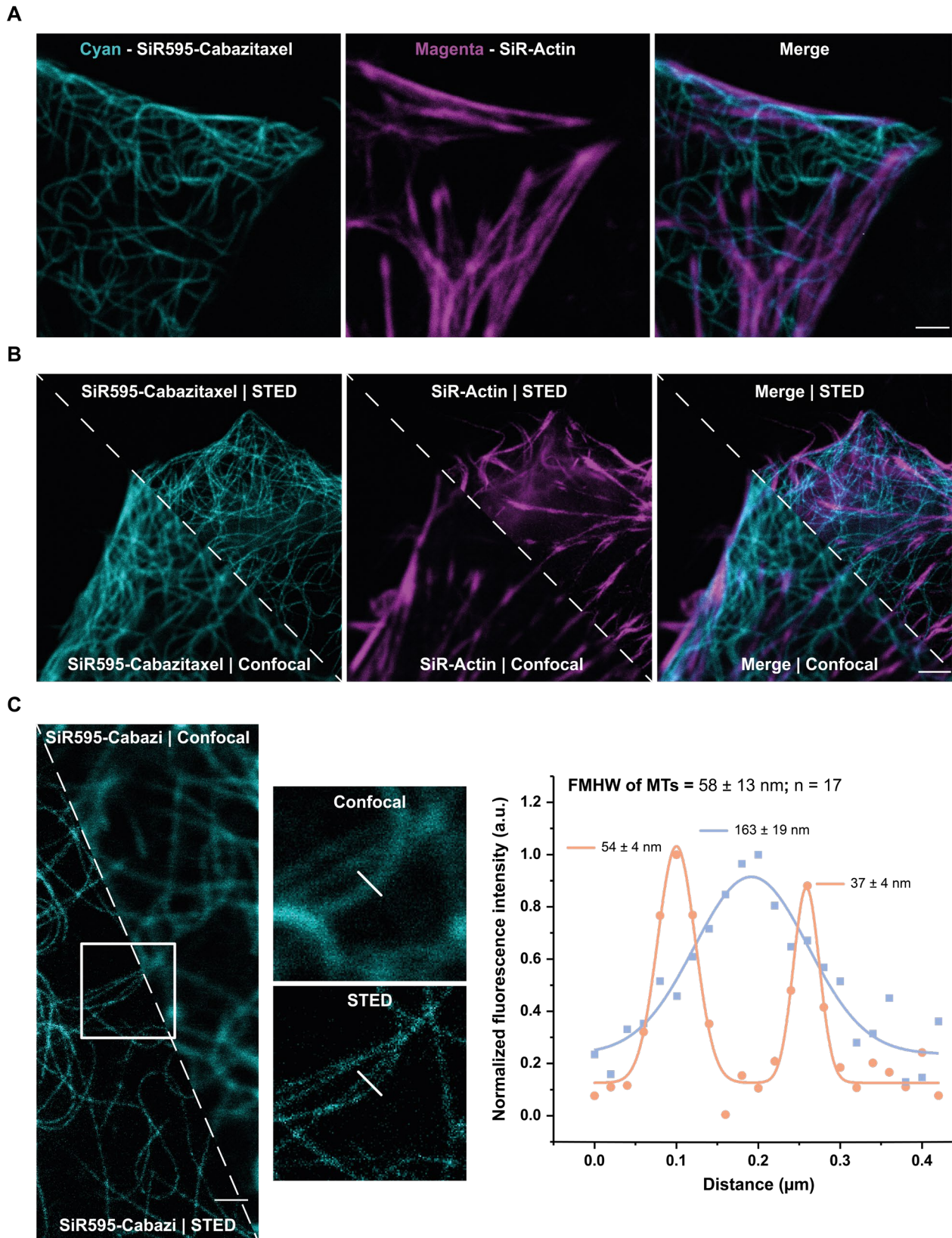focal imaging of Hela cells incubated for 1h with SiR595-Cabazitaxel (250 nM) and SiR650-Actin (500 nM). Cells were imaged in phenol free DMEM media on STED microscope without prior wash. Scale bar, 2 μm. **C.** (left) STED and confocal imaging of HeLa cells labelled with 250 nM of SiR595-Cabazitaxel for 1h imaged without prior washing. White square represents zoomed area. (right) Representative

intensity line plot of white lines depicted in zoomed areas (middle) comparing confocal (blue) and STED (orange) imaging of microtubules labelled by SiR595-Cabazitaxel FWHM is represented as mean ± s.d. Scale bar, 1 μm.

3.5 SiR595-DNA

Our lab has previously reported a far-red DNA probe based on SiR650.[38] Following our discovery of SiR650-DNA, Bucevičius *et al.* have expanded the versatility of these probes to different rhodamines-like fluorogenic dyes, as well as discovering that 5' isomers have higher brightness than 6'-isomers of the reported probes.[115] Using established methodology, we have set out to synthesize SiR595-5'/6'-DNA **24a-b** probes using Scheme 5.[38, 115]
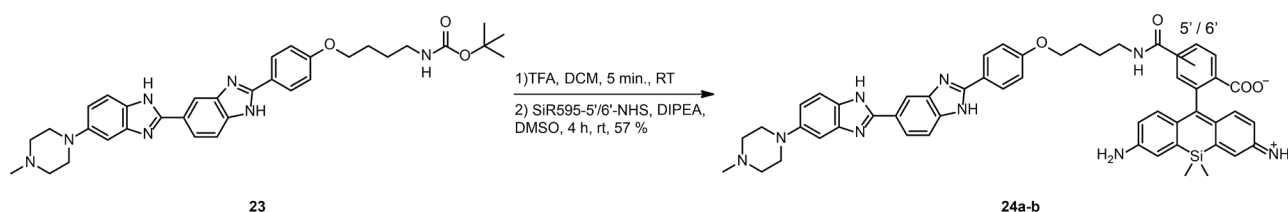
Scheme 5. Synthetic route to SiR595-5/6-DNA probe.

First, we evaluated the fluorogenicity of the synthesized probes (Fig 14A). Both probes were incubated under already established conditions. Both DNA probes, SiR595-5'-DNA and SiR595-6'-DNA, have a strong fluorescence increase in the presence of SDS, with a fluorescence increase of 388 ± 3 and 153 ± 11, respectively (Fig 13C, Table 4). To further assess the fluorogenicity of the DNA probes, we used a previously reported sequence of DNA that forms a hairpin (hpDNA) as a target for the probes. Following the same trend, both probes show good fluorescence fold-changes upon binding to the target, with increases of 26 ± 2 and 12.8 ± 0.3 (Fig 14C, Table 4). Both SiR595 probes show higher fluorogenic response than SiR650-6'-DNA (8.2 ± 0.5) (Fig 13C, Table 4) under measured conditions. We then measured the binding affinity of the synthesized DNA probes (Fig 14B and C, Table 4), obtaining K_d values of 391 ± 47 nM and 66 ± 6 nM for SiR595-5'-DNA and SiR595-6'-DNA, respectively. Based on *in-vitro* fluorogenicity measurements we decided to use SiR595-5'-DNA in further experiments. To test the utility of SiR595-5'-DNA for live-cell imaging, we incubated U2OS cells with SiR595-5'-DNA, Hoechst (33342) and SiR650-Tubulin and performed confocal microscopy. We observed co-localization of SiR595-5'-DNA with the Hoechst signal in the nucleus which confirmed the expected localization of SiR595-5'-DNA (Fig 14D). Also, we show compatibility of SiR595-5'-DNA probe with live-cell multicolour confocal imaging (Fig 14D), in combination with Hoechst and SiR650-Tubulin. Bucevičius *et al.* reports the use of rhodamine based fluorgenic probes for imaging of heterochromatine using STED microscopy. They observe heterochromatin exclusion zones (HEZs) located around nuclear pores and measure the diameter of the HEZs to be ~155 nm in living fibroblasts, HeLa and U2OS cells.[115] To assess the performance of SiR595-5'-DNA probe, we used U2OS cells that stably express Nup107-SNAP-tag as a fusion protein and incubated with SiR-BG and SiR595-5'-DNA. Nup107 is one of the structural proteins of nuclear pores located on the outer side of the nuclear membrane.[116] STED imaging revealed HEZs when labelled with SiR595-5'-DNA with SiR650 signal in the middle of the HEZs coming from labelled Nup107-SNAP by SiR650-BG. The size of HEZs was determined to be 178 ± 6 nm (n = 51) and these measurements are in concordance with previously reported data.[115]

A

SiR595-DNA probes

B

Binding curves of DNA probes

C

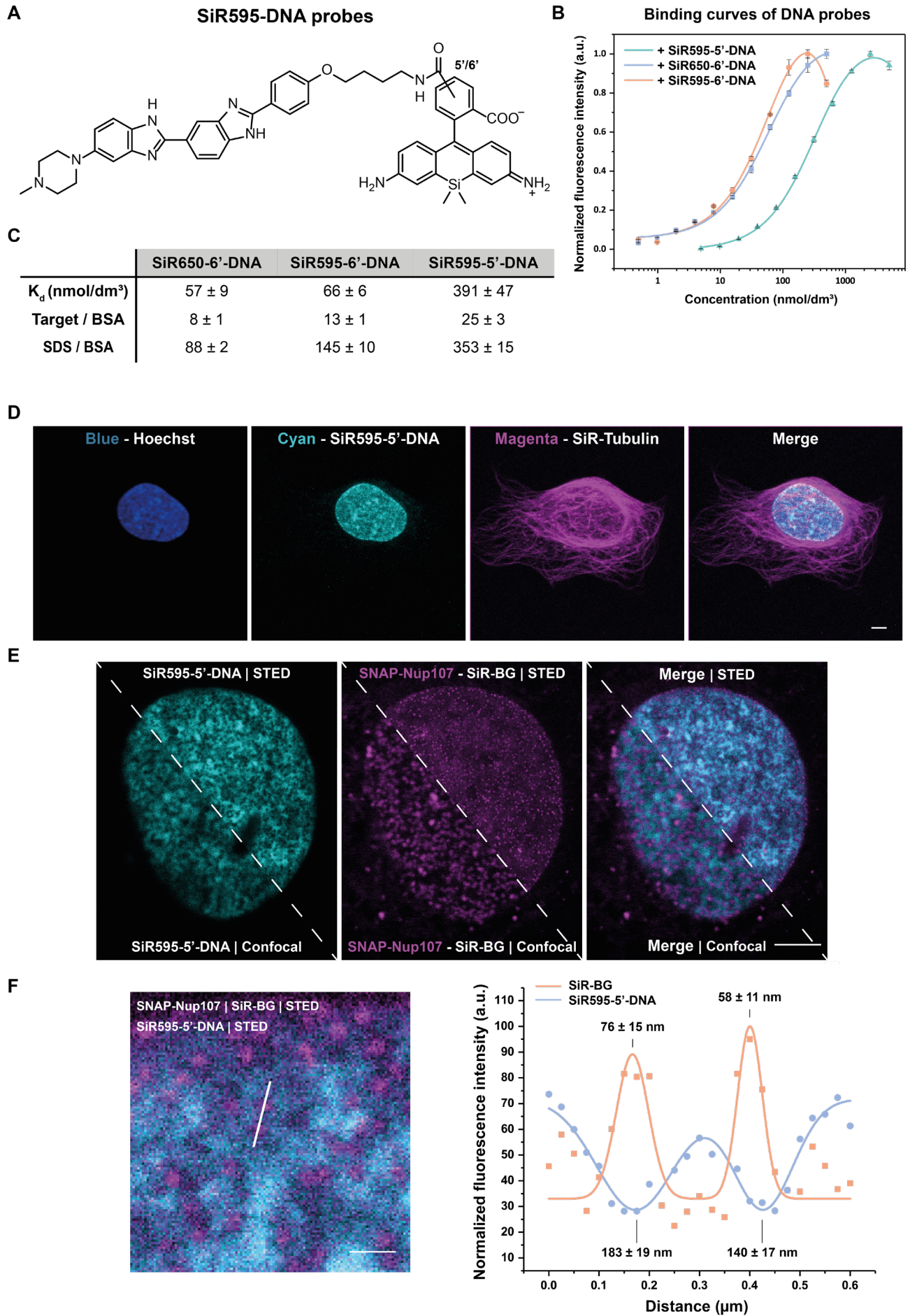|	SiR650-6'-DNA	SiR595-6'-DNA	SiR595-5'-DNA
K_d (nmol/dm³)	57 ± 9	66 ± 6	391 ± 47
Target / BSA	8 ± 1	13 ± 1	25 ± 3
SDS / BSA	88 ± 2	145 ± 10	353 ± 15

D

E

F

Figure 14. A. Structures of SiR595-5'/6'-DNA probes. **B.** Titration of 100nM of SiR595-5'/6'-DNA, and SiR650-6'-DNA probes with varying concentrations of hpDNA. Data points represent mean ± s.d. of three independent replicates. **C.** Table containing binding affinities and fluorogenicity measurements of SiR595 and SiR650-DNA probes. **D.** U2OS cells incubated in phenol-free media with 500 nM SiR650-Tubulin, 1 µM SiR595-5'-DNA and Hoechst for 1h, upon which cells were washed and imaged on confocal microscope. **E.** U2OS cells expressing Nup107-SNAP incubated in phenol-free media with SiR595-5'-DNA (1 µM) and SiR650-BG (1 µM) for 1h. Upon washing, cells were imaged on STED microscope. Scale bar: 1 µm. **F.** (left) Zoomed STED image area representing nuclear pores (Nup107-SNAP) localized in the middle of HEZs. Scale bar: 500 nm. (right) Representative intensity line plot showing sizes of two HEZs and Nup107-SNAP –tag labelled signal. Plots were fitted by Gaussian distribution. HEZs size is represented as FMHW ± s.d..

4 Centrinone based fluorogenic probes

4.1 Introduction

One of the main aims of this thesis was to develop a fluorogenic probe for live-cell labelling of centrioles. To target centrioles, we decided to use a recently identified inhibitor of Polo-like kinase 4 (Plk4), termed Centrinone (Fig 15A).[107] Plk4 is a master regulator of centriole biogenesis and during G1 phase of cell cycle, Plk4 localizes in the region around centriolar barrel termed torus. Towards the transition of G1 to S phase Plk4 forms a single focus which is believed to be a sight of procentriole formation (see Chapters 1.7-9). The inhibition of Plk4 by Centrinone prevents centriole biogenesis and ultimately leads to loss of centrioles in cell lines that lack or supress expression of p53.[107] The process is reversible and most of cells have normal centrosome numbers after 10 days of wash out. Centrinone is a very selective and potent inhibitor (K_i = 0.5 nM) of Plk4.[107] By analysing the reported crystal structure (PDB: 4YUR), we identified that the most suitable approach to attach a fluorophore to centrinone is to modify the piperidine ring of Centrinone (Fig 14B and C, arrow). The methoxy group on the pyrimidine core is essential for selectivity of Centrinone and the sulfone backbone is required for cellular activity.[107] Based on these data we envisioned several designs of probes by varying linker, handle and fluorophores to tune the hydrophobicity and distance between the Centrinone part of the probe and the fluorogenic dyes (Fig. 15D). By retrosynthetic analysis we identified two main building blocks: the Centrinone part and the fluorophore part (Fig 15E) and we set out to synthesize both of them.

A

Centrinone

B
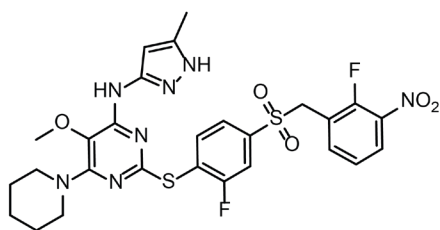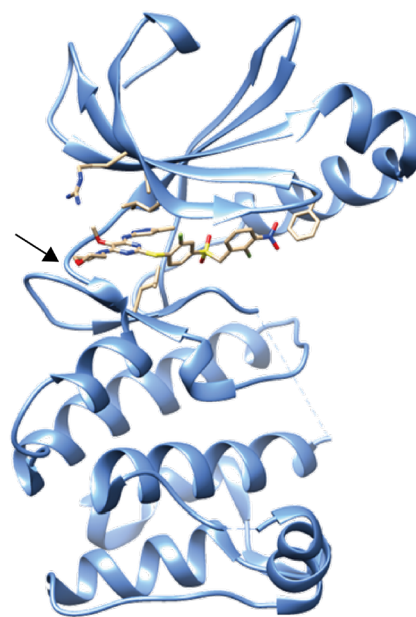
Plk4-KD

C
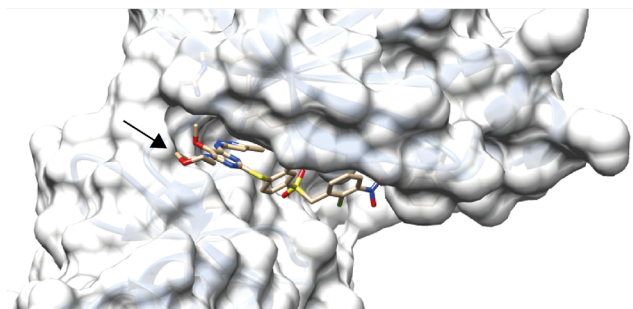
D

Fluorophore-Centrinone probe design

SiR650 or SiR595

Pyrazole

Handle

Linker

Pyrimidine

Sulfone backbone
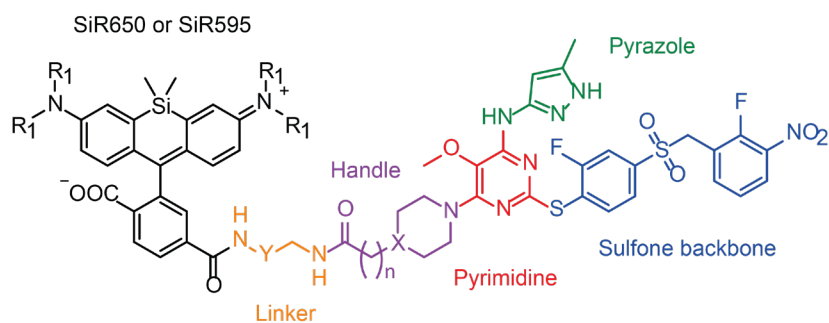
R1: Me or H
n: 1 or 2
X: N or C
Y: -(CH$_2$)$_3$- or
  -(CH$_2$)$_2$OCH$_2$-

E

Retrosynthetic analysis

Building blocks

Fluorophore part

Centrinone part

Pyrazole part

Sulfone backbone

Pyrimidine part

Handle
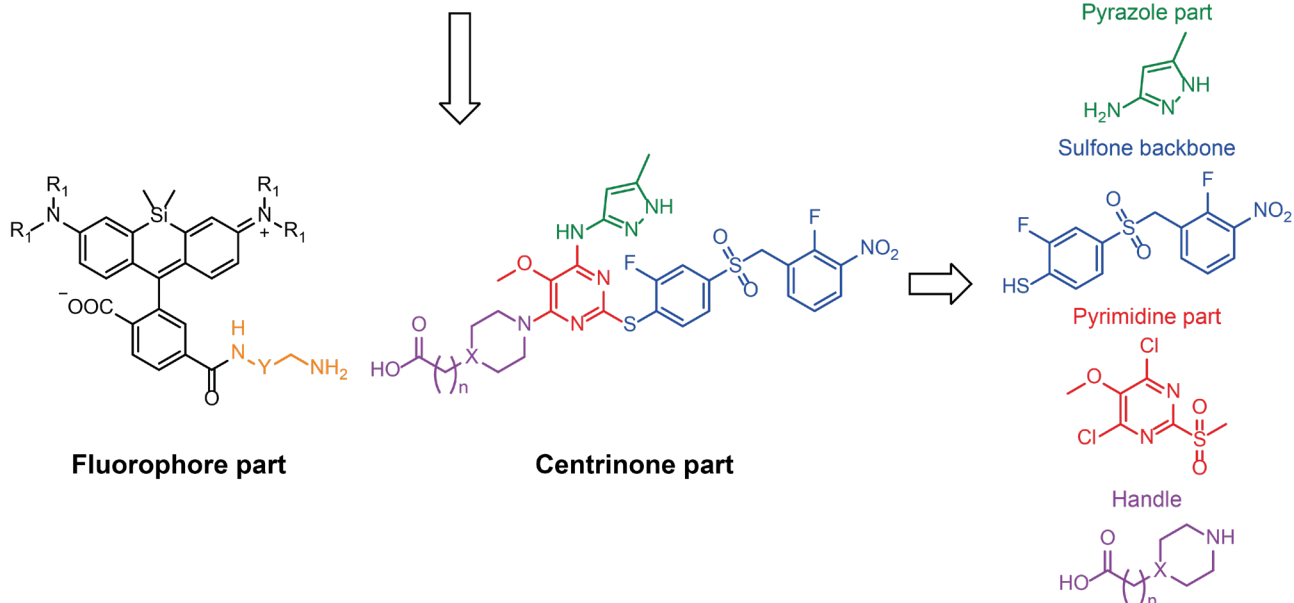
Figure 15. A. Structure of Centrinone. **B.& C.** Crystal structure with bound Centrinone (PDB: 4YUR). Arrow shows the carbon atom of the piperidine ring where we derivatized Centrinone to attach a fluorophore to it. **D**. Design of fluorophore-Centrinone probe. Black: Fluorophore part; Orange: Different linker versions; Purple: Different versions of handle; Red: Pyrimidine part; Green: Pyrazole part; Blue: Sulfone backbone. **E.** Retrosynthetic analysis depicting building blocks to approach the synthesis of different variants of the probes.

4.2   Synthesis of fluorophore-Centrinone probes

We set out to synthesize the Centrinone part of the probe by obtaining its building blocks (Fig 15E). The pyrimidine core was obtained by condensation of malonate **26** and thiourea to obtain thiomethyl barbiturate **27** in 70 % yield. Barbiturate **27** was then carefully treated with POCl₃ under microwave (MW) conditions to obtain the chlorinated pyrimidine core **28** in excellent yield. Compound **28** was then used as the main scaffold onto which the other parts of Centrinone were added. Subsequently, chloropyrimidine **28** was reacted with pyrazole **29** to obtain methyl sulphide **30,** which was further oxidized by means of mCPBA to synthesize methyl sulfone **31** in reasonable yields.
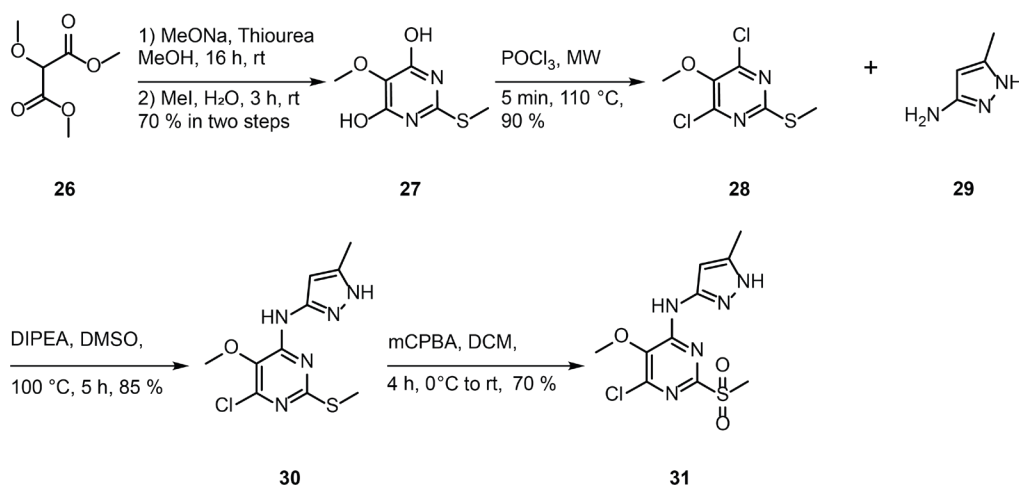
Scheme 6. Synthesis of pyrimidine core **28** and further synthesis of methyl sulfone **31**

In order to access sulfone backbone **37** we employed a Pd(II)-catalysed sulfination developed by Emmett et al. [117] Prior to this reaction we protected thiophenol **34** with a *t*-butyl protecting group. The reaction was performed in *t*-BuCl in the presence of catalytic amounts of AlCl₃ to obtain compound **35** in excellent yield. Compound **35** was then treated with Pd(II)-acetate, CataCxium A and DABSO as a source of sulphur dioxide in isopropanol in the presence of TEA. The *in-situ* generated sulfinic acid **36** was then reacted with benzyl bromide **33** to obtain compound **37** in 49 % yield. Installing the *t*-butyl protecting group on the thiophenol **34** was essential due to its tolerance to the acidic environment created by the release of sulphur dioxide during the Pd-catalyzed sulfination.
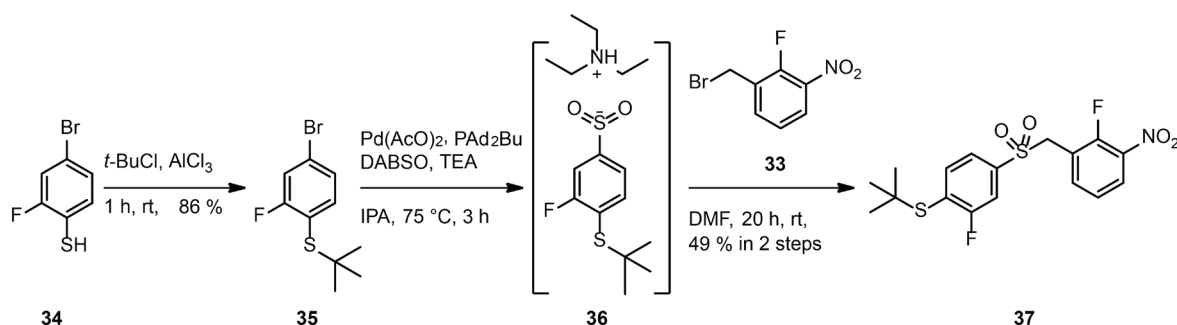
Scheme 7. Synthesis of sulfone backbone **37**

The formation of compound **38** was achieved upon deprotection of sulfone **37** under harsh acidic conditions to produce **36**. Without further purification compound **36** was directly reacted with methyl sulfone **31** to obtain the desired compound **38** via S$_N$Ar in moderate yield. Compound **38** was the main precursor which we structurally diversified to form different Centrinone based probes.
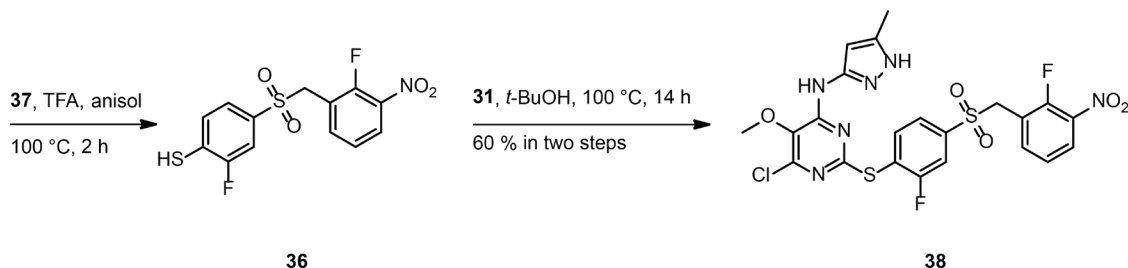
Scheme 8. Assembly of compound **38**

We then reacted compound **38** with three different piperidine or piperazine derivatives **29a**, **29b** and **29c** to obtain various Centrinone parts **40a**, **40b, 40c** and **40d** in 42 % - 56 % yields. These compounds have different handles, which were used to attach different fluorophore parts. The rationale behind these structural changes will be discussed below.
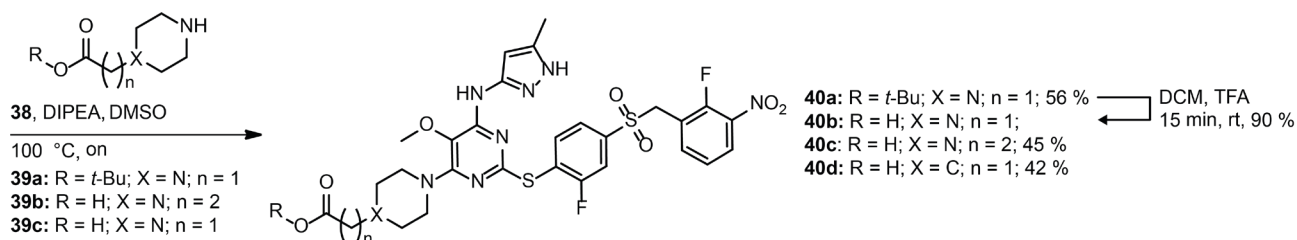
Scheme 9. Synthesis of various Centrinone parts **30a-d**.

Finally, SiR595 (**14**) and SiR650 (**41**) were conjugated to different linkers **42a and 42b** using identical conditions to obtain compounds **43a**, **43b**, **43c**, **43d**, **43e**, **43f** which we used to synthesize different fluorophore-Centrinone probes.
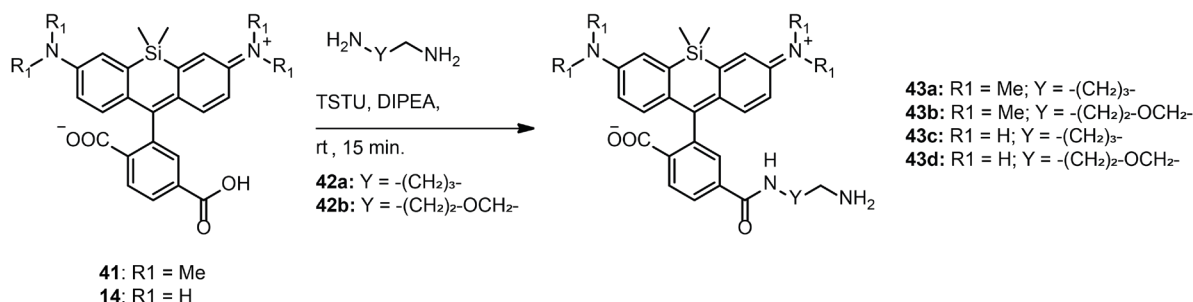
Scheme 10. Conjugation of fluorophores with different linkers for attachment to Centrinone

To finally obtain the Centrinone based probes we conjugated different Centrinone parts **40b-c** to different fluorophore parts **43a-f** to form different fluorophore-Centrinone probes **44a-f**.

40b-c, EDC/HOBt or HATU, DIPEA, rt

43a: R1 = Me; Y = -(CH$_2$)$_3$-
43b: R1 = Me; Y = -(CH$_2$)$_2$-OCH$_2$-
43c: R1 = H; Y = -(CH$_2$)$_3$-
43d: R1 = H; Y = -(CH$_2$)$_2$-OCH$_2$-

44a: R1 = Me; Y = -(CH$_2$)$_2$-OCH$_2$-; X = N; n = 1; 23 %
44b: R1 = Me; Y = -(CH$_2$)$_2$-OCH$_2$-; X = N; n = 2; 24 %
44c: R1 = H; Y = -(CH$_2$)$_2$-OCH$_2$-; X = N; n = 1; 29 %
44d: R1 = H; Y = -(CH$_2$)$_2$-OCH$_2$-; X = N; n = 2; 35 %
44e: R1 = H; Y = -(CH$_2$)$_2$-OCH$_2$-; X = C; n = 1; 40 %
44f: R1 = H; Y = -(CH$_2$)$_3$-; X = C; n = 1; 44%
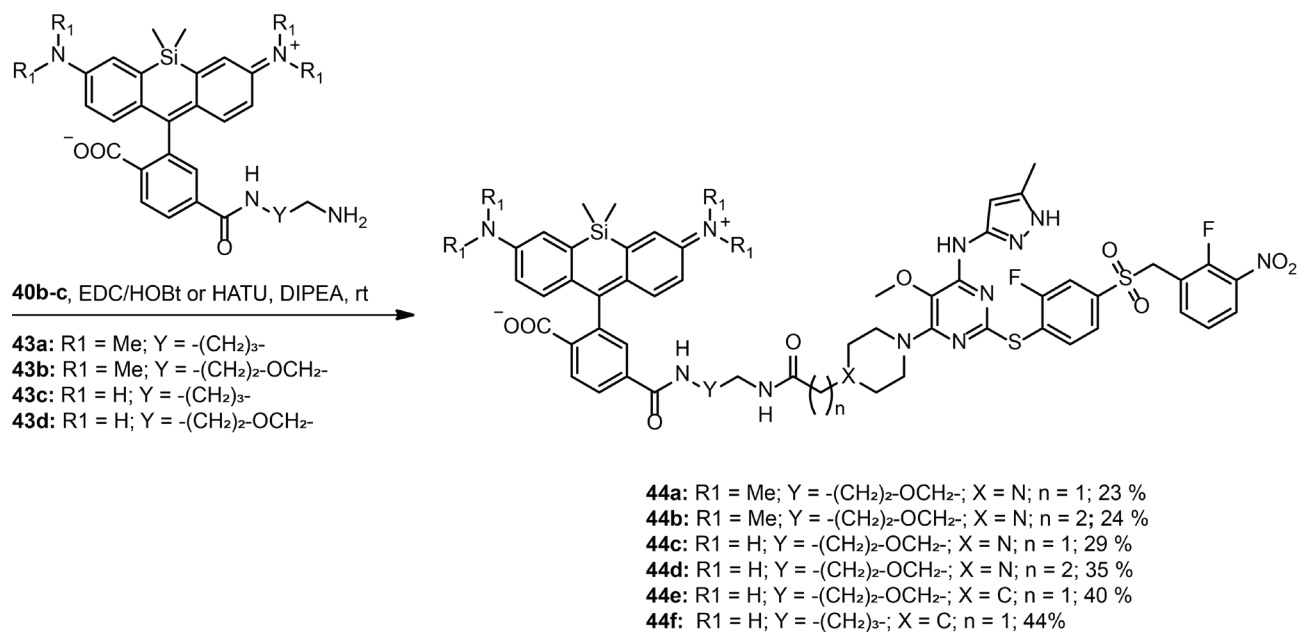
Scheme 11. Synthesis of different of Centrinone base probes **44a-f**

4.3   Silicon-Rhodamine650-Centrinone probes

Using the strategy described in the Chapter 4.2. we synthesized different SiR650-Centrinone probes (Fig 15A). First we evaluated the fluorogenicity of these probes in the presence of SDS and Plk4. For this purpose, we expressed and purified the Plk4 (2-275) kinase domain(KD) with His-tag (Appendix 7.4, Fig 21). The synthesized probes **44a** and **44b** indeed showed fluorogenic response in the presence of SDS in Tris buffer, with fluorescence intensity fold changes of 16 ± 3 and 28 ± 3, respectively. The probes also showed fluorogenic response upon interaction with Plk4-KD with fold changes up to 3.7 ± 0.3 and 4.9 ± 0.4, respectively. Probe **44b** showed higher fluorogenic response than **44a**. Next, we measured binding affinities of the probes by fluorescence polarization (FP).[118-119] As a tracer probe for our FP measurements we synthesized Alexa488-Centrinone. Alexa488-Centrinone was then titrated by Plk4-KD to obtain a binding affinity of 5.9 ± 0.8 nM (Fig 16B). Next we established a competition binding assay to measure binding affinities of the synthesized probes. The reported K_i value of Centrinone is 0.6 nM while in our measurements Centrinone shows a binding affinity that is below 1 nM (Fig 16C). Due to limitations of the FP binding assay we could not reliably measure binding affinities lower than 1 nM, and low affinity binding of Centrinone is in accordance with the reported data.[120] We then measured binding affinities of compounds **44a** and **44b** to be 45 ± 6 nM and 13 ± 3 nM, respectively. These measurements indicate that the binding of the synthesized probes is specific to the reported Centrinone binding site. We next evaluated whether the probes label centrosomes in live cells. Hela cells stably expressing Centrin1-GFP were used to mark centrioles and incubated with the SiR-Centrinone probes. We observed that SiR-Centrinone probes accumulate into a dot like structures in live-cell, hence we speculated that the probes are trapped in lysosomes. To confirm this hypothesis, the cells were incubated with **44a** together with Lysotracker and Hoechst 33342 (Fig 16D). Confocal imaging showed that **44a** co-localized with Lysotracker with Pearsons's correlation coefficient 0.85, confirming our hypothesis that the probes are trapped in lysosomes (Fig 16D). We speculated that due to the basicity of the amine in the piperazine ring, the probes were protonated during endocytosis, and were trapped in lysosomes/endosomes leading to an opening of the SiR650 spirolactone. To address these issues we envisioned using a handle that does not contain the amine in the structure (e.g. piperidine derivative). Also, we speculated that fluorogenic fluorophores with a spirolactone equilibrium shifted to more closed forms, such as SiR595, would allow greater permeability of the probes.
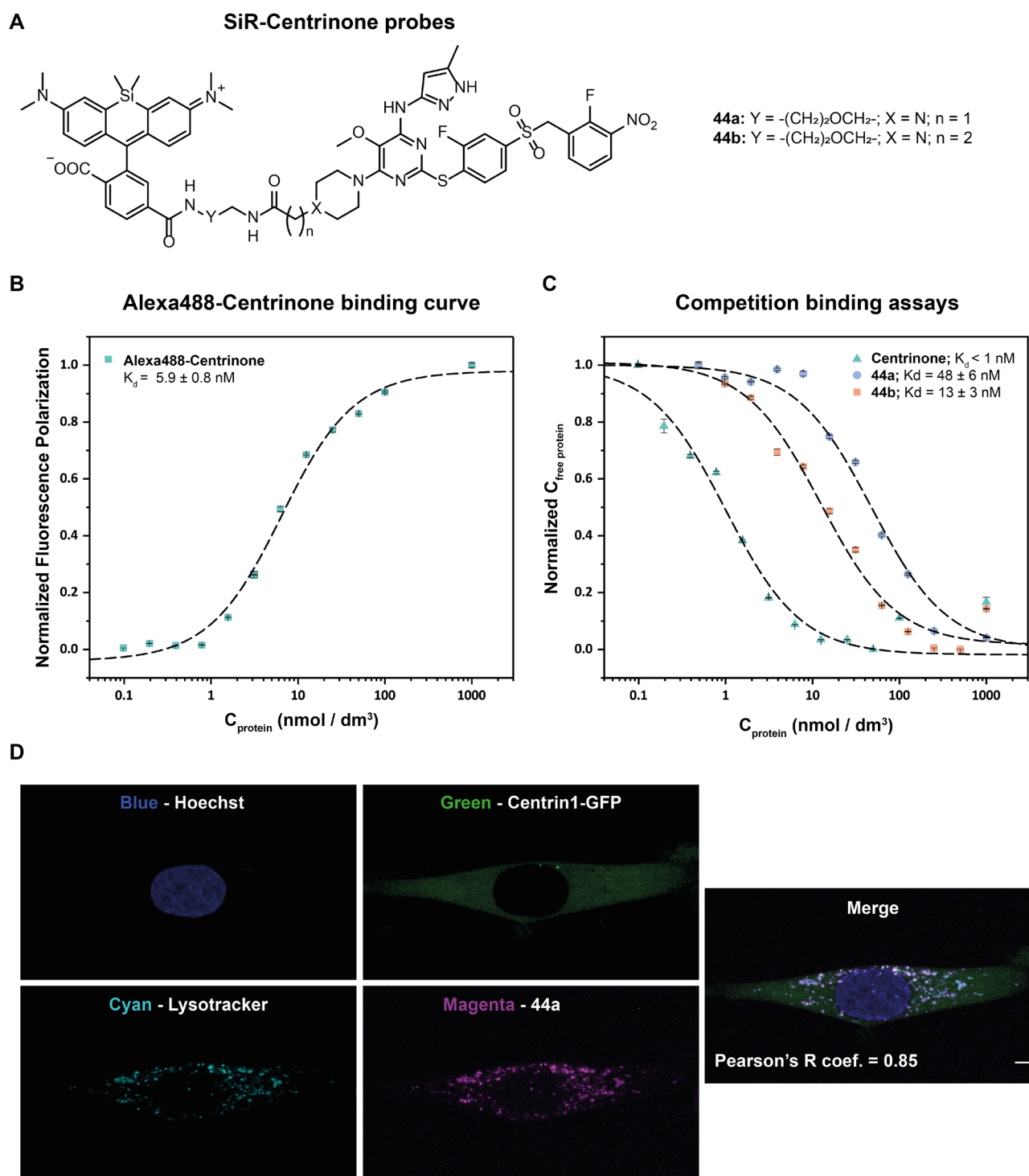
Figure 16. A. Structure of synthesized probes. **B.** Fluorogenicity of SiR-Centrinone probes. **C.** Fluorescence polarization binding curve of Alexa488-Centrinone (1 nM) titrated with different concentrations Plk4-KD. **D.** Competitions binding assays of Alexa488-Centrinone (1 nM) and Plk4-KD (10nM) titrated with different concentrations of Centrinone and SiR-Centrinone probes. **E.** Confocal imaging of Hela cells expressing Centrin1-GFP incubated for 1 h with **44a** (1 μM), 30 min with Lysotracker (50 nM) and 10 min with Hoechst 33342.

4.4 Silicon-Rhodamine595-Centrinone probes

To address the problems of unspecific staining as well as of permeability with SiR-Centrinone probes, we synthesized different SiR595-Centrinone probes (Fig. 17A, **44c-f**). As discussed previously, the SiR595 spirolactone equilibrium is shifted to mostly the closed form in aqueous solutions, and we hypothesized that this property will increase permeability of the probes through the cell membrane. Also, instead of using piperazine derivatives as a handle for conjugation, we tested piperidine derivatives to conjugate the fluorophore part to the Centrinone part. We first obtained probes **44c** and **44d** and assessed the fluorogenicity of these probes, and indeed the synthesized probes were fluorogenic in the presence of SDS (Fig 17B), with values of 101 ± 22 and 262 ± 5 fold change in fluorescent intensity, respectively. The probes also show fluorogenic response upon interaction with Plk4-KD, with values of 9.6 ± 0.5 and 14 ± 1, respectively (Fig. 16B). Both probes show significant improvements in fluorogenicity in comparison to SiR-Centrinone probes. Next we measured binding affinities of **44c** and **44d** (Fig 17C) using the established competition binding assay and obtained values of 27 ± 5 nM and 21 ± 3 nM, respectively. These measurements indicate that the synthesized probes bound to the same binding pocket as Centrinone. These modifications lead to a ~50x loss of affinity in comparison to Centrinone.

Subsequently, we assessed whether **44c** and **44d** label centrioles in live cells. Hela cells stably expressing Centrin1-GFP were incubated with **44c** and **44d** and imaged by confocal microscopy. It was observed that the **44c** probe showed similar fluorescent pattern as observed with the **44a** probe, corroborating the hypothesis that due to the amine in the piperazine ring, the probe gets trapped in lysosomes and/or endosomes (Fig. 15D). Also, we observed that the **44d** probe showed lower unspecific labelling than **44c.** Next, we tested whether the **44d** probe labels overexpressed Plk4 in live cells. It is known that the copy number of the Plk4 protein is very low and the levels of Plk4 are tightly regulated in human cells (see Chapter 1.9).[121] To circumvent the problem with low amounts of Plk4 during the optimization of the probe we used Hela cells and transfected them with GFP-Plk4 with a kinase dead domain (K41M). as overexpression of Plk4 with an active kinase domain leads to amplification of centrioles in cells.[122] Upon transfection, cells were incubated with **44d** and imaged by confocal microscope. Under these conditions co-localization of SiR595 signal with GFP-Plk4(K41M) signal was observed (Fig 17D). Also, minor unspecific labelling was observed that we speculated resulted from the probe trapped in lysosomes and/or endosomes. Next, we tested whether we can use **44d** to image overexpressed GFP-Plk4 with STED microscopy. We used the same labelling conditions as described before and observed weak circular signal corresponding to SiR595 signal, which colocalized with the GFP-Plk4(K41M) signal (Appendix 7.5, Fig 22A). The cells were then fixed, labelled with anti-GFP nanobody. and imaged by STED microscopy. The images confirmed that the observed SiR595 signal colocalizes with anti-GFP nanobody as well as with GFP-Plk4(K41M), indicating that the signal of **44d** comes from labelling of overexpressed GFP-Plk4(K41M) (Appendix 7.5, Fig 22B). The observed signal is weak, presumably due to low fluorogenicity and/or incomplete opening of probes **44c** and **44d** upon binding of GFP-Plk4(K41M). To improve the fluorogenic response we synthesized two other variants **44e** and **44f.** These probes have as handle a piperidine derivative **39c** which does not have nitrogen in the heterocycle which we suspected to cause entrapment of probes in lysosomes/endosomes. Also, probe **44f** have a shorter linker than **44e** (Fig 17A). The fluorogenicity of the probes was measured in the presence of SDS with values of 248 ± 16 and 918 ± 31 fold change in fluorescent intensity, respectively. The observed fluorogenicity upon interaction with Plk4-KD was measured to be 10.2 ± 0.4 and 17 ± 2 fold change in fluorescence intensity, respectively (Fig 17C). Thus, the probe **44e** showed similar fluorogenic response as **44d.** The **44f** probe showed mild improvement in fluorogenicity upon interaction with Plk4-KD relative to **44d** and **44e** (Fig 17C), while upon addition of SDS the probe showed a much stronger fluorogenic response improvement in comparison to other probes. Next we used overexpressed GFP-Plk4(K41M) conditions to evaluate the labelling of centrioles in cells by these probes. We incubated cells with **44e** and **44f** and imaged them live by STED microscopy. We observed that both probes show better labelling and stronger SiR595 signal than **44d**.

The **44f** probe showed the best performance and we could successfully observe centrioles with a 9-fold symmetry of the fluorescence signal resulting from overexpressed GFP-Plk4(K41M) protein (Fig 17E). The diameter of the circular signal was measured to be 362 ± 21 nm (n= 8 of centrioles in 7 different cells). We speculated that GFP-Plk4(K41M) localizes to the outer part of the torus of the centriole. The torus was reported to encompasses the region of 210-450 nm in diameter, depending on the conditions of labeling.[74, 123-124] For example, recent work on purified centrioles isolated from KE37 cells reported that the main torus components, Cep152/Cep63/Cep57 have diameter of ~270, ~290 and ~210 nm, respectively; and these measurements were acquired by 3D-SMLM.[70] Work on fixed HeLa cells reported the dimeter of Cep152 to be ~435 nm measured by 3D-SIM. The reported diameters for Plk4 also vary from ~270 nm to ~600 nm depending on the reports.[59, 74] The Plk4 diameter in fixed Hela cells is reported to be ~450 nm prior to Cep152 recruitment and ~590 nm upon Cep152 recruitment.[74] These measurements were acquired on antibody stained fixed U2OS cells which were imaged by 3D-SIM microscopy.[74] Labelling of overexpressed Plk4-SNAP in fixed U2OS cells showed diameter of ~ 270 nm which was determined by STED imaging.[59] The differences in reported data may come due to differences in cell lines, as well as due to purification of centrioles in comparison to fixed cells. Also, one should note that the overexpression of GFP-Plk4 (K41M) may lead to a miss localization of the protein. Hence, the reasons of the localization of labelled GFP-Plk4 (K41M) is not fully understood and further investigation is required. Also, these probes did not succeed in reliably labelling Plk4 at endogenous levels (data not shown). The expression levels of Plk4 are reported to be very low throughout cell cycle with a protein amount peaking during early G1 phase when Plk4 forms a ring around mother centriole prior to the Plk4-STIL module formation.[121, 125-126] To assess what would be detectable amounts of Plk4 one could measure the concentration differences between Plk4 levels at different cell cycle stages in comparison to the amounts of overexpressed GFP-Plk4 (K41M). Such experiments were performed, albeit the imaging parameters we used during acquisition of images were not optimized and obtained data was not reliable. Furthermore, development and optimization of fluorogenic probes with improved fluorogenicity may allow detection of low Plk4 amounts.
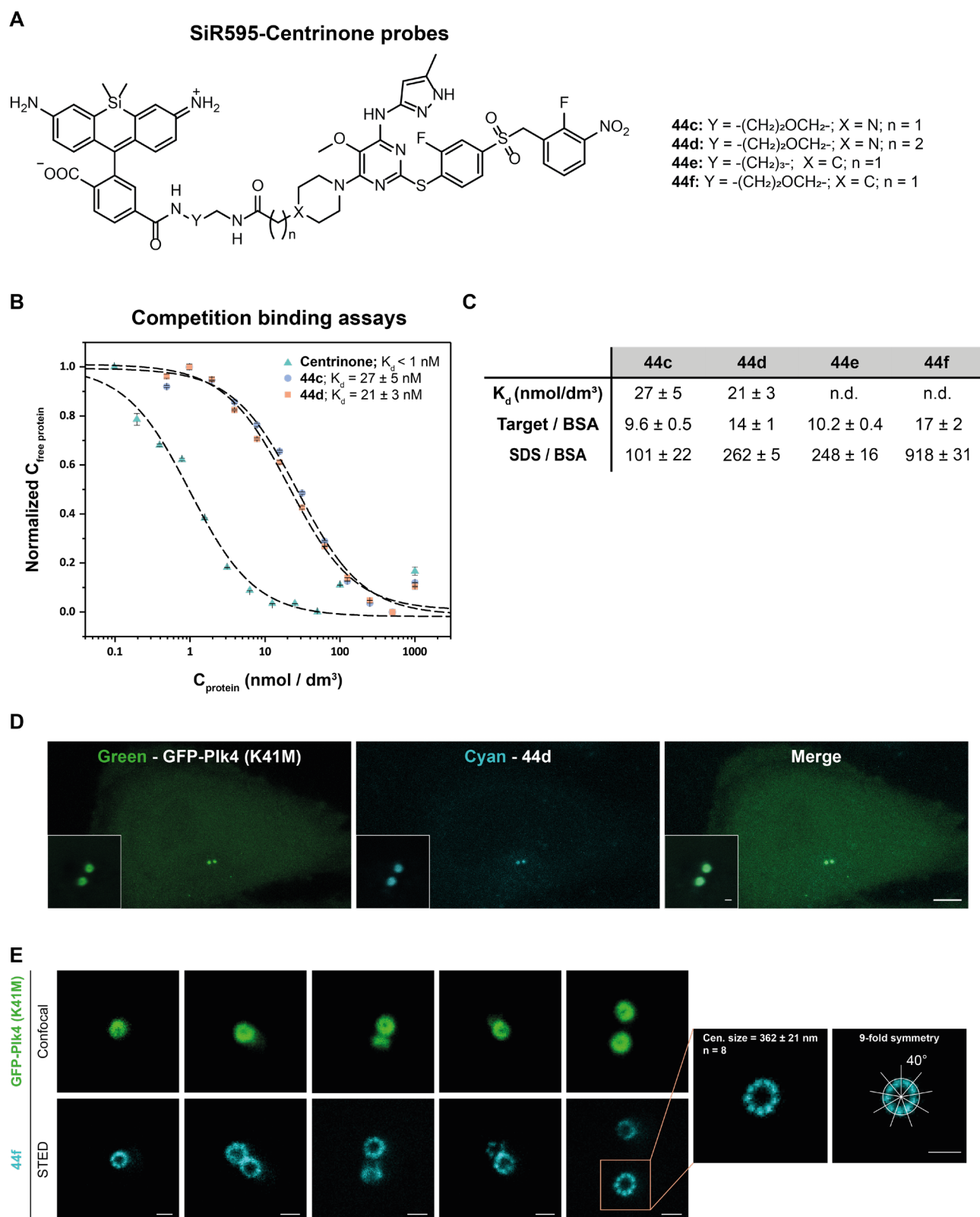
A

SiR595-Centrinone probes

44c: Y = -(CH$_2$)$_2$OCH$_2$-; X = N; n = 1
44d: Y = -(CH$_2$)$_2$OCH$_2$-; X = N; n = 2
44e: Y = -(CH$_2$)$_3$-; X = C; n =1
44f: Y = -(CH$_2$)$_2$OCH$_2$-; X = C; n = 1

B

Competition binding assays

▲ Centrinone; K$_d$ < 1 nM
● **44c**; K$_d$ = 27 ± 5 nM
■ **44d**; K$_d$ = 21 ± 3 nM

C

	44c	44d	44e	44f
K$_d$ (nmol/dm³)	27 ± 5	21 ± 3	n.d.	n.d.
Target / BSA	9.6 ± 0.5	14 ± 1	10.2 ± 0.4	17 ± 2
SDS / BSA	101 ± 22	262 ± 5	248 ± 16	918 ± 31

D

Green - GFP-Plk4 (K41M) | **Cyan** - 44d | **Merge**

E

GFP-Plk4 (K41M) — Confocal
44f — STED
Cen. size = 362 ± 21 nm
n = 8
9-fold symmetry
40°

Figure 17. A. Structures of synthesized SiR595-Centrinone probes. **B.** Competition binding assays of centrinone and SiR595-Centirnone probes. Data points represent a mean of three independent measurements and K$_d$ are represented as value ± s.d. **C.** Table of measured binding affinities and fluorogenicity of synthesized probes in different conditions. Fluorogenicity results represent the ratio of F$_{(+SDS)}$/F$_{(+BSA)}$ or F$_{(+target)}$/F$_{(+BSA)}$. Values are represented as mean ± s.d. of three independent measurements. **D.** Confocal imaging of Hela cells transfected for 4h with GFP-Plk4 (K41M), followed by overnight washing in DMEM media. The following day cells were

incubated with 500 nM of **44f** probe followed by imaging on a confocal microscope. Scale bar: 5 µM and 500 nm. **E**. Live-cell confocal and STED images of centrioles obtained by imaging unsynchronized Hela cells overexpressing GFP-PLK4 (K41M) labelled for 1h by **44f** (500nM) (see Appendix 7.6, Fig 22. for complete set of data). STED imaging was performed subsequently to Confocal imaging which may lead to position difference of centrioles in-between two modes of imaging. Centriole size is represented as mean ± s.d (n = 8 of centriole in 7 different cells). Scale bar: 500 nm.

5 Discussion and Conclusion

5.1 Achieved results

Herein we report a novel fluorogenic molecule, silicon rhodamine595 (SiR595), that absorbs in the spectral region of 600 nm with good extinction coefficient and quantum yield (ε = 75000 M^{-1} cm^{-3}, Φ = 0.5). SiR595 exists in a similar spirolactone equilibrium as SiR650, but the equilibrium is significantly shifted towards the closed, non-fluorescent form. This allowed development of probes with greater permeability and lower background fluorescence, enabling imaging without removal of excess probe through washing steps. Harnessing this property of SiR595, we synthesized and developed new red fluorogenic probes for labelling of HaloTagged proteins, F-Actin, microtubules, DNA and centrioles.

First, we demonstrated that SiR595 probes are fluorogenic, cell permeable and compatible with live-cell labelling (see Chapter 3). We then demonstrated the compatibility of SiR595 probes in multicolour live-cell imaging. We simultaneously imaged F-Actin and microtubules labelled with Lifeact-GFP, SiR595-Actin and SiR650-Tubulin in Ref52 cells. In addition, SiR595 is compatible with STED live-cell imaging. We demonstrated its STED compatibility by imaging axonal rings in rat hippocampal neurons labelled with SiR595-Actin, as well as by imaging of microtubules labelled with SiR595-Cabazitaxel. Dual colour STED imaging of live-cells was achieved by imaging of F-actin and microtubules labelled with either SiR595-Actin and SiR650-Tubulin or SiR595-Cabazitaxel and SiR650-Actin. Also, we successfully imaged exclusion zones of heterochromatin at nuclear pores (Nup107-SNAP-tag) labelled with SiR595-DNA and SiR650-BG. Developing such probes will complement already reported family of SiR650-based probes facilitating the multicolour live-cell imaging subcellular structures. It should be noted that during the preparation of this thesis, the Lavis lab reported the synthesis of SiR595 and its utility as SiR595-Halo probe. Our results are in concordance with this report.[110]

Next, we set out to develop a fluorogenic probe for live-cell labelling of centrioles (see Chapter 3). To target centrioles, we used a small molecule inhibitor Centrinone that binds to Plk4. First, we synthesized several SiR650-Centrinone probes varying linker length and the attachment handle. We demonstrated that SiR650-Centrinone probes bind to the same binding pocket as Centrinone with moderate loss of affinity in comparison to Centrinone. Next, we assessed labelling of SiR650-Centrinone probes in live cells and observed strong unspecific signal coming from lysosomes and/or endosomes. To address the entrapment problems stemming most probably from permeability issues, we synthesized several SiR595-Centrinone probes. They showed superior fluorogenicity and similar affinity towards Plk4-KD compared to SiR650-Centrinone probes. When probe **44c** was incubated with HeLa cells overexpressing GFP-Plk4(K41M), we observed that probe **44c** also stains cells with speckle like pattern of unspecific staining characteristic to lysosomes/endosomes, as well as that **44c** did not stain overexpressed GFP-Plk4(K41M). In the same conditions probe **44d** showed less unspecific labelling while staining the overexpressed GFP-Plk4(K41M). These observations lead us to believe that the probes are entrapped in lysosomes and/or endosomes due to the protonation of nitrogen found in piperazine derivatives **39a** and **39b** that were used as a handle to conjugate fluorophores. The acidic environment of lysosomes/endosomes then leads to a shift of SiR650 and SiR595 equilibrium to a fluorescent form resulting in observed unspecific labelling. To address these issues we used a piperidine derivative **39c** as a handle to conjugate SiR595 and synthesized probes **44e** and **44f**. *In-vitro* measurements showed that **44f** has stronger fluorogenic response in comparison to **44c**, **44d** and **44e**. Using **44f** we successfully imaged overexpressed GFP-Plk4 (K41M) arranged around centrioles with nine-fold symmetry. The diameter of the circular signal was measured to be 362 ± 21 nm (n= 8 of centrioles in 7 different cells). We believe that GFP-

Plk4 (K41M) localizes at the outer part of the torus, although it is not clear whether observed localization is intrinsic to Plk4 or it's an artefact of overexpression. Interestingly, it was reported that when Plk4 is inhibited with Centrinone, the amounts of Plk4 rise and seem to arrange in nine-fold symmetry.[126] Therefore, the observed nine-fold symmetry observed in our work may be a result of high amounts of GFP-Plk4 (K41M) caused by overexpression. Unfortunately, none of the generated probes were bright and fluorogenic enough to reliably label endogenous Plk4. The low expression levels of Plk4 and its labelling would require further development and optimization of the Centrinone-based probe.

In general, one of the disadvantages of ligand targeted labelling is the effect of the ligand on its target, in our case Centrinone and Plk4. Plk4 is particularly sensitive to alteration of its amounts and activity. As discussed long term inhibition of Plk4 causes loss of centrioles while overexpression leads to amplification of centrioles. Therefore, the best use of the optimized probe would be in short term STED imaging of Plk4 in live-cells that may provide more details of Plk4 dynamics throughout the cell cycle.

5.2   Future development

Regarding SiR595 based probes, one could envision the development of novel live-cell probes for organelles and/or proteins. One potentially interesting target would be focal adhesions. Recently, a small molecule inhibitor with high potency towards a focal adhesion kinase was published.[127] A probe based on this molecule would be an interesting approach towards labeling focal adhesions.

Further development of Centrinone based probes would involve testing novel fluorogenic fluorophores recently developed in our lab, more specifically fluorophores termed MAP555 and MAP618.[49] These fluorogenic fluorophores show strong fluorogenicity as well as very good permeability. With these novel probes we would aim to label Plk4 at endogenous levels in live-cells. Ideally, we could observe Plk4 localization over time in live-cells following the transition from a circular localization in G1 cell cycle phase into the dot like localization during G1/S phase. Also, it was shown that overexpression of Plk4, STIL or HsSAS-6 in cells leads to formation of multiple centrioles around the mother centriole.[122, 128-129] It would be of interest to label Plk4 and observe the localization of Plk4 during the formation of multiple centrioles in these conditions.

Finally, most of the inhibitors used as ligands in this thesis were designed and selected for their potency or effect on the function of the targeting protein and not solely for their affinity. An interesting challenge would be the development of ligands that bind to non-active sites of POI, e.g. a defined crevice on the protein surface. Weeding out high affinity binders with such properties could be used for the development of fluorogenic probes. The final goal would be to develop fluorogenic probes that could be used like small molecule antibodies.

6 Materials and Methods

6.1 General

All chemical reagents and anhydrous solvents for synthesis were purchased from commercial suppliers (Acros, Apollo, Armar, Bachchem, Biomatrik, Carbosynth, Fluka, Fluorochem, LC Laboratories, Merck, Reseachem, Roth, Sigma-Aldrich and TCI) and used without further purification. Halo-NHBoc was synthesized according to literature procedures.[130] Jasplakinolide-NHBoc was obtained from a custom synthesis by Spirochrome AG. Triflate **12** was ordered from ATT Bioquest (>95%). Composition of mixed solvents is given by volume ratio (v/v). Reactions in the absence of air and moisture were performed in oven-dried glassware under Ar or N2 atmosphere. Flash column chromatography was performed using a CombiFlash Rf system (Teledyne ISCO) using SiO2 RediSep® Rf columns at 25 °C or a Biotage (Isolera™) flash system using SiliaSep™ columns. The used solvent compositions are reported individually in parentheses. Analytical thin layer chromatography was performed on glass plates coated with silica gel 60 F254 (Merck). Visualization was achieved using UV light (254 nm). Evaporation in vacuo was performed at 25–60 °C and 900–10 mbar. 1H, 13C, and 19F NMR spectra were recorded on AV 400, Ascend™ 400 and AV 600 Bruker spectrometers at 400 MHz (1H), 101 MHz (13C) and 377 MHz (19F), respectively. All spectra were recorded at 298 K. Chemical shifts δ are reported in ppm downfield from tetramethylsilane using the residual deuterated solvent signals as an internal reference (CDCl3: δ H = 7.26 ppm, δ C = 77.16 ppm; CD3OD: δ H = 3.31 ppm, δ C = 49.00 ppm; DMSO-d6: δ H = 2.50 ppm, δ C = 39.52 ppm). For 1H, 13C and 19F NMR, coupling constants J are given in Hz and the resonance multiplicity is described as s (singlet), d (doublet), t (triplet), q (quartet), quint (quintet), sext (sextet), sept (septet), m (multiplet) and br. (broad). High-resolution mass spectrometry (HRMS) was performed by the MS-service of the EPF Lausanne (SSMI) on a Waters Xevo® G2-S Q-Tof spectrometer with electron spray ionization (ESI) or by the MS-facility of the Max Planck Institute for Medical Research on a Bruker maXis IITM ETD. Liquid chromatography coupled to mass spectrometry (LC-MS) was performed on a Shimadzu MS2020 connected to a Nexera UHPLC system equipped with a Waters ACQUITY UPLC BEH C18 (1.7 μm, 2.1 x 50 mm) column or a Supelco Titan C18 80 Å (1.9 μm, 2.1 x 50 mm). Buffer A: 0.05% HCOOH in H2O Buffer B: 0.05% HCOOH in ACN. Analytical gradient was from 10% to 90% B within 6 min with 0.5 mL/min flow unless otherwise stated. Preparative reverse phase high-performance liquid chromatography (RP-HPLC) was carried out on a Dionex system equipped with an UltiMate 3000 diode array detector for product visualization on a Waters Symmetry C18 column (5 μm, 3.9 x 150 mm), Waters SunFireTM Prep C18 OBDTM (5 μm, 10 x 150 mm) column, Supleco Ascentis® C18 column (5 μm, 10 x 250 mm) or on a Supleco Ascentis® C18 column (5 μm, 21.2 x 250 mm). Buffer A: 0.1% TFA in H2O Buffer B: ACN. Typical gradient was from 10% to 90% B within 32 min with 2, 4 or 8 mL/min flow.

6.2 Protocols

6.2.1 Extinction coefficient

SiR595-6'-COOH was dissolved in DMSO-*d6* and 1,2-dichloroethane(DCE) was added in concentration of 36.1 mM. The concentration was determined by ^{1}H-NMR. This solution was used to obtain a series of dilutions in EtOH + 0.1 % TFA. Absorbance was measured by UV-Vis spectrometry (JASCO V770 spectrophotometer) were performed from 500 nm to 750 nm. E_{max} was calculated using Lamberts-Beer law.

6.2.2   UV-Vis measurements

Solution of 5 µM substrate in TBS (20 mM Tris-HCl pH 7.4, 100 mM NaCl), TBS containing 1 mg/mL BSA, TBS containing 0.1 % SDS, ethanol or ethanol containing 0.1 % TFA were prepared. Absorbance spectra were recorded using a JASCO V770 spectrophotometer and small 1 cm quartz cuvettes with volume of 125 µL.

6.2.3   Quantum yields measurements

Solution of 200 nM SiR595-6'-COOH was made in EtOH + 0.1 % TFA. Quantum yields was determined using a Hamamatsu Quantaurus QY.

6.2.4   Dioxane titration

Solutions of 10 µM SiR595-6'-COOH and SiR650-COOH were prepared in water-dioxane mixtures containing 0 %, 10 %, 20 %, 30 %, 40 %, 50 %, 60 %, 70 %, 80 %, 90 % and 100 % of dioxane (v/v). The absorbance spectra were recorded using a plate reader (TECAN Spark® 20M) using polypropylene 96-well pates in 1 nm steps. The normalized absorbance at λ_{max} was plotted against the dielectric constant of dioxane/water mixtures and when permitted the inflection point was determined by using sigmoidal fitting in Originlab 8.1.[36]

6.2.5   Estimation of fluorescence increase

The probes analysed as described in Lukinavičius et al.[36] Briefly, SiR595 or SiR595-probes from a 1 mM DMSO (Applichem) stock solution was directly added to the target protein (0.4 mg/ml G-actin, 2 mg/ml monomeric tubulin or 10 µM HaloTag), to 0.1% SDS (Applichem GmbH) or to a bovine serum albumin (BSA) (Sigma) solution (0.4 mg/ml , 2 mg/ml or 1 mg/mL). Final concentration of the probes was 2 µM. In the case of tubulin probes, a buffer containing 80 mM piperazine-N,N'-bis(2-ethanesulfonic acid) sequisodium salt (PIPES) (Applichem), 2 mM MgCl$_2$, 0.5 mM ethylene glycol-bis(β-aminoethyl ether) N,N,N',N'-tetra-acetic acid (EGTA, pH 6.9) (Applichem), 1 mM GTP (Cytoskeleton) and 15% glycerol (Cytoskeleton) was used. In the case of actin probes, a buffer containing 5 mM Tris-HCl (pH 8.0), 0.2 mM CaCl$_2$ and 0.2 mM ATP was used. This buffer was supplemented with 50 mM KCl, 2 mM MgCl$_2$, 5 mM guanidine carbonate and 1 mM ATP to obtain F-actin. Both buffers are components of the actin polymerization fluorescence assay kit (Cytoskeleton). In the case of Halo-tag, a Tris buffer containing 20 mM Tris, 200 mM NaCl at pH 7.5 was used. The samples prepared in 1.5-ml tubes (Eppendorf) were incubated for 2–3 h at 37 °C, and fluorescence was measured in a 96-well plate (Greiner Bio-One) on a plate reader (TECAN Spark® 20M). Fluorescence emission was recorded from 570 nm to 750 nm for SiR595 probes, and 630 nm to 750 nm while exciting at 550 nm ± 10 nm for SiR595 probes and at 610 ± 10 nm for SiR650 probes. Fluorescence excitation scan was recorded by measuring the emission at 660 ± 10 nm for SiR595 and 720 ± 10 nm for SiR650 probes, while exciting from 500 nm to 640 nm for SiR595 probes and from 580 nm to 700 nm for SiR650 probes. All samples were prepared in triplicates. Ratios F(+SDS)/F(+BSA) or F(+target)/F(+BSA) of fluorescence signals at 620 nm for SiR595 probes and 670 nm for SiR650 probes and were calculated.

6.2.6   Fluorescence Polarization assay & competition assay

The solution of 1 nM Alexa488-Centrinone was titrated with increasing concentrations of Plk4-KD dissolved in 20 mM Tris pH 8.0, 200 mM NaCl, 0.2 mg/mL BSA in a black flat bottom 96-well plate (Greiner Bio-One). Upon mixture of protein and ligand, the plate was incubated for 30 min at room temperature followed by fluorescence polarization measurements. The fluorescence polarization was then measured by a plate reader (TECAN Spark® 20M) using 485 nm as excitation wavelength (bandwidth 20 nm) and 535 nm as emission wavelength (bandwidth 25 nm). Obtained fluorescence polarization values from each well were plotted

against the concentration of the protein. The apparent K_d values were obtained by fitting the curve to the following equation[118-119]:

$$FP = FP_{min} + \left(\frac{FP_{max} - FP_{min}}{2C_f}\right)\left(C_f + C_p + K_d - \sqrt{\left(C_f + C_p + K_d\right)^2 - 4C_f C_p}\right)$$

where FP_{min} is the minimum polarization value, FP_{max} is the maximum polarization value, C_f is the concentration of Alexa488-Centrinone and C_p is the concentration of the protein(Plk4-KD).

For competition assay, we have used the same amount of tracer, 1 nM Alexa488-Centrinone and 10 nM Plk4-KD. The amount of protein should be around the K_d of the tracer to ensure that enough free protein that can bind the competitor, and enough signal change coming from binding and unbinding of the tracer.[118-119] The solution of the tracer and protein was titrated with increasing amounts of competitors, in our case SiR650 and SiR595-Centrinone probes. The mixture was then incubated for an hour at room temperature and the FP was then measured on a plate reader using same conditions as mentioned before. From obtained FP values we have calculated amount of free protein in the solution for each concentration of competitor we used equation of the single-site binding isotherm[119]:

$$\left[P_{free}\right] = K_{d\_tracer}\ \frac{FP_{min} - FP}{FP - FP_{max}}$$

Where P_{free} is concentration of free protein, $K_{d\ tracer}$ represents the previously determined binding affinity of the tracer, FP_{min} is the minimum polarization value, FP_{max} is the maximum polarization value.

The obtained concertation of free protein was then fitted against the concentration of competitor and obtained curve was fitted by single site binding isotherm to determine the K_d of the protein towards the competitor:

$$FP = FP_{min} + \frac{FP_{max} - FP_{min}}{1 + \dfrac{K_{d,competitor}}{[Protein]}}$$

6.2.7   Cell Culture and Transfection

HeLa, U-2 OS (both ATCC), Ref52 Lifeact-GFP, U2OS H2B-Halo (produced by Michele Frei in our lab), U2OS Cep41-Halo (produced by Dr. Birgit Koch and Michelle Frei in our lab), HeLa Centrin1-GFP [131](gift from Gönczy lab, EPFL) and U2OS Nup107-Halo (generously provided by the Hell lab, MPI for medical research, Heidelberg) cells were cultured in high-glucose phenol red free DMEM (Life Technologies) medium supplemented with GlutaMAX (Life Technologies), sodium pyruvate (Life Technologies) and 10% FBS (Life Technologies) in a humidified 5% CO_2 incubator at 37 °C. Cells were split every 3–4 days or at confluency. These cell lines were regularly tested for mycoplasma contamination. Cells were seeded on glass bottom 35 mm dishes (Mattek or Greiner bio-one) or 10 well glass bottom dishes (Greiner bio-one) one day before imaging. For U2OS H2B-Halo-tag and Cep41-Cep41-HaloTag cell lines were incubated with 1 µg/mL of doxycycline for 24h to induce protein expression. Transient transfection of cells was performed using Lipofectamine™ 2000 reagent (Life Technologies) according to the manufacturer's recommendations: DNA (2.5 µg) was mixed with OptiMEM I (100 µL, Life Technologies) and Lipofectamine™ 2000 (6 µL) was mixed with OptiMEM I (100 µL). The solutions were incubated for 5 min at room temperature, then mixed and incubated for an additional 20 min at room temperature. The prepared DNA-Lipofectamine complex was added to a glass bottom 35 mm dish with cells

at 50–70% confluency. After 12 h incubation in a humidified 5% CO2 incubator at 37 °C the medium was changed to fresh medium. The cells were incubated for 24–48 h before imaging.

6.2.8   Staining of living and fixed cells

Live-cell staining with SiR595-probes was achieved by simply adding the probes from a 1 mM DMSO stock solution to the complete growth medium to obtain the desired final concentration (usually 100-500 nM) and incubating for 1 h in a humidified 5% CO_2 incubator at 37 °C. If required, Hoechst 33342 was added together with probes at the final concentration of 1 μg/ml.

Methanol fixation was performed as follows: growth medium was removed from cells, cells were incubated for 3–5min in −20 °C cold methanol and washed once with PBS followed by labeling with anti-GFP –STAR 635P nanobody for 30min. Cells were washed twice with PBS and imaged.

6.2.9   Preparation of hippocampal neurons

Cultures of hippocampal neurons were prepared from Wistar rats at postnatal day P0-P1 in accordance with the regulations of the German animal Welfare Act and under the approval of local veterinary service. Cells were plated on 100 μg/mL polyornithine (Sigma-Aldrich, cat. P3655) and 1 μg/mL Laminin (BD Bioscience, cat. 354232) coated coverslips. Neuronal cultures were maintained in NeuroBasal medium (Gibco, cat. 21103049) supplemented with 2% B27 serum-free supplement (Gibco, cat. 17504044), 2 mM L-Glutamine (Gibco, cat. 25030) and Pen/Strep (100 units/mL and 100 μg/mL respectively, BiochromAG, cat. A2213). The day after plating 5 μM cytosine β-D-arabinofuranoside (Sigma, cat. C1768) was added to the cultures. Medium was replaced once per week.

Live-cell staining of axonal rings in hippocampal neurons was achieved by first labelling of axonal marker neurofascin by incubating anti-neurofascin-A488 nanobody for 15 min. Upon nanobody labelling we incubated the neurouns for 45 min with SiR595-Actin (1 μM) probe. Cells were incubated in a humidified 5% CO2 incubator at 37°C. After washing, cells were imaged in artificial cerebrospinal fluid (ACSF buffer) at RT.

6.2.10   Protein amino acid sequence

MATCIGEKIEDFKVGNLLGKGSFAGVYRAESIHSGLEVAIKMIDKKAMYKAGMVQRVQNEVKIHCQLKHPSILELYNYFEDS NYVYLVLEMCHNGEMNRYLKNRVKPFSENEARHFMHQIITGMLYLHSHGILHRDLTLSNLLLTRNMNIKIADFGLATQLKM PHEKHYTLCGTPNYISPEIATRSAHGLESDVWSLGCMFYTLLIGRPPFDTDTVKNTLNKVVLADYEMPTFLSIEAKDLIHQLLR RNPADRLSLSSVLDHPFMSRNSSTKHHHHHHHHHH

Red: Plk4(2-272), Purple: His-tag

6.2.11   Expression, purification and characterization of Plk4-KD-6xHis

DNAs encoding fragments of Plk4 kinase domain (2-275) with 6xHis-tag were cloned in pET system vectors. The recombinant protein expression of the fragments was performed in *E. coli* strain BL21 gold (DE3) in LB medium. Protein expression was induced at 18 °C by addition of 0.3 mM IPTG and allowed to proceed for 18 hr. Cell pellets were lysed by lysozyme treatment and sonication, resuspended in lysis buffer containing 50 mM Tris (pH7.5), 400 mM NaCl, 2 mM $MgCl_2$, 5 mM EDTA, 1 mM DTT, 0.5 mM PMSF, 5% glycerol, 0.5% TritonX-100. Upon sonication, cells were centrifuged for 45 min at 4 C at 10000 rpm. Upon centrifugation protein was purified by AKTA system of purification using HisTrap HP (GElifesciences). Protein was loaded in lysis buffer, after which the column was wash with wash buffer (20mM Tris (pH 7.5), 1 mM DTT, 800mM

NaCl, 10% glycerol, 40 mM imidazole), to be finally eluted in elution buffer (20mM Tris (pH 7.5), 1 mM DTT, 400mM NaCl, 10% glycerol, 500 mM imidazole). Buffer was exchanged (20mM Tris (pH 7.5), 1 mM DTT, 200mM NaCl, 10% glycerol) by using spin columns and flash frozen and stored at -70 °C.

6.2.12 Confocal microscopy

Confocal imaging was performed on a Leica DMi8 microscope (Leica Microsystems) equipped with a Leica TCS SP8 X scanhead; a SuperK white light laser, a 355 nm CW laser (Coherent), a HC PL APO 63x1.47 oil objective or a HC PL APO 40.0x1.10 water objective; emissions for SiR595-probes were collected from 600 nm to 630 nm, and SiR650 from 670 nm to 750 nm. The microscope was equipped with a CO_2 and temperature controllable incubator (Life Imaging Services, 37 °C).

6.2.13 STED microscopy

STED microscopy mages were taken on a Abberior easy3D STED/RESOLFT QUAD scanning microscope (Abberior Instruments GmbH, Göttingen, Germany) built on a motorized inverted microscope IX83 (Olympus, Tokyo, Japan). Fluorophores were excited with a pulsed laser diode at 561 nm or 640-nm wavelength (PicoQuant). Fluorescence detector is an avalanche photodiode (APD). Microscope is equipped with 775 nm pulsed STED laser. The SiR595 signal was acquired using 590 nm to 630 nm detection window, and the SiR650 signal was acquired using a 660 nm to 750-nm detection window. A confocal channel with 485-nm excitation and 505 nm to 530 nm detection wavelengths were implemented to additionally image GFP. All images were acquired on 100x/1.40 UPlanSApo 100x/1.40 Oil 8/0.17/FN26.5 objectives. Pixel size, laser powers and dwell times were optimized for each sample.

6.3 Synthesis of SiR595-Probes

6.3.1 Compound 13
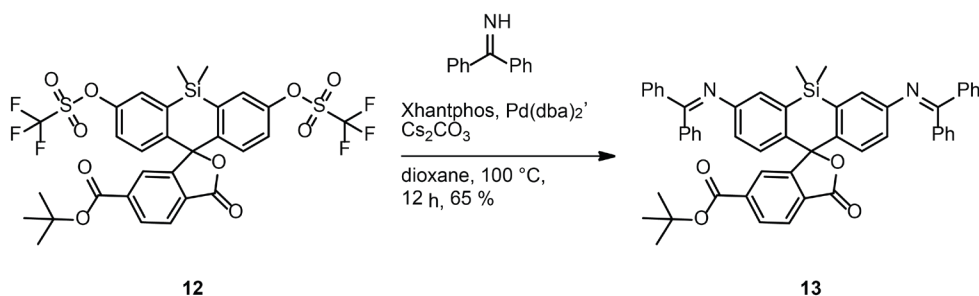
The 10 mL Schlenk flask was charged with caesium carbonate (132 mg, 406.0 µmol, 6 eq.), tris(dibenzylideneacetone)dipalladium(0) (6.2 mg, 6.8 µmol, 0.1 eq.), and 4,5-bis-diphenylphosphanyl-9,9-dimethyl-9H-xanthene (Xantphos, 7.8 mg, 13.5 µmol, 0.2 eq.). The flask was evacuated and backfilled with nitrogen 3×. Dry dioxane (1 mL) was added followed by another set of three cycles of evacuation and backfilling with nitrogen. The solution was stirred at room temperature for 10 min. To a separate vial, compound 12 (50 mg, 67.7 µmol, 1 eq.) and benzophenone imine (45 µL, 270 µmol, 4 eq.) were added in 0.5 mL of dioxane via a cannula. The reaction mixture was warmed to an internal temperature of 100 °C overnight (12 h). Cooling the reaction mixture to ambient temperature was followed by pouring the slurry into 100 mL of ethyl acetate. The organics were washed with 2 × 100 mL of water and 1 x 100 mL of brine. The ethyl acetate solution was concentrated in vacuo and the residue was dissolved in a minimal amount of DCM. Solution was loaded on silica-gel cartridge and purified by automated flash chromatography using gradient method (hexane/EA = 0-20-50-100 %). Fractions were collected and solvent was evaporated to yield compound 13 (35 mg, 65 %).

^{1}H NMR (400 MHz, CDCl$_3$-d) δ 8.07 (dd, J = 8.0, 1.3 Hz, 1H), 7.93 (dd, J = 8.0, 0.7 Hz, 1H), 7.77 − 7.71 (m, 4H), 7.59 (m, 1H), 7.50 − 7.45 (m, 2H), 7.40 (dd, J = 8.3, 6.7 Hz, 4H), 7.28 − 7.21 (m, 6H), 7.10 − 7.03 (m, 4H), 6.95 (d, J = 8.5 Hz, 2H), 6.86 (d, J = 2.3 Hz, 2H), 6.75 (dd, J = 8.6, 2.3 Hz, 2H), 1.56 (s, 9H), 0.38 (s, 3H), 0.12 (s, 3H).

^{13}C NMR (101 MHz, CDCl$_3$-d) δ 170.57, 169.18, 164.10, 156.36, 150.38, 139.47, 138.62, 137.56, 135.96, 134.44, 131.09, 130.20, 130.01, 129.57, 129.49, 128.91, 128.41, 128.38, 128.20, 127.18, 126.77, 126.34, 125.89, 124.21, 123.57, 89.97, 82.41, 28.22, -0.30, -0.62.

HR-MS (ESI): m/z calc. for C$_{53}$H$_{44}$N$_2$O$_4$Si [M+H]$^+$ 801.3070, found 801.3070.

6.3.2 Silicon-Rhodamine 595 (SiR595-6'-COOH) **14**
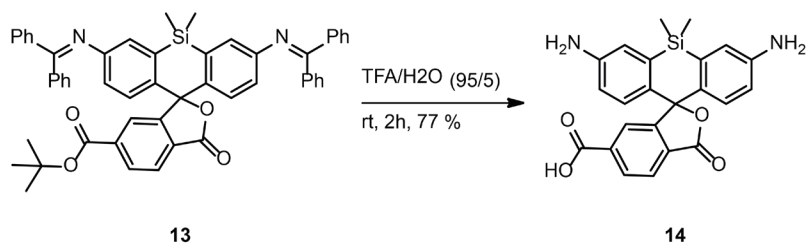
A 10 mL round bottom flask was charged with compound **13** (35 mg, 43.7 µmol, 1 eq.) which was dissolved in 1 mL of TFA/H_2O (95/5). The solution was mixed for 2 h at room temperature. Upon reaction completion, TFA was evaporated in vacuo and to residual compound/water mixture 2 mL of DMSO /H_2O (90/10) mixture was added. Solution was purified by RP-HPLC (8 mL/min, H_2O (0.1 % TFA)/ACN, 10-90 %). Collected fractions were frozen and lyophilized to obtain TFA salt of SiR595-6'-COOH **14** (18 mg, 77 %).

^{1}H NMR (400 MHz, DMSO-d_6) δ 8.16 (dd, J = 8.0, 1.4 Hz, 1H), 8.08 (d, J = 8.0 Hz, 1H), 7.72 (d, J = 1.1 Hz, 1H), 7.18 (m, 2H), 6.74 (m, 4H), 4.2 (broad peak, 4H), 0.60 (s, 3H), 0.51 (s, 3H).

^{13}C NMR (101 MHz, DMSO-d_6) δ 168.62, 165.80, 136.07, 132.64, 129.94, 128.25, 126.19, 124.54, 120.78, 120.11, 117.44, 117.20, 114.28, 100.08, 40.20, 39.91, 39.70, 39.49, 39.29, 39.08, 38.87, 38.66, -0.50, -1.47.

HR-MS (ESI): m/z calc. for $C_{23}H_{20}N_2O_4Si$ [M+H]$^+$ 417.1265, found 417.1265.

6.3.3   SiR595-Halo **16**
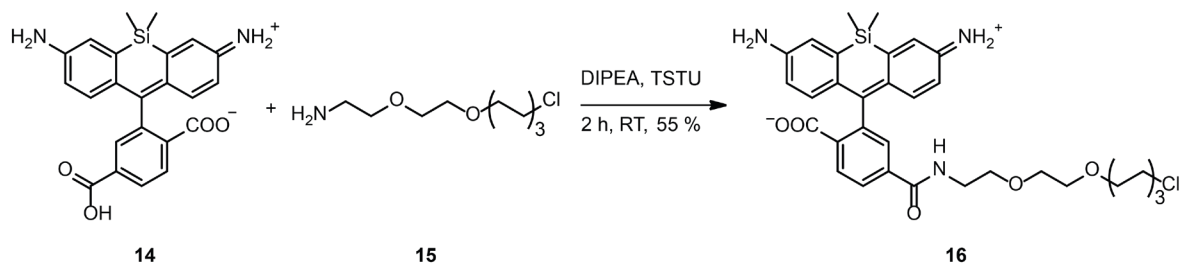
To solution of SiR595-6'-COOH **14** (500 µl of 15mM, 7.25 µmol, 1 eq.) in DMSO were successively added TSTU (250 µL of 100 mM, 8 µmol, 1.1 eq.) in DMSO and 10 µl DIEA. After 5 min, 80 µl of 0.1 M HaloTag ligand **15** in DMSO were added. The reaction was incubated 30 min at r.t. Then 50 µl H_2O and 50 µl acetic acid were added. The reaction was purified by RP-HPLC and lyophilized. The blue residue was dissolved in 0.5 mL DMSO to obtain 8 mM blue solution of SiR595-Halo **16** (55 % yield).

¹H-NMR (400 MHz, DMSO-d_6) δ 8.85 (t, J = 5.6 Hz, 1H), 8.14 (dd, J = 8.0, 1.4 Hz, 1H), 8.08 (d, J = 8.0 Hz, 1H), 7.77 (s, 1H), 7.10 (s, 2H), 6.68 – 6.57 (m, 4H), 4.09 (broad peak, 4H), 3.62 (t, J = 6.6 Hz, 3H), 3.54 (td, J = 5.7, 3.3 Hz, 5H), 3.52 – 3.42 (m, 4H), 3.43 (d, J = 5.7 Hz, 3H), 3.36 (t, J = 6.5 Hz, 3H), 1.75 – 1.63 (m, 2H), 1.45 (dq, J = 15.2, 8.7, 7.7 Hz, 3H), 1.43 – 1.29 (m, 4H), 1.34 – 1.21 (m, 4H), 0.60 (s, 3H), 0.51 (s, 3H).

HR-MS (ESI): m/z for calc. for $C_{33}H_{40}ClN_3O_5Si$ [M+H]$^+$ 622.2500, found 622.2499.

6.3.4   SiR595-C5-COOH **17**

14   **17**
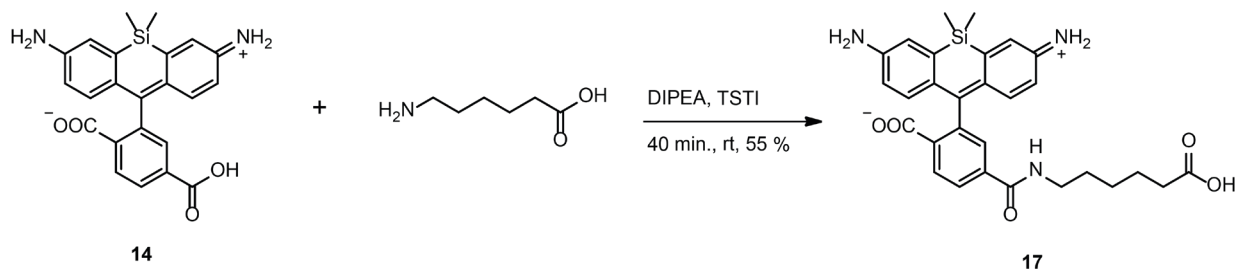
SiR595-6'-COOH **14** (100 µl of 12 mM solution in DMSO, 1.2 µmol, 1 eq.) was treated with DIEA (10 ul, 58 µmol, 48 eq.) and TSTU (14 µl of 100 mM solution in DMSO, 1.4 µmol, 1.2 eq.) were successively added. After 5 min, 6-aminohexanoic acid (24 µl of 100 mM solution in DMSO, 2.4 µmol, 2 eq.) was added. The mixture was incubated for 15 min at r.t. The mixture was incubated for 15 min at r.t. after which 100 µl of water and 100 µl of acetic acid was added until the pH was neutral and the reaction was purified by RP-HPLC and lyophilized. 200 µl of 4.0 mM solution of SiR595-C5-COOH **17** was obtained (55 % yield) as a blue solution.

¹H NMR (400 MHz, DMSO-d_6) δ 8.74 (t, J = 5.6 Hz, 1H), 8.10 (dd, J = 8.1, 1.4 Hz, 1H), 8.05 (d, J = 8.0 Hz, 1H), 7.72 (s, 1H), 7.12 (s, 2H), 6.72 – 6.58 (m, 4H), 4.12(broad peak, 4H), 3.22 (q, J = 6.7 Hz, 2H), 2.19 (t, J = 7.4 Hz, 2H), 1.50 (m, 4H), 1.28 (m, 2H), 0.58 (s, 3H), 0.49 (s, 3H).

¹³C NMR (101 MHz, DMSO-d_6) δ 174.88, 165.04, 128.71, 121.31, 117.82, 114.83, 34.03, 29.10, 26.49, 24.67, 0.34, -1.11. *Not all quaternary carbons from SiR595 observed

HR-MS (ESI): m/z for calc. for $C_{29}H_{31}N_3O_5Si$ [M+H]$^+$ 530.2106, found 530.2103.

6.3.5   SiR595-Actin 19
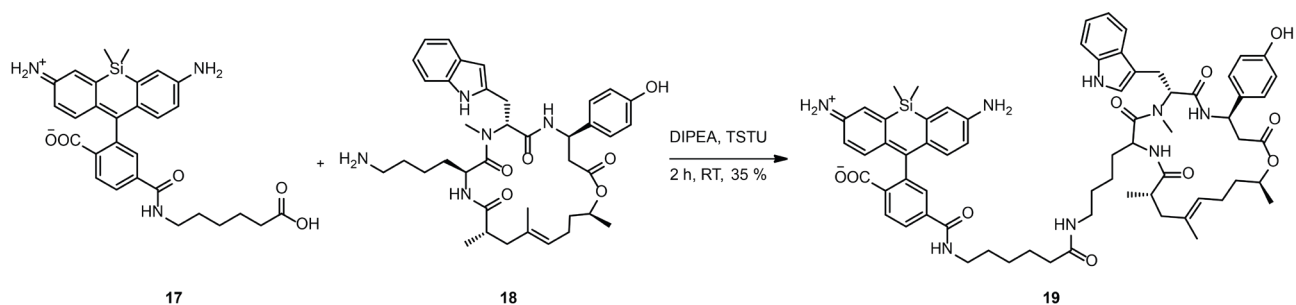
SiR595-C5-COOH **17** (283 µl of 10.0 mM solution in DMSO, 2.8 µmol, 1 eq.) was treated with DIEA (2.5 ul, 14.2 µmol, 5 eq.) and TSTU (34 µl of a 100 mM solution in DMSO, 3.4 µmol, 1.2 eq.). After 5 min, lysine modified depsipeptide **18** (28 µl of a 100 mM DMSO solution, 2.8 µmol, 1 eq.) was added. The mixture was incubated for 1 h at r.t. The product was retrieved by RP-HPLC, lyophilized and dissolved in dry DMSO to obtain 100 µl of 10 mM solution of SiR595-Actin **19** (35 % yield) as a light blue solution.

^{1}H NMR (400 MHz, DMSO-d_6) δ 10.82 (s, 1H), 8.74 (t, J = 5.6 Hz, 1H), 8.65 (d, J = 8.8 Hz, 1H), 8.10 (dd, J = 8.0, 1.4 Hz, 1H), 8.05 (d, J = 8.0 Hz, 1H), 7.75 – 7.62 (m, 4H), 7.29 (d, J = 8.0 Hz, 1H), 7.13 (m, 4H), 7.08 – 6.98 (m, 2H), 6.99 – 6.90 (m, 1H), 6.77 - 6.65 (m, 6H), 5.52 (dd, J = 11.3, 5.1 Hz, 1H), 5.19 (ddd, J = 11.5, 8.8, 3.1 Hz, 1H), 4.92 (t, J = 6.9 Hz, 1H), 4.67 (q, J = 6.4 Hz, 1H), 4.55 (m, 1H), 3.75 (broad peak, 4H), 3.22 (q, J = 6.7 Hz, 2Hz, 2H), 3.05 (m, 4H), 2.96-2.75(m, 4H), 2.72-2.54(m, 2H), 2.17 (dd, J = 14.9, 11.4 Hz, 1H), 2.02 (t, J = 7.5 Hz, 2H), 1.84 (m, 2H), 1.72 (d, J = 14.6 Hz, 1H), 1.49 (m, 8H), 1.33-1.42 (m, 2H), 1.28 – 1.18 (m, 2H), 1.16 (d, J = 6.4 Hz, 3H), 1.14 – 1.03 (m, 2H), 0.93 (d, J = 6.4 Hz, 3H), 0.79-0.84 (m, 3H), 0.59 (s, 3H), 0.49 (s, 3H).

^{13}C NMR (101 MHz, DMSO-$d6$) δ 174.95, 172.74, 172.39, 170.76, 170.51, 165.03, 156.70, 136.58, 133.58, 133.47, 128.72, 127.54, 127.42, 123.80, 123.45, 121.27, 119.10, 118.51, 115.53, 111.60, 110.00, 71.41, 55.07, 49.47, 48.13, 42.97, 42.13, 38.52, 38.09, 35.81, 35.33, 31.02, 29.19, 29.09, 26.67, 26.01, 25.54, 24.17, 22.51, 20.15, 19.92, 17.38, 0.31, -1.12.

HR-MS (ESI): m/z for calc. for $C_{67}H_{80}N_8O_{10}Si$ [M+2H]$^{2+}$ 593.2956, found 593.2957.

6.3.6 SiR595-C7-COOH 20

14   **20**
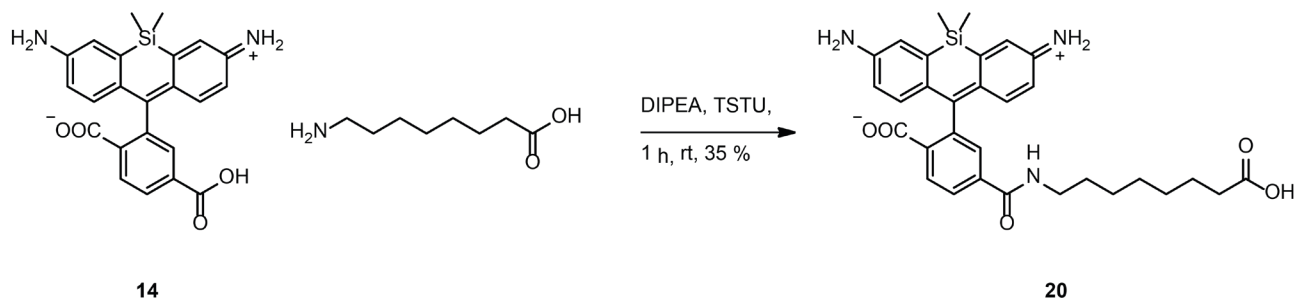
SiR595-COOH **14** (240 µl of a 20 mM solution in DMSO, 4.8 µmol, 1 eq.) was successively treated with DIPEA (4 µl, 24 µmol, 5 eq.) and TSTU (58 µl of 100 mM DMSO solution, 5.8 µmol, 1.2 eq.). After 5 min, 8-aminooctanoic acid (3.1 mg, 19.2 µmol, 4.0 eq.) was added. The reaction was sonicated for 1 h at r.t. Then water (50 µl) and acetic acid (50 µl) was added until the pH was neutral. The reaction was purified by RP-HPLC and lyophilized and dissolved in dry DMSO. 400 µl of 5.9 mM solution of **20** were obtained (37% yield) as a blue solution

^{1}H NMR (400 MHz, DMSO-d_6) δ 8.72 (t, J = 5.6 Hz, 1H), 8.11 – 8.03 (m, 2H), 7.71 (s, 1H), 7.15 (d, J = 2.2 Hz, 2H), 6.73 – 6.65 (m, 4H), 4.14 (broad peak, 4H), 3.21 (q, J = 6.6 Hz, 2H), 2.17 (t, pp$J$ = 7.3 Hz, 2H), 1.47 (q, J = 7.3, 6.4 Hz, 4H), 1.25 (t, J = 5.1 Hz, 8H), 0.58 (s, 3H), 0.49 (s, 3H).

HR-MS (ESI): m/z for calc. for $C_{31}H_{35}N_3O_5Si$ [M+H]$^+$, 558.2419, found 558.2420

6.3.7 SiR595-Cabazitaxel 22b

20   **11a-c**   **22a-c**
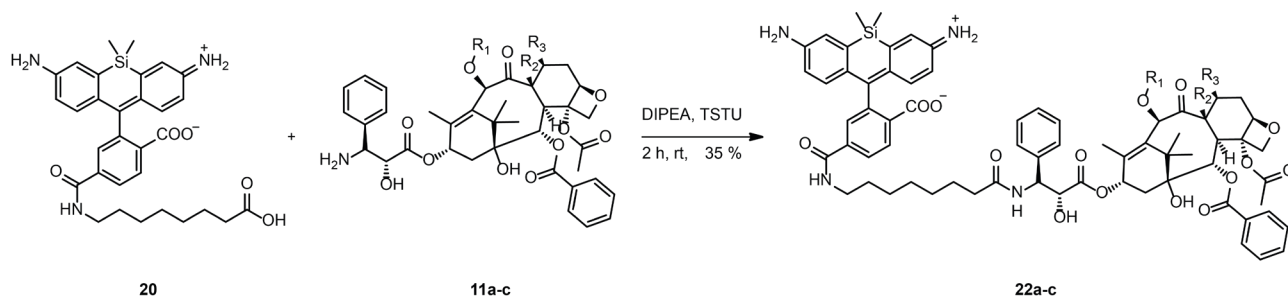
SiR595-C7-COOH (**20**) (90 µl of a 20 mM solution in DMSO, 1.8 µmol, 1 eq.) was treated with DIPEA (3 ul, 17.9 µmol, 10 eq.) and TSTU (22 µl of a 100 mM solution in DMSO, 2.2 µmol, 1.2 eq.). After 5 min, 3'-aminocabazitacel **11b** (54 µl of a 50 mM solution in DMSO, 2.7 µmol, 1.5 eq.) was added. The mixture was incubated 2h at r.t. The mixture was purified by RP-HPLC and lyophilized. The obtained powder was dissolved in DMSO to obtain 210 µl of 3 mM solution of SiR595-Cabazitaxel **22b** (35 % yield) as a light blue solution.

¹H NMR (400 MHz, DMSO-d_6): δ 8.71 (t, J = 5.6 Hz, 1H), 8.35 (d, J = 9.1 Hz, 1H), 8.08 (dd, J = 8.0, 1.4 Hz, 1H), 8.05 – 7.94 (m, 3H), 7.73 – 7.63 (m, 2H), p), 7.34 (ddd, J = 14.8, 8.3, 6.7 Hz, 4H), 7.24 – 7.14 (m, 1H), 7.02 (s, 2H), 6.56 (s, 4H), 5.94 (t, J = 9.0 Hz, 1H), 5.39 (d, J = 7.1 Hz, 1H), 5.28 (dd, J = 9.1, 5.7 Hz, 1H), 4.96 (d, J = 9.8 Hz, 1H), 4.70 (s, 1H), 4.64 (s, 1H), 4.42 (d, J = 5.7 Hz, 1H), 4.02 (s, 2H), 3.30 (s, 3H), 3.20 (d, J = 4.9 Hz, 6H), 2.25 (s, 2H), 2.19 – 2.10 (m, 2H), 1.97 (dd, J = 15.4, 9.2 Hz, 1H), 1.91 – 1.80 (m, 4H), 1.52 (m, 3H), 1.46 (m, 6H), 1.22 (m, 8H), 1.02 (s, 3H), 0.97 (s, 3H), 0.55 (s, 3H), 0.46 (s, 3H).

HR-MS (ESI): m/z for calc. for $C_{71}H_{82}N_4O_{16}Si$ [M+H]⁺, 1275.5568, found 1275.5563

6.3.8   SiR595-6'/5'-DNA **24a and 24b**
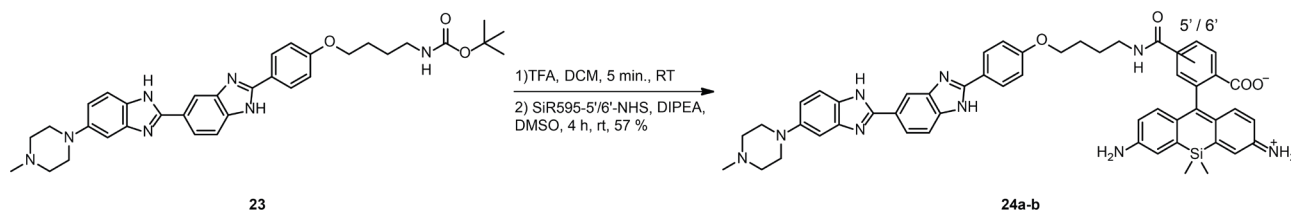
SiR595-6'-DNA was synthesized using a 2 step reaction starting from the Boc protected Hoechst derivative **23**. First, the Boc protecting group was removed by dissolving compound **23** (5 mg, 8.4 µmol) in 500 µl of 20 % TFA in DCM. The reaction mixture was stirred at r.t. for 5 min and then evaporated under a stream of N_2. The crude reaction mixture was dissolved in DMSO to a concentration of 20 mM (assuming full conversion) and used without further purification. A DMSO solution of SiR595-6'-NHS (390 µl of the 10 mM solution, 1 eq.) and treated with a deprotected compound **23**, a Hoechst-C_4-NH_2 in DMSO (290 µl, 10 mM, 1.5 eq.), and DIPEA (7 µl, 10 eq). The reaction mixture was stirred at r.t. for 4 h. The mixture was purified by RP-HPLC and lyophilized. The obtained powder was dissolved in DMSO to obtain 220 µl of 10 mM solution of SiR595-6'-DNA **25a** (57 % yield) as a light blue solution. The SiR595-5'-DNA **24b** was obtained using same protocol, although the obtained amounts were in sub < 0.3 mg amounts. Albeit, proper characterization of the compound was not performed.

Characterization of SiR595-6'-DNA

¹H NMR (400 MHz, DMSO-d_6): δ 10.02 z(s, 1H), 8.82 (t, J = 5.6 Hz, 1H), 8.45 (d, J = 1.7 Hz, 1H), 8.26 − 8.15 (m, 2H), 8.12 (dd, J = 8.1, 1.4 Hz, 1H), 8.09 − 8.00 (m, 2H), 7.89 (d, J = 8.6 Hz, 1H), 7.77 − 7.68 (m, 2H), 7.32 (dd, J = 9.1, 2.2 Hz, 1H), 7.23 (d, J = 2.1 Hz, 1H), 7.20 − 7.13 (m, 2H), 7.06 (d, J = 2.0 Hz, 2H), 6.68 − 6.55 (m, 4H), 4.11 (t, J = 6.2 Hz, 2H), 3.92 (d, J = 11.9 Hz, 2H), 3.59 (s, 2H), 3.33 (q, J = 6.6 Hz, 2H), 3.25 (s, 2H), 3.07 (s, 2H), 2.91 (s, 3H), 1.79 (dq, J = 11.2, 6.5 Hz, 2H), 1.70 (q, J = 7.1 Hz, 2H), 0.57 (s, 3H), 0.47 (s, 3H).

¹³C NMR (101 MHz, DMSO-d_6): δ 168.94, 164.74, 161.04, 154.07, 149.52, 148.34, 128.88, 128.26, 121.99, 120.59, 120.08, 117.66, 116.70, 115.11, 114.74, 114.55, 111.81, 99.43, 67.54, 52.35, 46.50, 42.10, 26.18, 25.59, -0.05, -1.59.

HR-MS (ESI): m/z for calc. for $C_{52}H_{51}N_9O_4Si$ [M+H]$^+$ 894.3906, found 894.3912.

6.4 Fluorophore-Centrinone synthesis

### 6.4.1 4,6-Dihydroxy-5-methoxy thiopyrimidine **27**
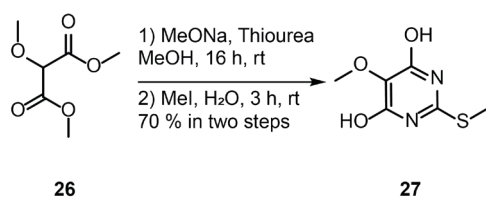
To a solution of dimethyl malonate **26** (200 mg, 2.23 mmol, 1.0 eq.) and thiourea (140 mg, 1.8 mmol, 1.5 eq.) in MeOH, a 20% sodium methoxide (170 mg, 3 mmol, 2.5 eq.) solution in methanol was added dropwise over 15 min at 0 °C, and the mixture was stirred at room temperature for 16 h. Upon reaction completion, MeOH was evaporated and the crude residue was dissolved in water (20 mL) before methyl iodide (270 mg, 120 µL,1.9 mmol, 1.5 eq.) was added, upon which the mixture was stirred at room temperature for 3 h. The reaction mixture was acidified with a HCl solution (6 M) to pH 3-4 and the product was allowed to precipitate. The precipitate was collected and mother liquor was acidified 3 times to precipitate all of the product. The collected precipitate was washed with water and dried on air to afford the desired product **27** as a snow white powder (163 mg, 70 %).

^{1}H-NMR (400 MHz, Methanol-d_4): δ 3.72 (s, 3H), 2.53 (s, 3H).

^{13}C-NMR (101 MHz, Methanol-d_4):δ 162.9, 157.4, 124.4, 60.3, 13.6.

HRMS (ESI): calc. $C_6H_9N_2O_3S$ [M+H]$^+$: 189.0328; found 189.0333

6.4.2 4,6-Dichloro-5-methoxy thiopyrimidine 28
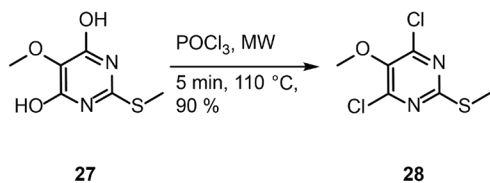
Compound **27** (500 mg, 2.66 mmol, 1.0 eq.) was added slowly into freshly distilled POCl$_3$ (4 mL) in a microwave vessel. The mixture was stirred at 110 °C for 5 min at 150 W in a microwave. Upon reaction, the reaction mixture was cooled to -20 °C and carefully quenched with ice. The product was extracted with EtOAc (3 x 20 mL) and the combined organic extracts were washed with brine, separated, dried over MgSO$_4$ and evaporated. The crude residue was dissolved in hexane and purified by flash column chromatography (hexane/DCM; gradient 0-50%) to obtain the desired product **28** as a beige powder (532 mg, 90%).

^{1}H-NMR (400 MHz, Chloroform-*d*): δ3.91 (s, 3H), 2.55 (s, 3H).

^{13}C-NMR (101 MHz, Chloroform-*d*): δ 167.0, 155.3, 143.6, 61.4, 15.0.

HR-MS (EI): calc. for C$_6$H$_7$Cl$_2$N$_2$OS [M+H]$^+$: 224.9651, 226.9626, 228.9596 ; found 224.9656, 226.9631, 228,9599

6.4.3 6-Chloro-5-methoxy-4-((methyl-*1H*-pyrazol-3-yl)amino)-2-(methylthio) pyrimidine **30**
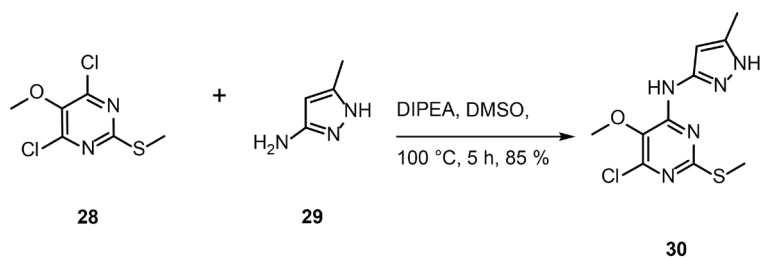
To a solution of compound **28** (40 mg, 118 μmol, 1.0 eq.) in DMSO, 5-methyl-*2H*-pyrazole-3-yl amine **29** (17 mg, 176 μmol, 1.5 eq.) and DIPEA (61 μL, 353 μmol, 3.0 eq.) were added. The reaction mixture was heated at 80 °C for 3 h before it was diluted with water (10 mL) and the product extracted with EtOAc (3 x 20 mL). The collected organic phase was washed with water and brine, separated, dried over $MgSO_4$ and evaporated. The crude residue was dissolved in EtOAc and purified by flash column chromatography (hexane/EtOAc; step gradient 0-100%) to obtain the desired product **30** as a brown powder (30 mg, 85%)

^{1}H NMR (400 MHz, Methanol-d_4): δ 6.45 (s, 1H), 3.86 (s, 3H), 2.51 (s, 3H), 2.29 (s, 3H).

^{13}C-NMR (101 MHz, Chloroform-*d*): δ 167.3, 155.9, 150.1, 133.7, 98.0, 58.3, 18.4, 14.8.

HRMS (ESI): calc. for $C_{10}H_{13}ClN_5OS$ [M+H]$^+$: 286.0529, 288.0500; found 286.0523, 288.0497

6.4.4 6-Chloro-5-methoxy-4-((5-methyl-1H-pyrazol-3-yl)amino)-2-(methylsulfonyl) pyrimidine 31
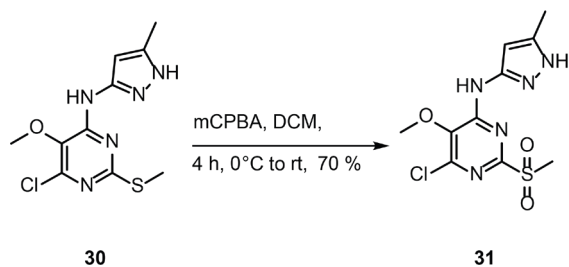
To a stirred solution of pyrimidine methyl sulfide **30** (250 mg, 0.87 mmol, 1 eq.) in DCM at 0 °C, a DCM solution of *m*CPBA (77% wt) (392 mg, 1.75 mmol, 2.0 eq.) was added. The reaction mixture was let warm up to r.t. and was stirred for 4 h. Upon completion, the mixture was diluted with DCM and washed with 50 % solution of NaS_2O_3/$NaHCO_3$ (3 x 50 mL). The organic phase was washed with water and brine, separated, dried over $MgSO_4$ and evaporated. The crude residue was dissolved and purified flash column chromatography (hexanes/EtOAc; step gradient 0-100%) to obtain the desired product **31** as white title powder (200 mg, 72 %).

¹H NMR (400 MHz, DMSO-*d6*): δ 10.38 (s, 1H), 6.47 (d, *J* = 0.8 Hz, 1H), 3.87 (s, 3H), 3.32 (s, 3H), 2.26 (s, 3H).

¹³C NMR (101 MHz, DMSO-*d6*): δ 158.90, 155.52, 148.57, 146.36, 139.48, 137.70, 97.45, 61.24, 11.34.

HRMS (ESI): calc. for $C_{10}H_{12}ClN_5O_3S$ [M+H]⁺: 318.0422; found 318.0420

6.4.5   1-(Bromomethyl)-2-fluoro-3-nitrobenzene **33**
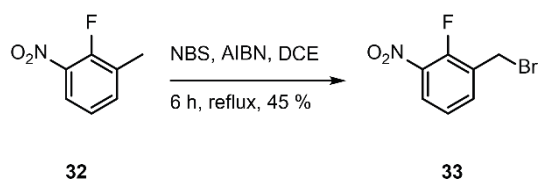
To a stirring solution of 1-methyl-2-fluoro-3-nitrobenzene **32** (2 g, 12.9 mmol, 1 eq.) and NBS (2.75 g, 15.5 mmol, 1.2 eq.), in 100 mL of DCE, was added AIBN (423 mg, 2.6 mmol, 0.2 eq.). The mixture was stirred under reflux for 6 h. The reaction mixture was cooled to r.t., diluted with DCM and washed with water, sat. NaHCO$_3$ and brine. To the organic phase silica gel was added to obtain silica dry load upon solvent evaporation. Silica gel loaded with the compound was purified by flash chromatography (haxane/DCM; step gradient 0-2.5-5-10-50 %) to obtain the desired product **33** as yellow oil (1.36 g, 45 %)

¹H NMR (400 MHz, Chloroform-*d*) δ 8.01 (ddd, *J* = 8.5, 7.0, 1.8 Hz, 1H), 7.71 (ddd, *J* = 7.9, 6.3, 1.8 Hz, 1H), 7.30 (td, *J* = 8.1, 1.3 Hz, 1H), 4.55 (d, *J* = 1.5 Hz, 2H).

¹³C NMR (101 MHz, Chloroform-*d*) δ 153.60 (d, *J* = 267.8 Hz), 137.97, 136.64 (d, *J* = 3.7 Hz), 128.72 (d, *J* = 13.9 Hz), 126.35 (d, *J* = 2.6 Hz), 124.63 (d, *J* = 5.3 Hz), 23.74 (d, *J* = 5.5 Hz).

6.4.6 4-Bromo-2-fluoro-1-(*tert*-butylthio) benzene **35**
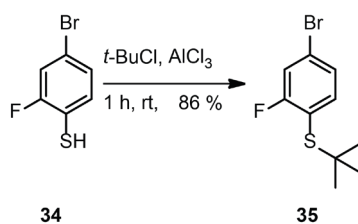
To the ice cooled solution of thiophenol **34** (2 g, 9.7 mmol, 1 eq.) in 10 mL of t-BuCl, AlCl$_3$ (257 mg, 1.9 mmol, 0.2 eq.) was added in small portions. Evolved HCl was lead through solution of 2 M NaOH. Upon addition of AlCl$_3$, the ice bath was removed and reaction was stirred for 1h on r.t. Reaction mixture was poured into water and extracted with hexanes (3 x 20 mL). The pooled organic phases were washed with water, brine, dried over of an anh. MgSO$_4$ and filter. Prior to evaporation of organic phase, silica gel was added to form silica cake. Silica gel loaded with a compound was purified by flash chromatography (hexanes; isocratic) to obtain desired product **35** as colourless oil (2.2 g, 86 %).

^{1}H NMR (400 MHz, Chloroform-*d*) δ [ppm] = 7.50 (dd, *J* = 8.2, 7.3 Hz, 1H), 7.29 (dd, *J* = 8.6, 2.0 Hz, 1H), 7.18 (ddd, *J* = 8.2, 1.9, 0.8 Hz, 1H), 1.30 (s, 9H).

^{13}C NMR (101 MHz, Chloroform-*d*) δ [ppm] = 164.04 (d, J = 250.9 Hz), 141.11, 127.58 (d, J = 4.1 Hz), 124.11 (d, J = 9.0 Hz), 119.74 (d, J = 27.9 Hz), 119.20 (d, J = 19.1 Hz), 47.65, 31.02.

6.4.7 *tert*-Butyl (2-fluoro-4-((2-fluoro-3-nitrobenzyl) sulfonyl) phenyl) sulfane **37**
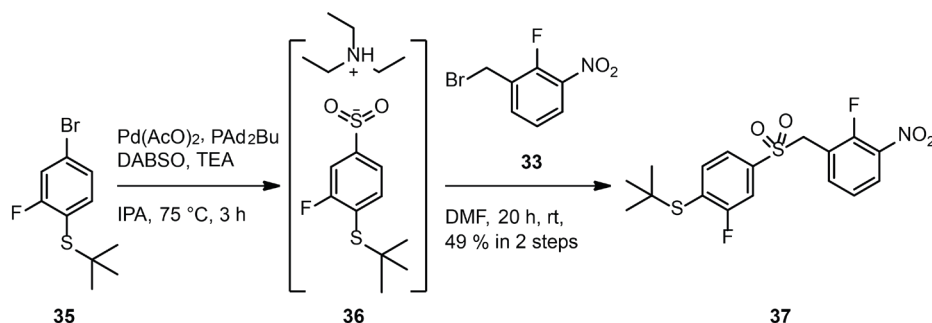
A glass tube was charged with DABSO (274 mg, 0.12 mmol, 0.6 eq.), palladium(II) acetate (43 mg, 190 µmol, 0.1 eq.) and CataCXium A® (136 mg, 380 µmol, 0.2 eq.), sealed with a rubber septum and evacuated and filled with nitrogen four times. Aryl bromide **35** (500 mg, 1.9 mmol, 1.0 eq.), anhydrous triethylamine (777 µL, 5.7 mmol, 3.0 eq.) and anhydrous 2-propanol (5 mL) were added sequentially through the septum and the =mixture stirred under positive pressure of nitrogen in a preheated oil bath at 75 °C for 16 h Reaction was monitored by LC-MS, and when most of the starting material was transformed into sulfinic salt **36**, the solution was cooled to room temperature, and anh. DMF (~15 mL) solution of benzyl bromide **33** (533 mg, 2.3 mmol, 1.2 eq.) was added dropwise and the solution stirred at the same temperature for 6 h. Upon completion, the mixture was poured onto water (50 mL) and extracted with EtOAc (3 x 50 mL). The combined organic fractions were dried over MgSO₄, filtered and evaporated. Flash column chromatography (hexane/ EtOAc, 0–100 % gradient) afforded the titled sulfone **37** as a pale yellow solid (380 mg, 49 %).

¹H NMR (400 MHz, Chloroform-*d*) δ 8.06 (ddd, *J* = 8.6, 7.0, 1.8 Hz, 1H), 7.74 (ddd, *J* = 7.8, 6.0, 1.8 Hz, 1H), 7.68 (dd, *J* = 7.9, 6.6 Hz, 1H), 7.46 (dd, *J* = 7.3, 1.9 Hz, 1H), 7.43 (dd, *J* = 8.0, 2.0 Hz, 1H), 7.36 (td, *J* = 8.1, 1.3 Hz, 1H), 4.50 (d, *J* = 1.1 Hz, 2H), 1.32 (s, 9H).

¹³C NMR (101 MHz, Chloroform-*d*) δ 163.70 (d, *J* = 252.8 Hz), 153.94 (d, *J* = 267.1 Hz), 139.67 (d, *J* = 6.4 Hz), 138.19 (d, *J* = 3.3 Hz), 137.78, 129.11 (d, *J* = 19.2 Hz), 127.29 (d, *J* = 2.4 Hz), 124.81 (d, *J* = 5.2 Hz), 123.72 (d, *J* = 4.4 Hz), 119.12 (d, *J* = 13.9 Hz), 116.06 (d, *J* = 28.1 Hz), 55.20 (d, *J* = 2.9 Hz), 49.05, 31.13.

¹⁹F-NMR (376 MHz, Chloroform-*d*): δ -108.39 (d, *J* = 2.7 Hz), -122.09 (d, *J* = 2.7 Hz).

HRMS (ESI): calc. for C₁₇H₁₇F₂NO₄S₂ [M+Na]⁺: 424.0465; found 424.0459

6.4.8   6-chloro-2-((2-fluoro-4-((2-fluoro-3-nitrobenzyl)sulfonyl)phenyl)thio)-5-methoxy-4-((5-methyl-1H-pyrazol-3-yl)amino) pyrimidine 38
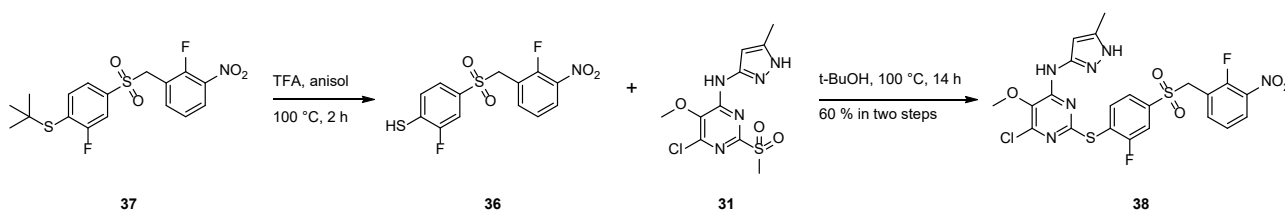
A reaction tube was charged with sulfone **37** (40 mg, 100 µmol, 1.3 eq.) and carefully dissolved in pure TFA followed by addition of anisole (21.66 mg, 200 µmol, 2.6 eq.). The flask was sealed, air was exchanged with argon multiple times and the reaction mixture was heated to 100 °C for 2 h. Upon reaction completion, the mixture was cooled down to room temperature and TFA was evaporated. The crude was kept under argon, before the dissolved methyl sulfone **31** (27 mg, 85 µmol, 1.0 eq.) in *tert*-butanol (10 mL) was added. The mixture was sealed and heated at 100 °C overnight under argon. Upon completion, the solvent was evaporated and crude was purified via RP-HPLC (H$_2$O\ACN = gradient 10–90 % (50 min.)) to afford the titled sulfone **38** as a pale yellow TFA salt (28 mg, 60 %).

^{1}H NMR (400 MHz, DMSO-d_6) δ 9.81 (s, 1H), 8.18 (ddd, J = 8.6, 7.1, 1.8 Hz, 1H), 8.00 (dd, J = 8.1, 6.8 Hz, 1H), 7.84 (dd, J = 8.1, 1.9 Hz, 1H), 7.67 (dd, J = 8.1, 1.9 Hz, 1H), 7.65 – 7.58 (m, 1H), 7.45 (t, J = 8.0 Hz, 1H), 5.45 (d, J = 0.8 Hz, 1H), 5.02 (s, 2H), 3.76 (s, 2H), 2.05 (s, 3H).

^{13}C NMR (101 MHz, DMSO-d_6) δ 161.63 (d, J = 252.4 Hz), 161.16, 154.47, 153.47 (d, J = 265.9 Hz), 148.41, 145.78, 141.06 (d, J = 6.7 Hz), 139.03 (d, J = 3.8 Hz), 138.87, 138.04, 137.33 (d, J = 8.0 Hz), 133.33, 127.02 (d, J = 2.2 Hz), 124.94 (d, J = 4.8 Hz), 124.80 (d, J = 3.9 Hz), 124.22 (d, J = 18.4 Hz), 118.87 (d, J = 14.2 Hz), 115.97 (d, J = 26.4 Hz), 96.00, 60.69, 54.10, 10.80.

^{19}F NMR (376 MHz, DMSO-d_6) δ -102.18 (t, J = 7.4 Hz), -121.97 (t, J = 6.9 Hz).

**HRMS (ESI):** calc. for C$_{22}$H$_{17}$ClF$_2$N$_6$O$_5$S$_2$ [M+H]$^+$: 583.0431, found 583.0436.

6.4.9 *tert*-Butyl-2-(4-(2-((2-fluoro-4-((2-fluoro-3-nitrobenzyl)sulfonyl)phenyl)thio)-5-methoxy-6-((5-methyl-1H-pyrazol-3-yl)amino)pyrimidin-4-yl)piperazin-1-yl)acetate **40a**
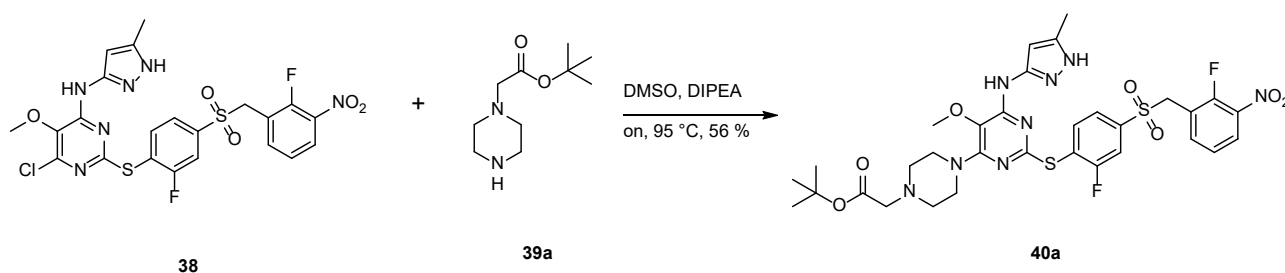
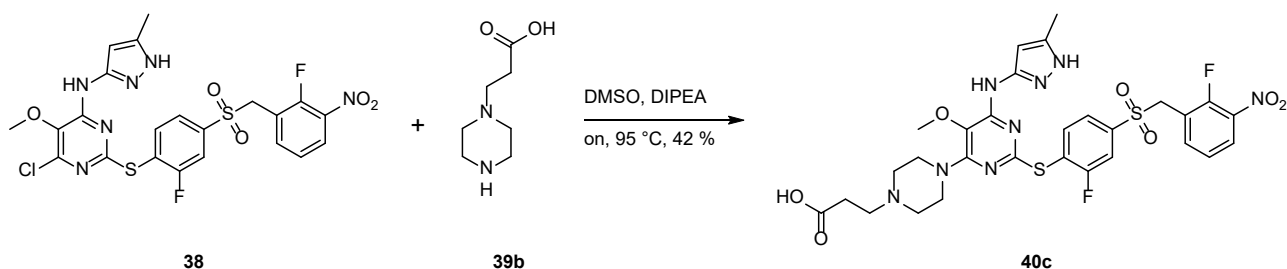Compound **38** (7 mg, 12 µmol, 1.0 eq.) was dissolved in anh. DMSO (1 mL) then piperazine derivative **39a** (2.9 mg, 14 µmol, 1.2 eq.) and DIPEA (2.3 mg, 18 µmol, 1.5 eq.) was added to the solution. The mixture was heated at 95 °C overnight. Upon cooling, the mixture was acidified with acetic acid (200 µL), followed by adding water (200 µL) before purification by RP-HPLC (ACN/H$_2$O; gradient 10-90%). Corresponding fractions were collected, frozen and lyophilized overnight to obtain the desired product **40a** as TFA salt in form of a white powder (5 mg, 56 %).

^{1}H NMR (400 MHz, Chloroform-*d*) δ 10.11 (s, 1H), 8.08 (ddd, *J* = 8.5, 7.0, 1.7 Hz, 1H), 7.84 (dd, *J* = 8.3, 6.4 Hz, 1H), 7.74 (ddd, *J* = 7.7, 5.9, 1.7 Hz, 1H), 7.56 (td, *J* = 7.7, 1.8 Hz, 2H), 7.44 – 7.32 (m, 1H), 6.01 (s, 1H), 4.54 (s, 2H), 4.02 (s, 4H), 3.79 (s, 2H), 3.66 (s, 3H), 3.36 (s, 4H), 2.66 (s, 2H), 2.25 (s, 3H), 1.46 (s, 10H).

6.4.10 2-(4-(2-((2-fluoro-4-((2-fluoro-3-nitrobenzyl)sulfonyl)phenyl)thio)-5-methoxy-6-((5-methyl-1H-pyrazol-3-yl)amino)pyrimidin-4-yl)piperazin-1-yl)acetic acid **40b**

40a   DCM, TFA / 15 min, rt, 90 %   **40b**
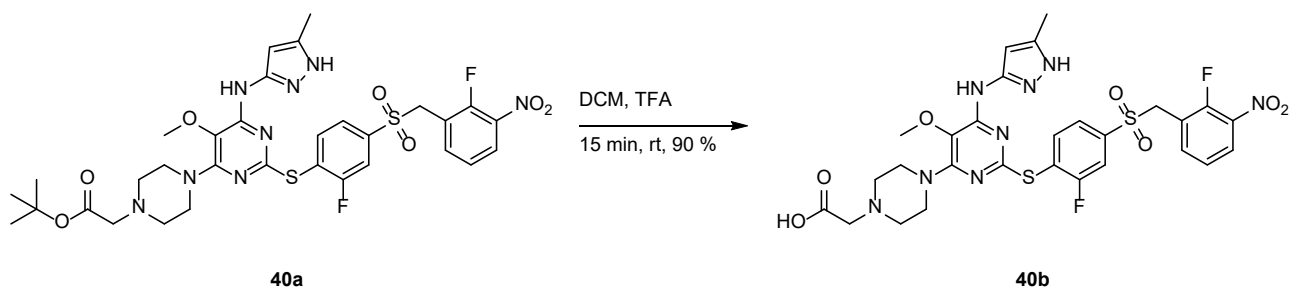
Compound **40a** (5 mg, 6.7 µmol, 1 eq.) was dissolved in DCM containing 20 % of TFA. Reaction was stirred for 15 min. upon which DCM/TFA mixture was evaporated under vacuum. The residue was dissolved and purified by RP-HPLC (ACN/H_2O; gradient 10-90%). Corresponding fractions were collected, frozen and lyophilized overnight to obtain the desired product **40b** as TFA salt in form of a white powder (4.2 mg, 90 %).

^{1}H NMR (400 MHz, DMSO-d_6) δ [ppm] = 8.93 (s, 1H), 8.18 (ddd, J = 8.6, 7.1, 1.8 Hz, 1H), 7.96 (dd, J = 8.1, 6.8 Hz, 1H), 7.82 (dd, J = 8.1, 1.9 Hz, 1H), 7.65 (ddd, J = 8.1, 6.1, 1.8 Hz, 2H), 7.46 (t, J = 8.0 Hz, 1H), 5.48 (s, 1H), 5.01 (s, 2H), 4.15 (zs, 2H), 3.96 (broad peak, 4H), 3.57 (s, 3H), 3.34 (broad peak, 4H), 2.04 (s, 3H).

^{13}C NMR (101 MHz, DMSO-d_6) δ [ppm] = 167.74, 163.31, 160.59 (d, J = 44.4 Hz), 154.76 (d, J = 87.5 Hz), 153.01 (d, J = 90.6 Hz), 146.89, 141.18 (d, J = 6.9 Hz), 139.02 (d, J = 105.7 Hz), 137.76 (d, J = 8.1 Hz), 127.47, 125.65, 125.43 (d, J = 5.6 Hz), 125.06, 123.32, 119.28, 118.18, 116.21 (d, J = 26.5 Hz), 115.25, 95.77, 59.24, 55.74, 54.57, 51.87, 42.90, 11.40.

^{19}F NMR (376 MHz, DMSO-d_6) δ [ppm] = -102.27 (t, J = 7.4 Hz), -122.12 (d, J = 6.7 Hz).

6.4.11 3-(4-(2-((2-fluoro-4-((2-fluoro-3-nitrobenzyl)sulfonyl)phenyl)thio)-5-methoxy-6-((5-methyl-1H-pyrazol-3-yl)amino)pyrimidin-4-yl)piperazin-1-yl)propanoic acid **40c**
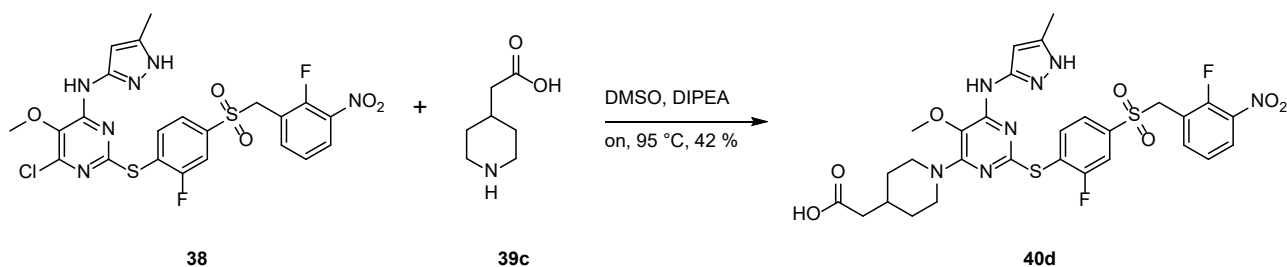

Compound **38** (13 mg, 22 µmol, 1.0 eq.) was dissolved in anh. DMSO (1 mL) then piperazine derivative **39b** (5.3 mg, 33 µmol, 1.5 eq.) and DIPEA (14 mg, 111 µmol, 5 eq.) was added to the solution. The mixture was heated at 95°C overnight. Upon cooling, the mixture was acidified with acetic acid (200 µL), followed by adding water (200 µL) before purification by RP-HPLC (ACN/H_2O; gradient 10-90%). Corresponding fractions were collected, frozen and lyophilized overnight to obtain the desired product **40c** as TFA salt in form of white powder (7 mg, 45 %).

^{1}H NMR (400 MHz, DMSO-d_6) δ 9.69 (s, 1H), 8.92 (s, 1H), f8.18 (ddd, J = 8.6, 7.1, 1.8 Hz, 1H), 7.97 (dd, J = 8.1, 6.8 Hz, 1H), 7.82 (dd, J = 8.0, 1.9 Hz, 1H), 7.72 – 7.60 (m, 3H), 7.47 (t, J = 8.0 Hz, 1H), 5.49 (s, 1H), 5.02 (s, 2H), 3.70 (broad peak, 4H), 3.58 (s, 3H), 3.36 (t, J = 7.4 Hz, 2H), 3.15 (broad peak, 4H), 2.77 (t, J = 7.4 Hz, 2H), 2.05 (s, 3H).

^{13}C NMR (101 MHz, DMSO-d_6) δ 171.96, 162.07 (d, J = 252.0 Hz), 160.35, 153.87 (d, J = 265.6 Hz), 153.86 (d, J = 93.1 Hz), 146.91, 141.18 (d, J = 6.9 Hz), 139.55, 138.50, 137.76 (d, J = 7.8 Hz), 127.48, 125.66, 125.48, 125.05, 123.28, 119.35 (d, J = 14.3 Hz), 116.20 (d, J = 26.4 Hz), 95.76, 59.31, 54.57, 51.93, 51.36, 43.19, 28.96, 11.40.

^{19}F NMR (376 MHz, DMSO-d_6) δ -102.29 (t, J = 6.9 Hz), -122.14 (t, J = 6.7fHz).

HRMS (ESI): calc. for $C_{29}H_{29}F_2N_7O_7S_2$ [M+H]$^+$: 690.1611; found 690.1614.

6.4.12 f2-(1-(2-((2-fluoro-4-((2-fluoro-3-nitrobenzyl)sulfonyl)phenyl)thio)-5-methoxy-6-((5-methyl-1H-pyrazol-3-yl)amino)pyrimidin-4-yl)piperidin-4-yl) acetic acid **40d**


Compound **38** (10 mg, 17 µmol, 1.0 eq.) was dissolved in anh. DMSO (1 mL) then piperidine derivative **39c** (3.7 mg, 26 µmol, 1.5 eq.) and DIPEA (11 mg, 86 µmol, 5 eq.) was added to the solution. The mixture was heated at 95°C overnight. Upon cooling, the mixture was acidified with acetic acid (200 µL), followed by addition of water (200 µL) before purification by RP-HPLC (ACN/H_2O; gradient 10-90%). The corresponding fractions were collected, frozen and lyophilized overnight to obtain the desired product **40d** as TFA salt in form of white powder (5 mg, 42 %).

^{1}H NMR (400 MHz, DMSO-d_6) δ 8.94 (s, 1H), 8.17 (ddd, J = 8.6, 7.1, 1.8 Hz, 1H), 7.96 (dd, J = 8.1, 6.8 Hz, 1H), 7.81 (dd, J = 8.1, 1.9 Hz, 1H), 7.68 – 7.61 (m, 2H), 7.45 (t, J = 8.0 Hz, 1H), 5.64 (s, 1H), 5.01 (s, 2H), 4.18 (d, J = 13.0 Hz, 3H), 3.54 (s, 3H), 2.81 (td, J = 12.9, 2.4 Hz, 2H), 2.15 (d, J = 6.9 Hz, 2H), 2.09 (s, 3H), 1.88 (ddd, J = 11.1, 7.2, 3.8 Hz, 0H), 1.69 – 1.61 (m, 2H), 1.14 (qd, J = 12.5, 3.8 Hz, 2H).

^{13}C NMR (101 MHz, DMSO-d_6) δ 173.40, 162.87, 160.37, 159.56, 154.22 (d, J = 111.2 Hz), 152.68 (d, J = 111.1 Hz), 145.90, 140.64 (d, J = 6.7 Hz), 140.41, 139.06, 138.03, 137.32 (d, J = 8.0 Hz), 127.01, 125.46 (d, J = 18.5 Hz), 124.95 (d, J = 4.8 Hz), 124.47, 122.15, 118.91 (d, J = 14.4 Hz), 115.61 (d, J = 26.5 Hz), 95.14, 58.66, 54.04, 45.61, 40.50, 32.58, 31.48, 11.04.

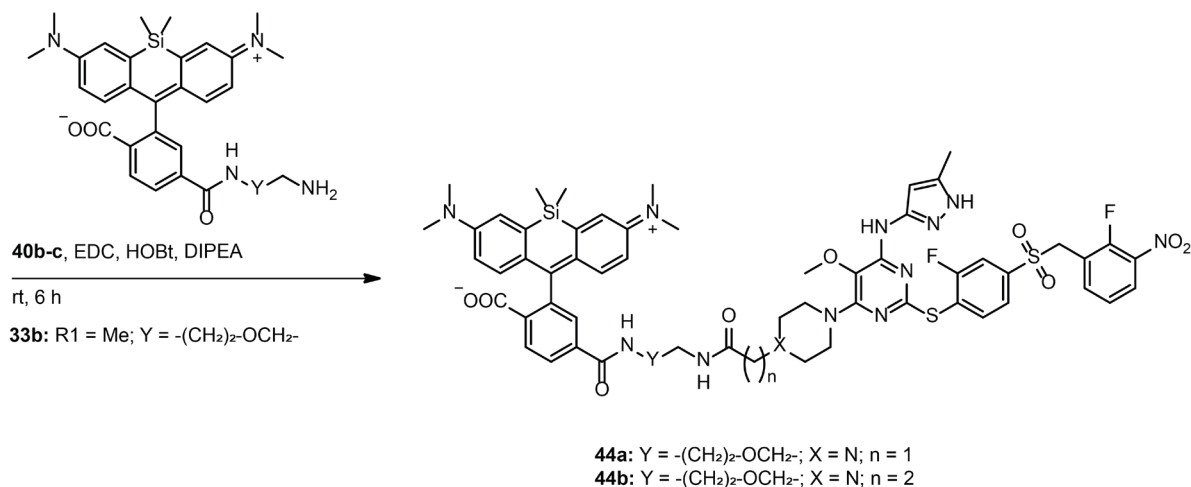**^{19}F NMR** (376 MHz, DMSO-d_6) δ -102.31(t, J = 7.4 Hz, -122.02(t, J = 6.9 Hz).

HRMS (ESI): calc. for $C_{29}H_{29}F_2N_7O_7S_2$ [M+H]$^+$: 690.1611; found 690.1614.

6.4.13 SiR650 – linker **43a** & **43b**

43a: Y = -(CH₂)₃-
43b: Y = -(CH₂)₂-OCH₂-
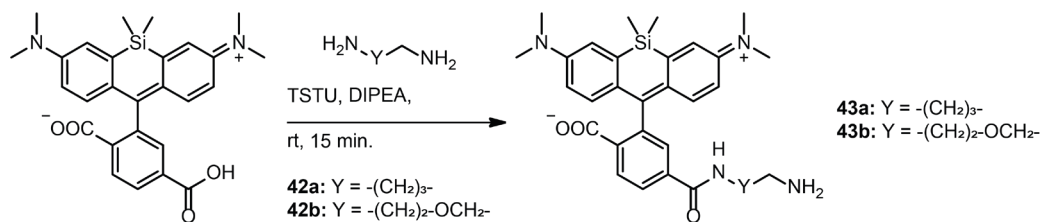
These compounds were synthesized according to published literature.[132]

6.4.14 SiR595 - linker **43c** & **43d**

43c: Y = -(CH₂)₃-
43d: Y = -(CH₂)₂-OCH₂-
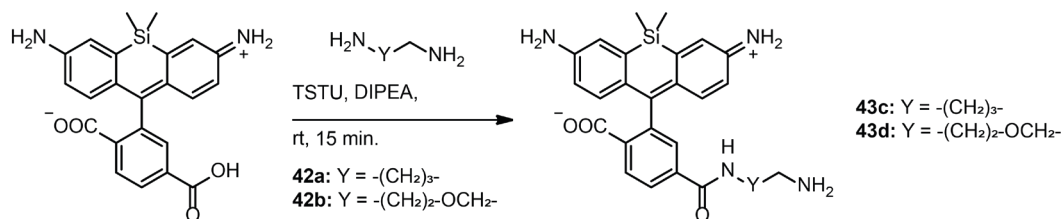
General procedure: A 2 mL vial was charged with SiR595-6'-COOH **14** (3 mg, 7.2 µmol, 1.0 eq) in DMSO (1 mL) and DIPEA (4.65 mg, 36 µmol, 5.0 eq.) and TSTU (2.4 mg, 7.9 µmol, 1.1) were added in one portion. Upon addition, the mixture turned from blue to colourless (DIPEA) to yellow (TSTU). After the mixture was stirred at rt for 5 min, diamine **42a** or **42b** (10 eq) was added and the reaction mixture was vigorously stirred for 15 min and then quenched with HOAc (25 eq) and 0.1% aqueous TFA (~100 µL per 3 mg of SiR595-6'-COOH). The crude was subjected to RP-HPLC (ACN/H₂O; gradient 10-90%) to obtain **43c** (51 %, 7.2 mM, 510 µL) and **43d** (44 %, 5.7 mM, 500 µL). The compounds were analysed by LC-MS and used for next reaction.

6.4.15 SiR650-Centrinone probes **44a** and **44b**

40b-c, EDC, HOBt, DIPEA

rt, 6 h

33b: R1 = Me; Y = -(CH₂)₂-OCH₂-

44a: Y = -(CH₂)₂-OCH₂-; X = N; n = 1
44b: Y = -(CH₂)₂-OCH₂-; X = N; n = 2

Compounds **40b** (1 mg, 1.5 µmol, 1 eq.) and **40c** (1 mg, 1.4 µmol, 1 eq.) were dissolved in DMSO dissolved in two 1.5 mL Eppendorf vials, and to each to Eppendorf were added DIPEA (2 mg (3 uL), 14.5 µmol, 10 eq.), EDC (0.25 mg, 1.6 µmol, 1.1 eq.), HOBt (0.25 mg, 0.3 µmol, 0.20 eq.) and **43b** (1.2 mg, 2.1 µmol, 1.5 eq.). Mixture was incubated for 6 h at room temperature. Reaction was followed by LC-MS and upon reaction completion, HOAc (~100 µL) and H2O (~100 µL) were added. The crude was subjected to RP-HPLC (ACN/H₂O; gradient 10-90%) to obtain **44a** (23 %, 3 mM, 100 µL) and **44b** (24 %, 3.3 mM, 100 µL) as blue powder that was dissolved in DMSO. The compounds were analysed by LC-MS, and unfortunately due to limited amount compound no further characterization was performed

6.4.16 SiR595-Centrinone probes **44c and 44d**

40b-c EDC, HOBt, DIPEA

rt, 6 h

43c: Y = -(CH₂)₂-OCH₂-

44a: Y = -(CH₂)₂-OCH₂-; n = 1
44b: Y = -(CH₂)₂-OCH₂-; n = 2
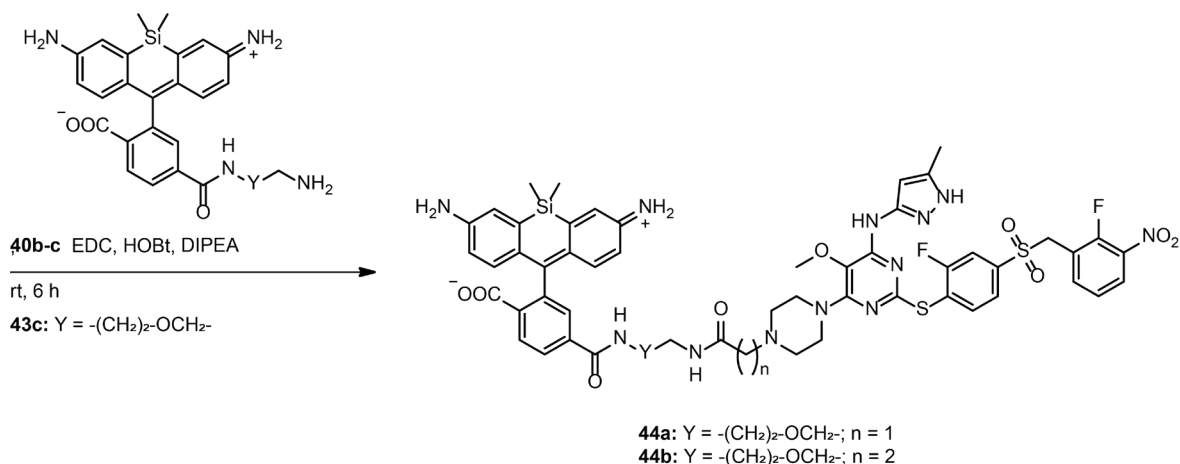
Compounds **40b** (1 mg, 1.5 µmol, 1 eq.), **40c** (1 mg, 1.4 µmol, 1 eq.) were dissolved in DMSO were dissolved in DMSO dissolved in two 1.5 mL Eppendorf vials, and to each to Eppendorf were added PEA (2 mg (3 uL), 14.5 µmol, 10 eq.), EDC (0.25 mg, 1.6 µmol, 1.1 eq.), HOBt (0.25 mg, 0.3 µmol, 0.20 eq.) and **43c** (1.2 mg, 2.1 µmol, 1.5 eq.). Mixture was incubated for 6 h at room temperature. Reaction was followed by LC-MS and upon reaction completion, HOAc (~100 µL) and H2O (~100 µL) were added. The crude was subjected to RP-HPLC (ACN/H₂O; gradient 10-90%) to obtain **44c** (29 %, 3.3 mM, 100 µL) and **44d** (35 %, 5.1 mM, 100 µL) as

blue powder that was dissolved in DMSO. The compounds were analysed by LC-MS, and unfortunately due to limited amount compound no further characterization was performed

6.4.17 SiR595-Centrinone probes **44e and 44f**

44e: Y = -(CH₂)₂-OCH₂-
44f: Y = -(CH₂)₃-
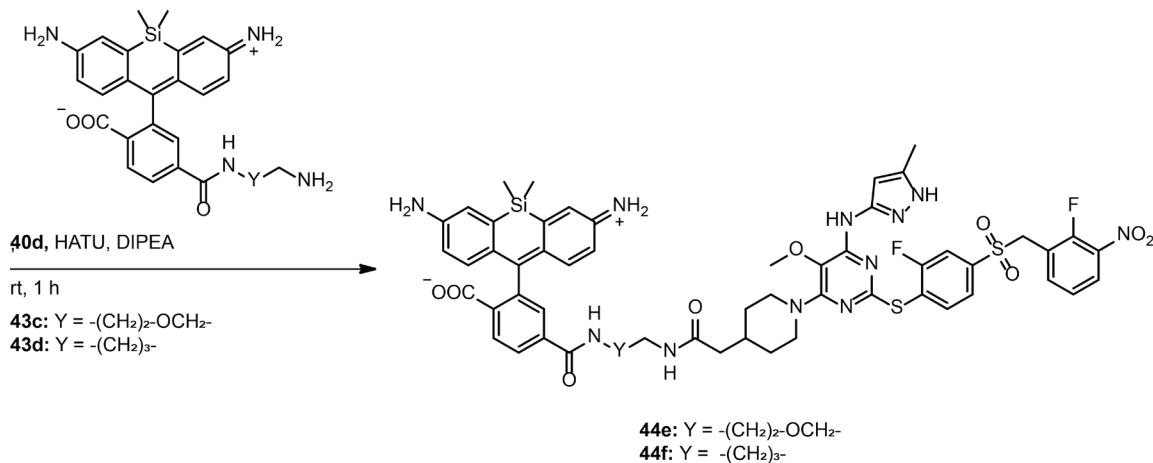
Two 1.5 mL Eppendorf vials were charged with compound **40d** (1 mg, 1.45 µmol, 1 eq.) and dissolved in DMSO, followed by addition of DIPEA (2 mg (~3 uL), 14.5 µmol, 10 eq.) and HATU (0.6 mg, 1.6 µmol, 1.1 eq.). The acid was activated for 15 min. upon which **43c** (1.1 mg, 2.2 µmol, 1.5 eq.) or **43d** (1.1 mg, 2.1 µmol, 1.5 eq) were added. Mixture was incubated for 1 h at room temperature. Reaction was followed by LC-MS and upon reaction completion, HOAc (~100 µL) and H_2O (~100 µL) were added. The crude was subjected to RP-HPLC (ACN/H_2O; gradient 10-90%) to obtain **44e** (40 %, 5.8 mM, 100 µL) and **44f** (44 %, 6.4 mM, 100 µL) as blue powder that was dissolved in DMSO. The compounds were analysed by LC-MS, and unfortunately due to low amounts of compound only limited characterization was performed

44e:

HRMS (ESI): calc. for $C_{56}H_{57}F_2N_{11}O_{10}S_2Si$ [M+H]$^+$: 587.6807; found 587.6804.

44f:

HRMS (ESI): calc. for $C_{56}H_{57}F_2N_{11}O_9S_2Si$ [M+2H]$^+$: 579.6833; found 579.6827.

7 Appendix

7.1 Rat hippocampal neurons labeled with SiR595-Actin
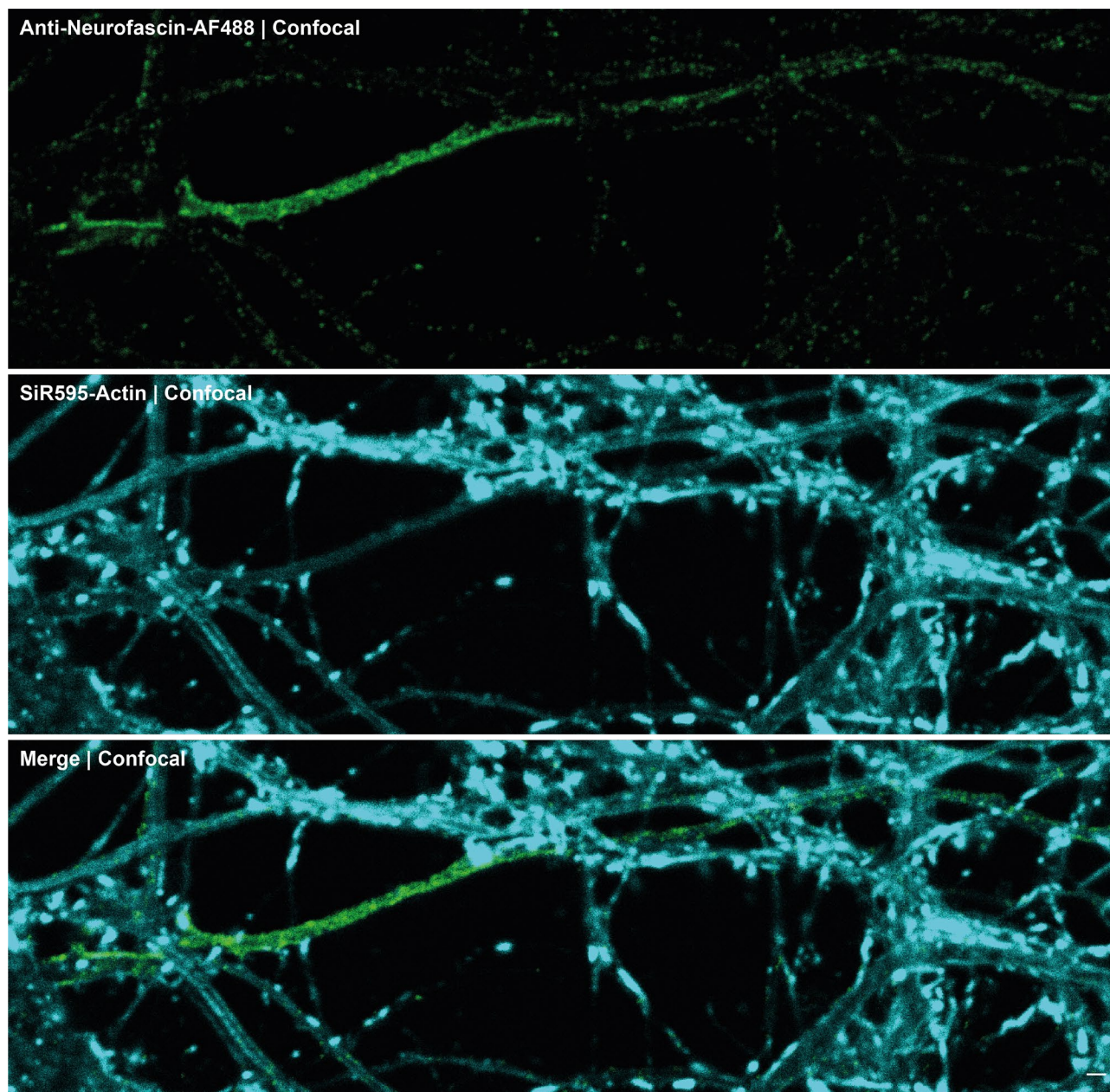
Figure 18. Live confocal imaging of rat hippocampal neurons cultured for 22 days, and labelled with nanobody with Alexa-488 labelling neurofascin (15 min.) as axonal marker (see Appendix 7.2) and incubated with SIR595-Actin (1 µM). Scale bar: 2 µm.

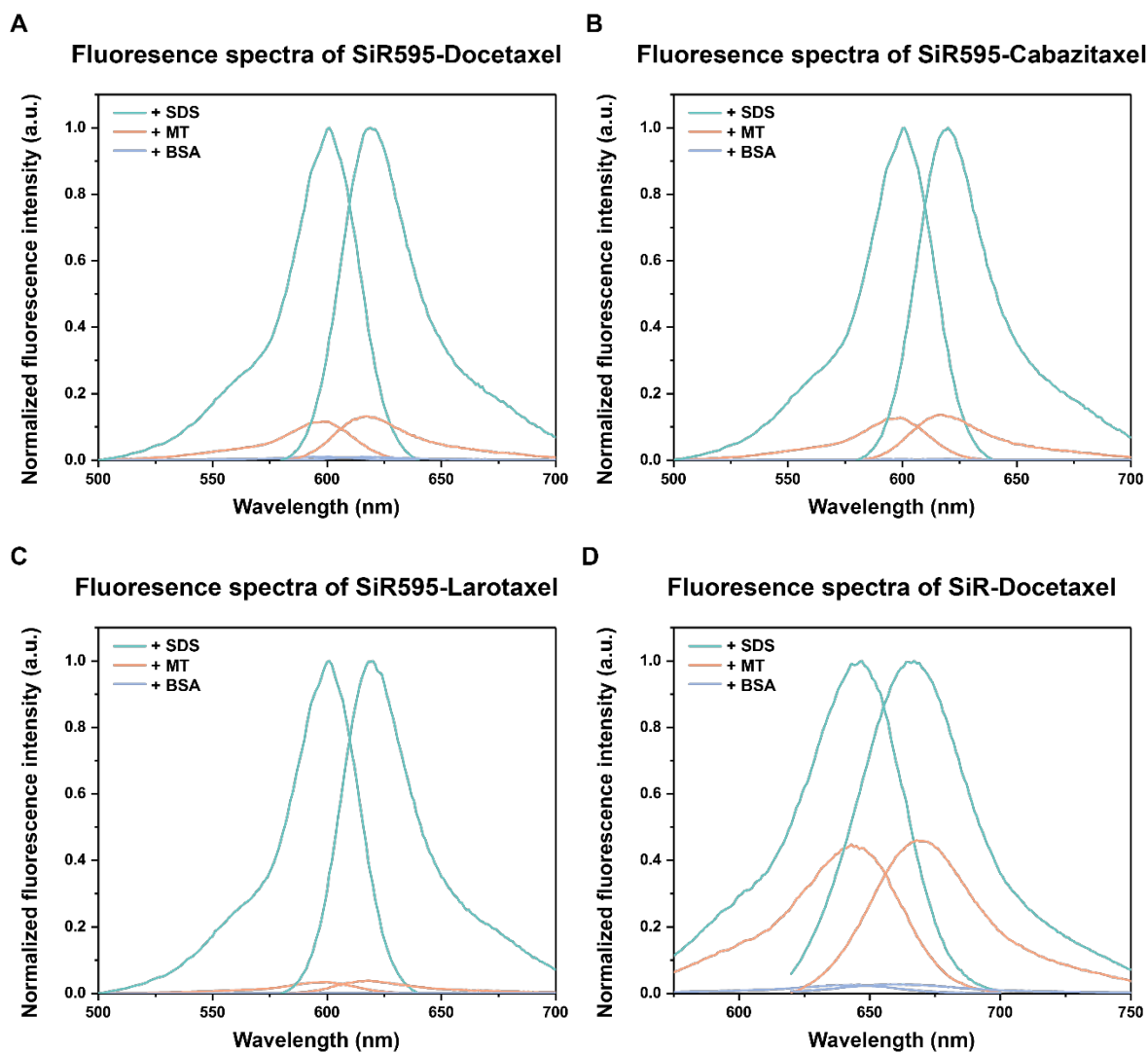## 7.2 Fluorescence spectra of SiR650-Tubulin and SiR595-Tubulin probes

A

B

C

D

Figure 19. Fluorescence excitation and emission spectra of different SiR650-Tubuli and SiR595-Tubulin probes.

7.3 Fluorescence spectra of SiR595-5'/6'-DNA and SiR-6'-DNA

A

B

C
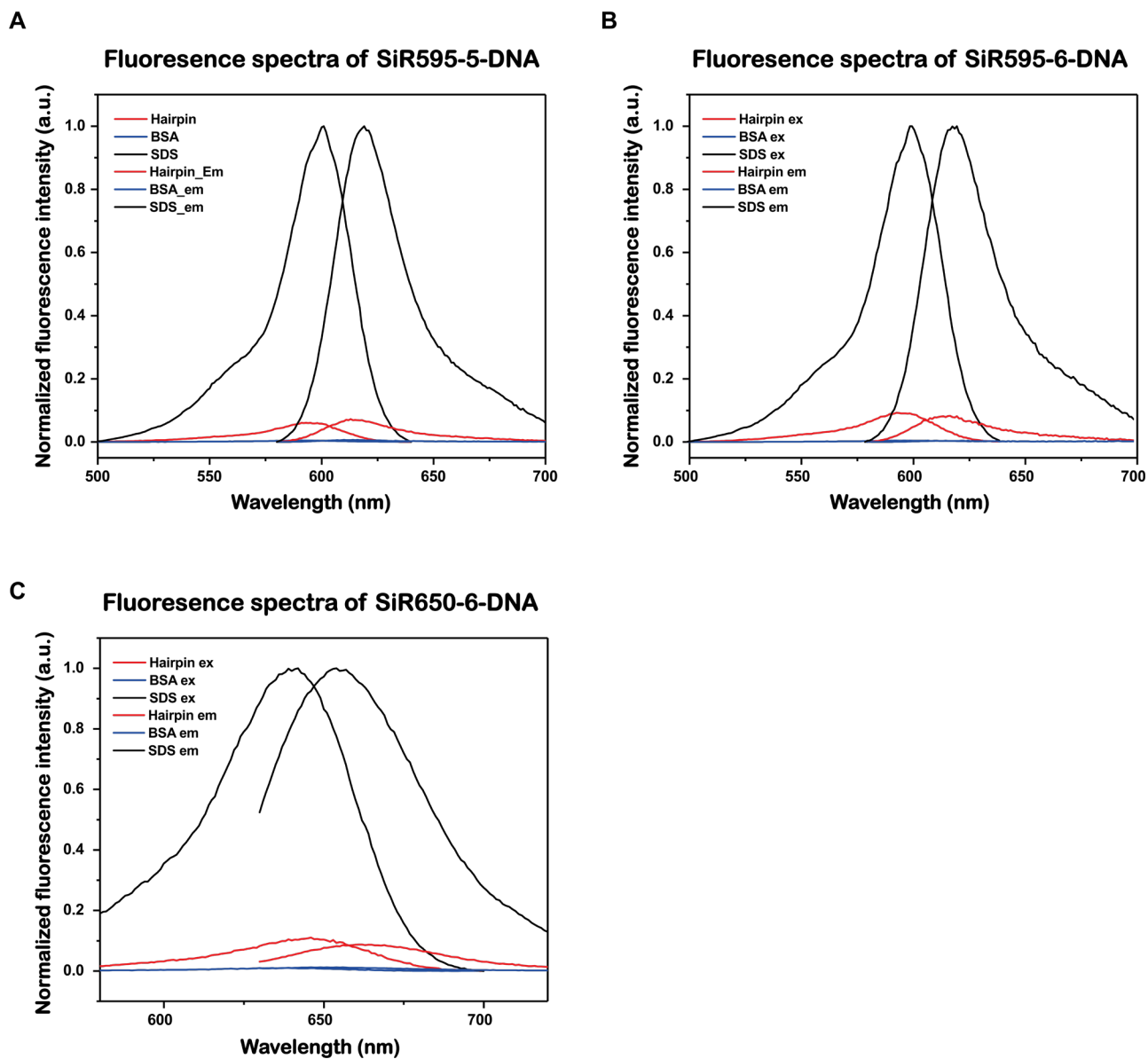
Figure 20. Fluorescence excitation and emission spectra of SiR650-6'-DNA and SiR595-5/6-DNA probes

7.4 Plk4 purification and characterization

A   Coomassie stain of His-tag purified Plk4-KD
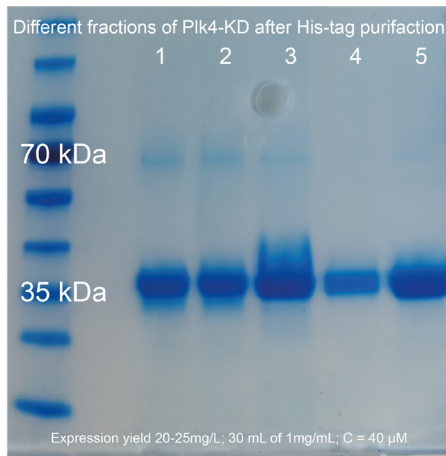
B   Coomassie stain of purified Plk4-KD

35 kDa
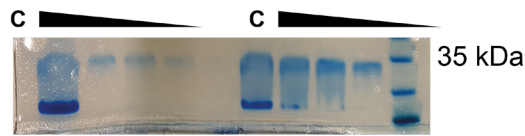
C   Western blot of purified Plk4-KD

rabbit anti-His &
anti-rabbit- Alexa680

mouse anti-Plk4-KD &
anti-mouse- Dylight 800
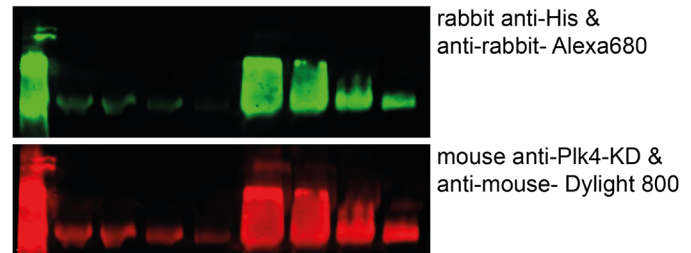
D   **High resolution mass of Plk4-KD**
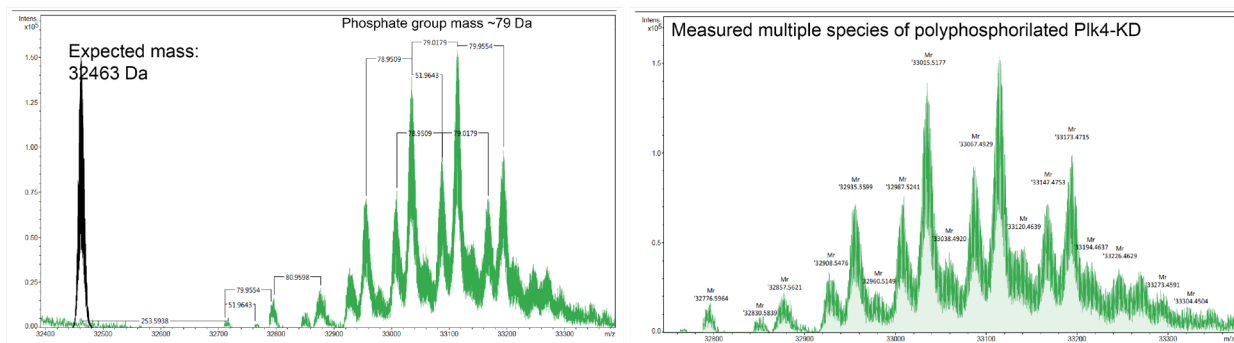
E   **ETD measurements of Plk4-KD**
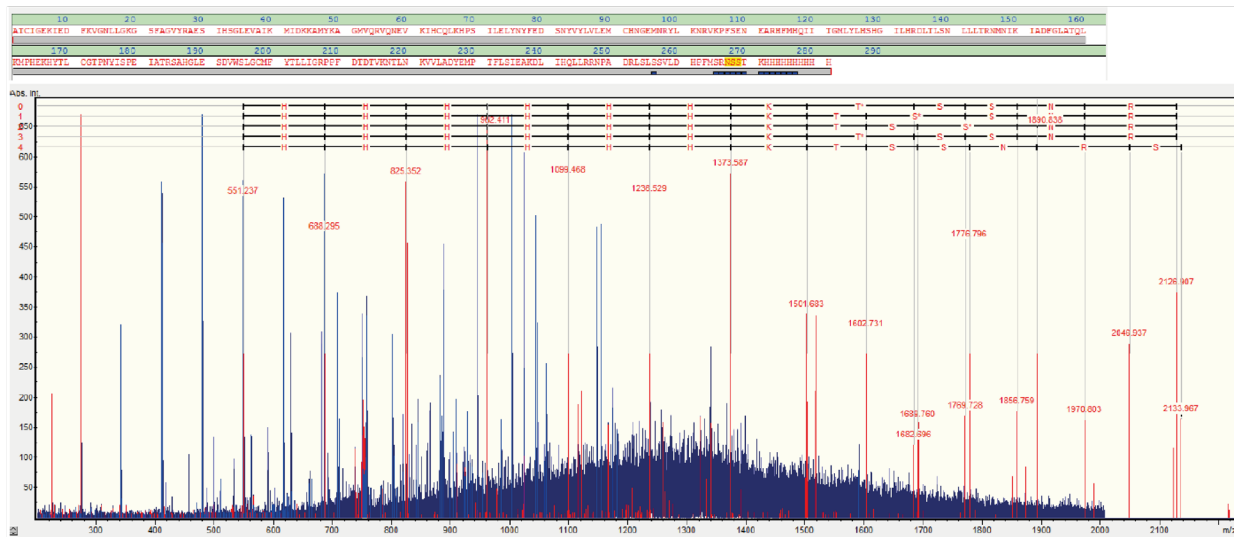
Figure 21. A. Coomassie stain of Plk4-KD-6xHis protein after His-tag purification **B.** Coomassie stain of purified and concentrated Plk4-KD-6xHis at decreasing concentrations prior to Western-blot. **C.** Western blot of decreasing amounts of Plk4-KD-6xHis protein stained with different antibodies **up:** Primary antibody: rabbit anti-His; Secondary antibody: Anti-rabbit Alexa680; **down**: Primary antibody: mouse anti-Plk4 kinase domain; Secondary antibody: Anti-mouse Dyligth 800. **D.** High resolution mass of purified Plk4-KD-6xHis showing different species of polyphosphorylated Plk4-KD-6xHis.**E.** Electron-transfer dissociation analysis of C-terminus of Plk4-KD-6xHis protein showing expected sequence.

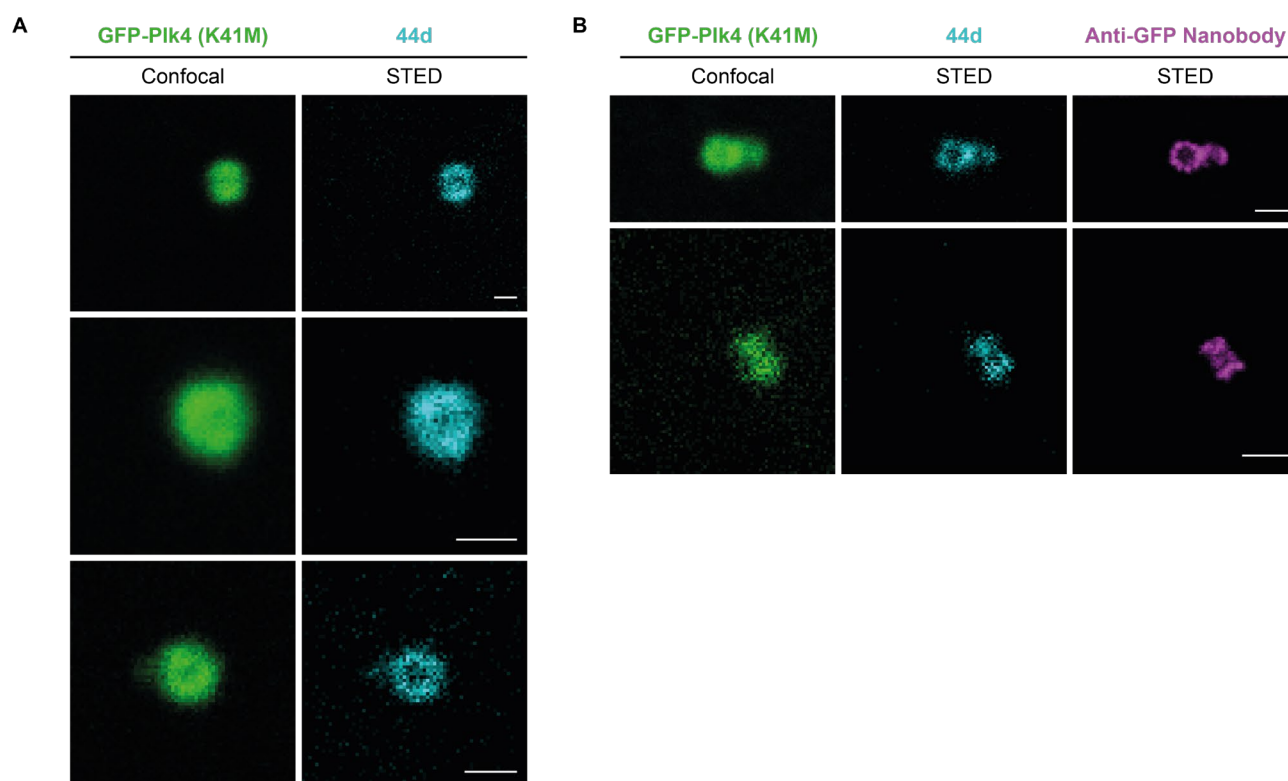## 7.5 Hela cells expressing GFP-Plk4(K41M) labeled with 44d

Figure 22. . **A**. Live-cell STED images of centrioles obtained by imaging Hela cells overexpressing GFP-PLK4 (K41M) labelled for 1h by **44d** (500nM); Scale bar: 500 nm **B.** Upon live-cell STED imaging cells were fixed with MeOH (-20 °C) and labelled with anti-GFP nanobody. Upon nanobody labelling cells were imagined on STED microscope showing that signal of **44d** is colocalized with anti-GFP antibody. Scale bar: 500 nm.

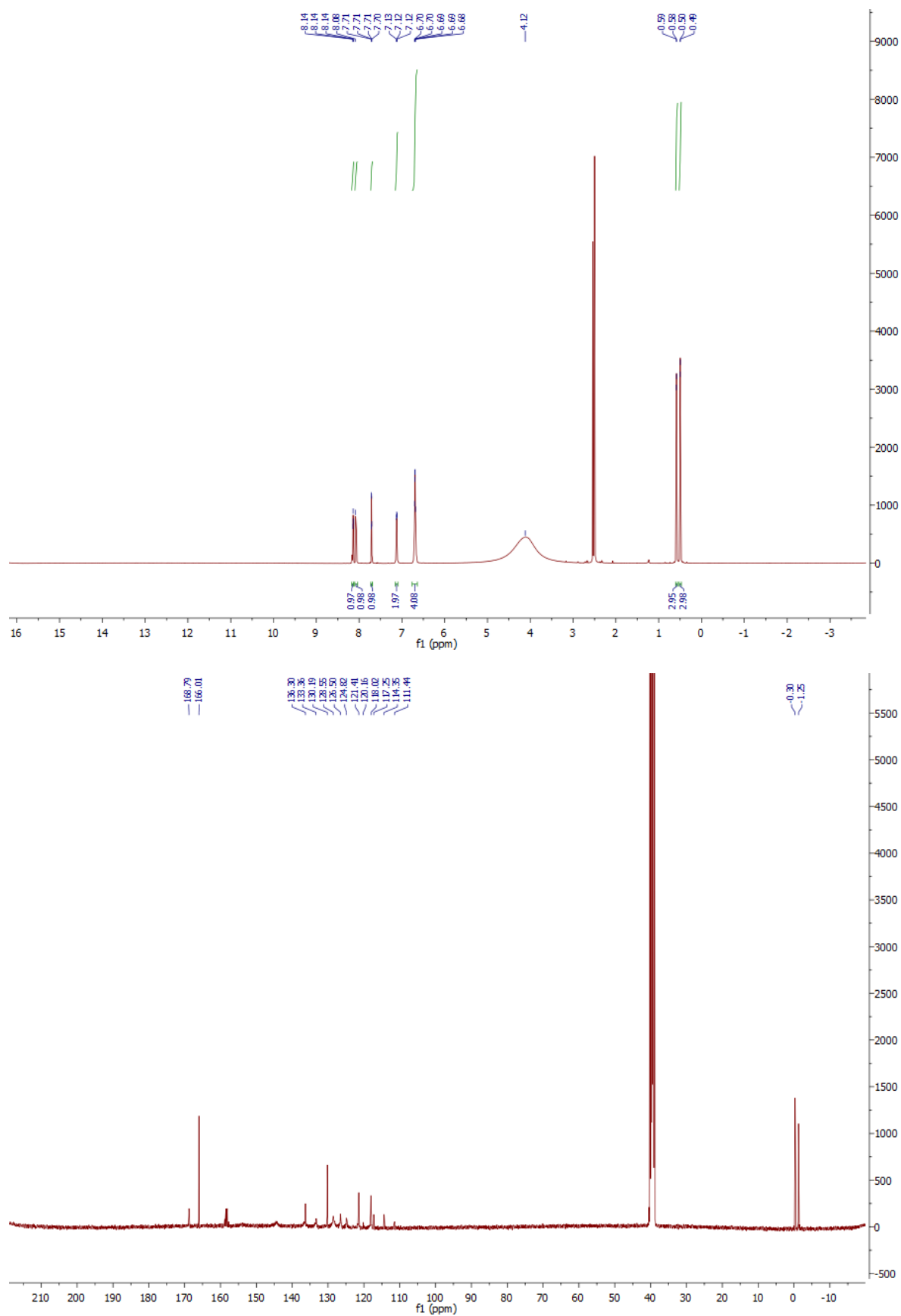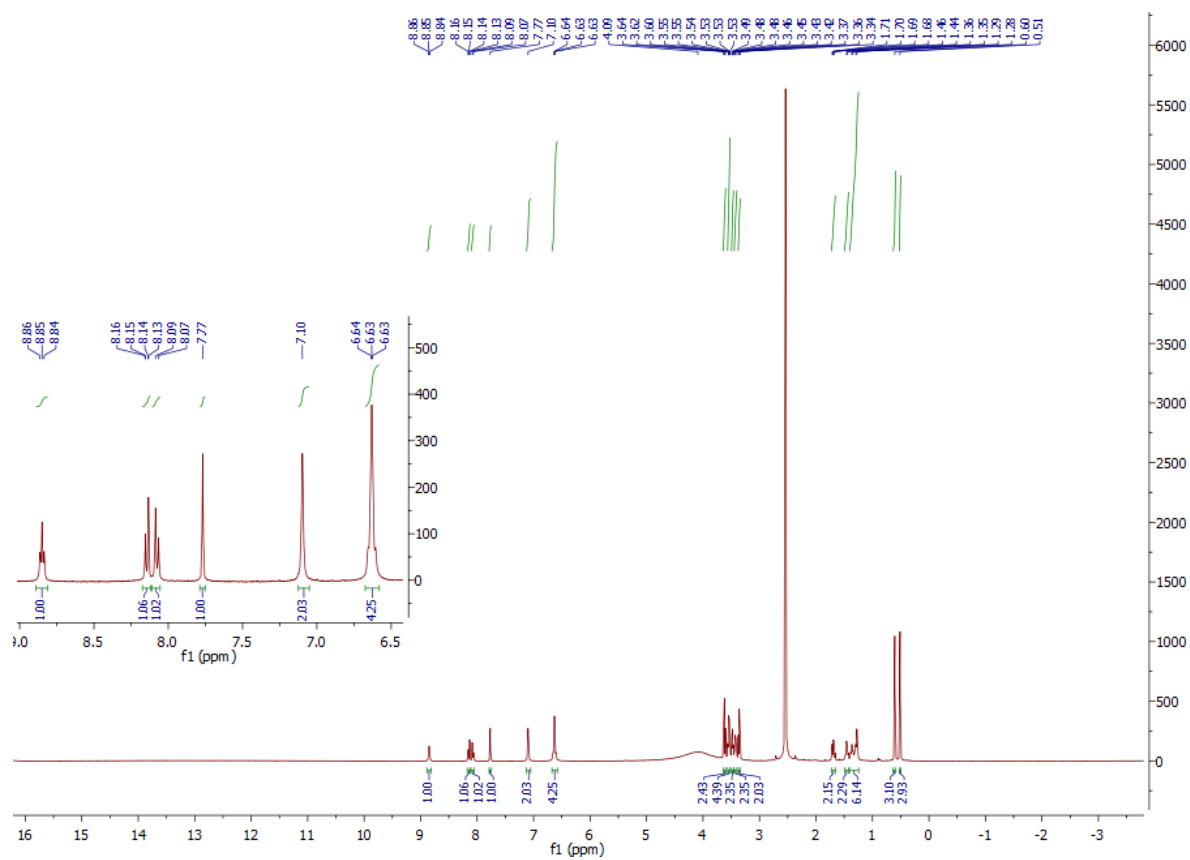## 7.6 Hela cells overexpressing GFP-Plk4(K41M) labeled with 44f
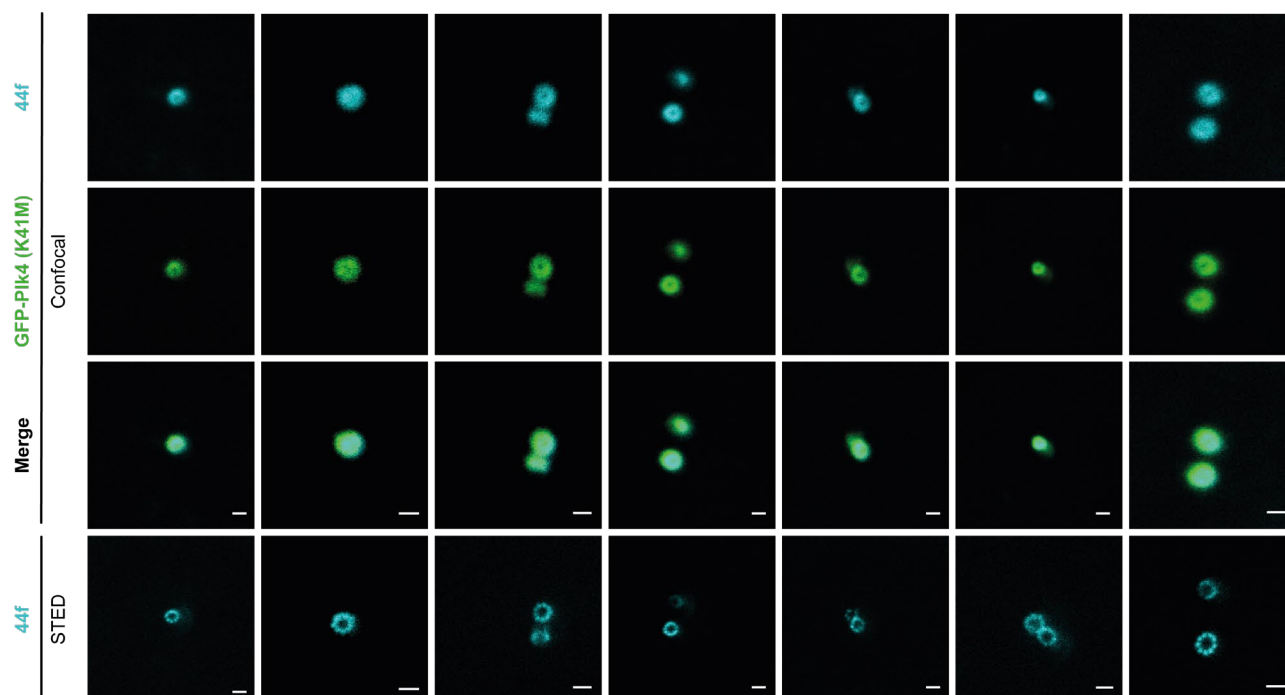
Figure 23. Full set of images acquired from live-cell imaging of HeLa cells overexpressing GPF-Plk4(K41M) labelled with **44f**
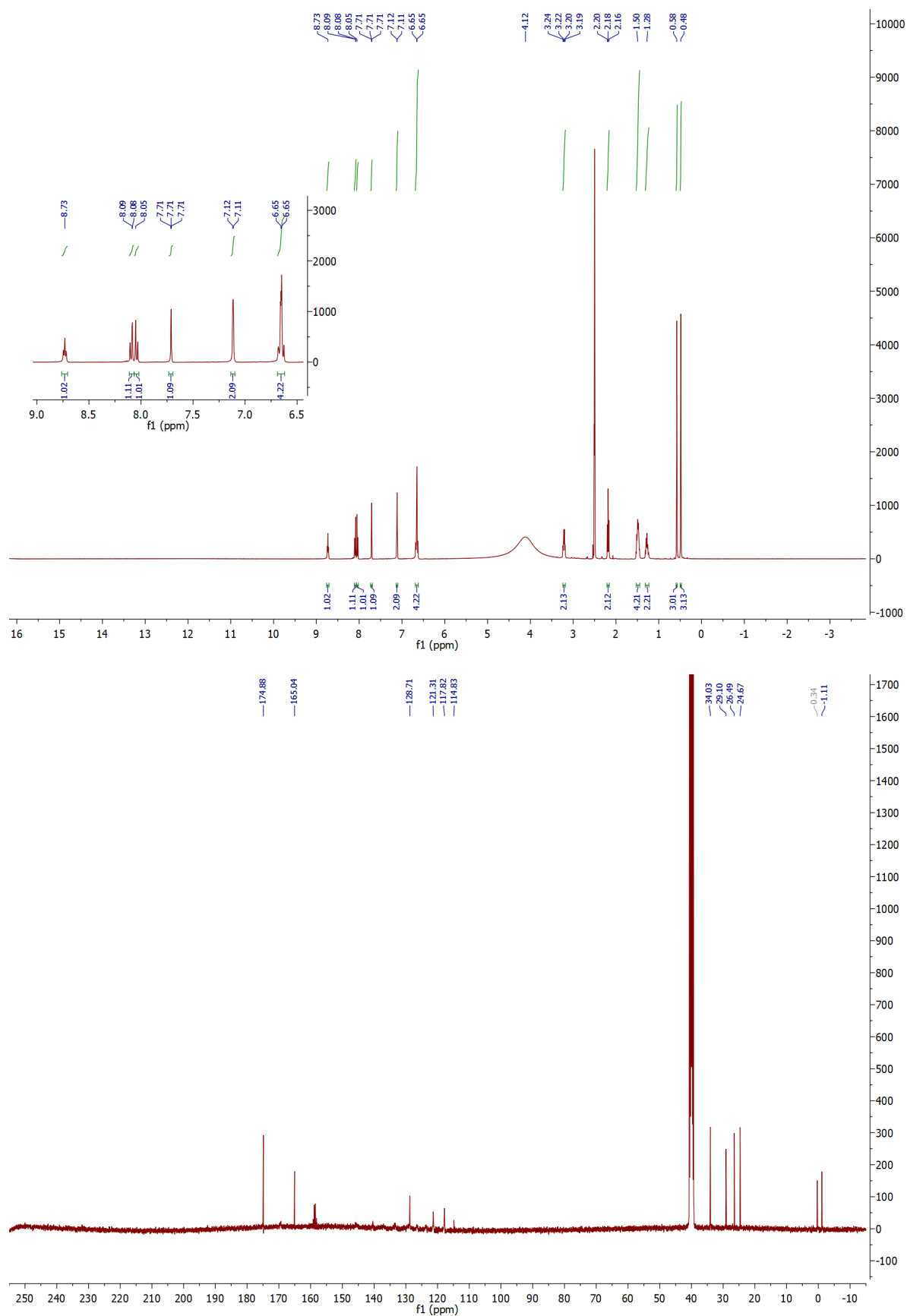
7.7 NMR Spectra

7.7.1 Compound **13**
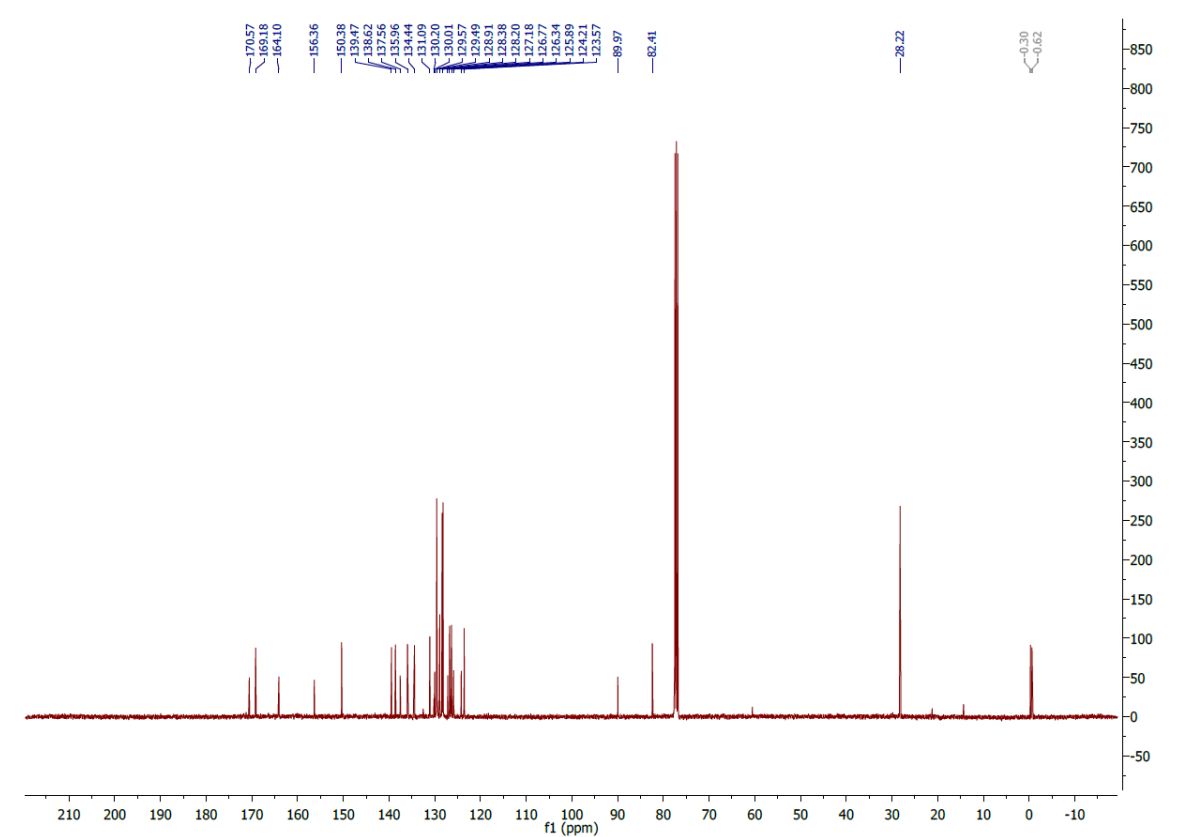
7.7.2 Silicon-Rhodamine 595 (SiR595-6'-COOH) **14**

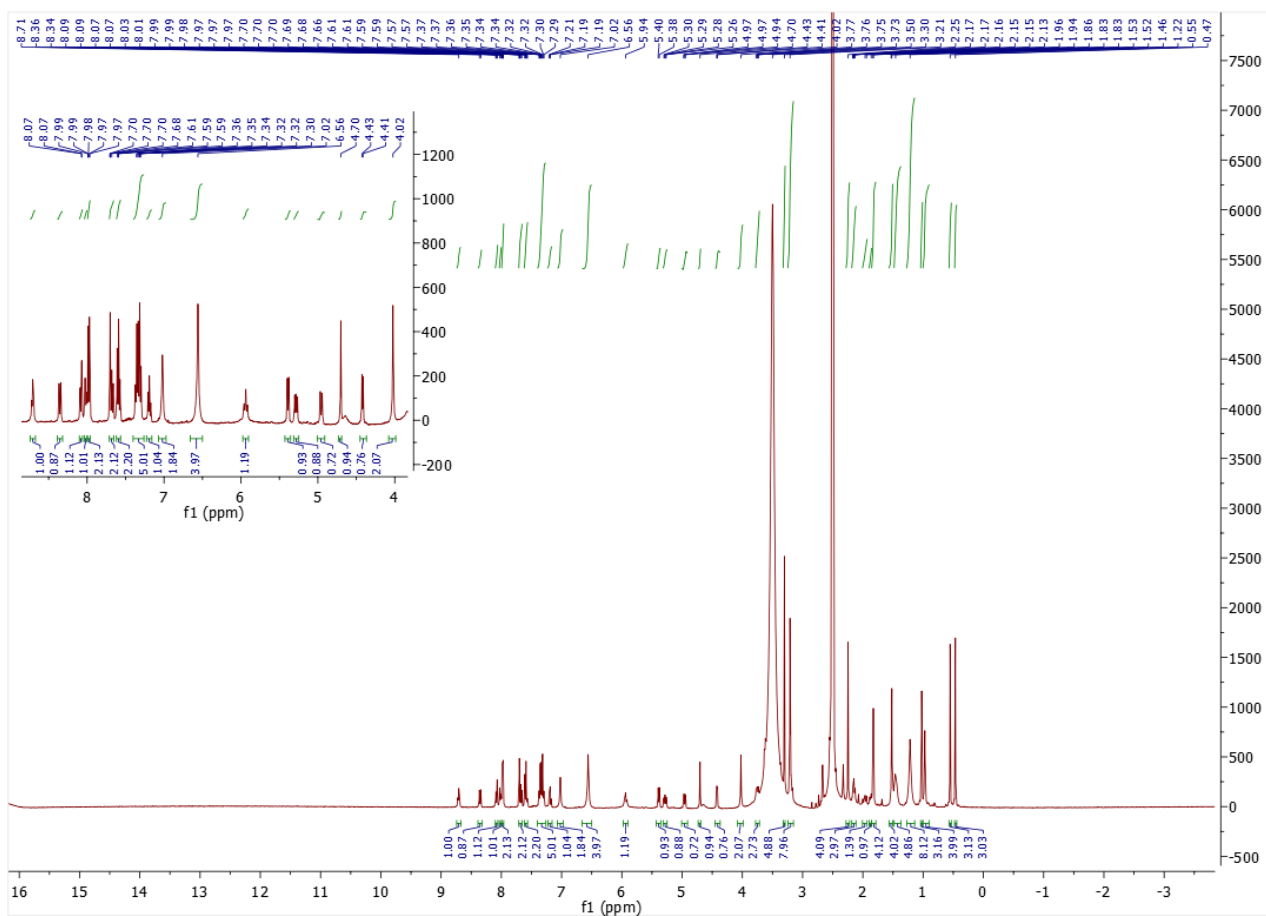### 7.7.3 SiR595-Halo **16**

7.7.4   SiR595-C5-COOH **17**
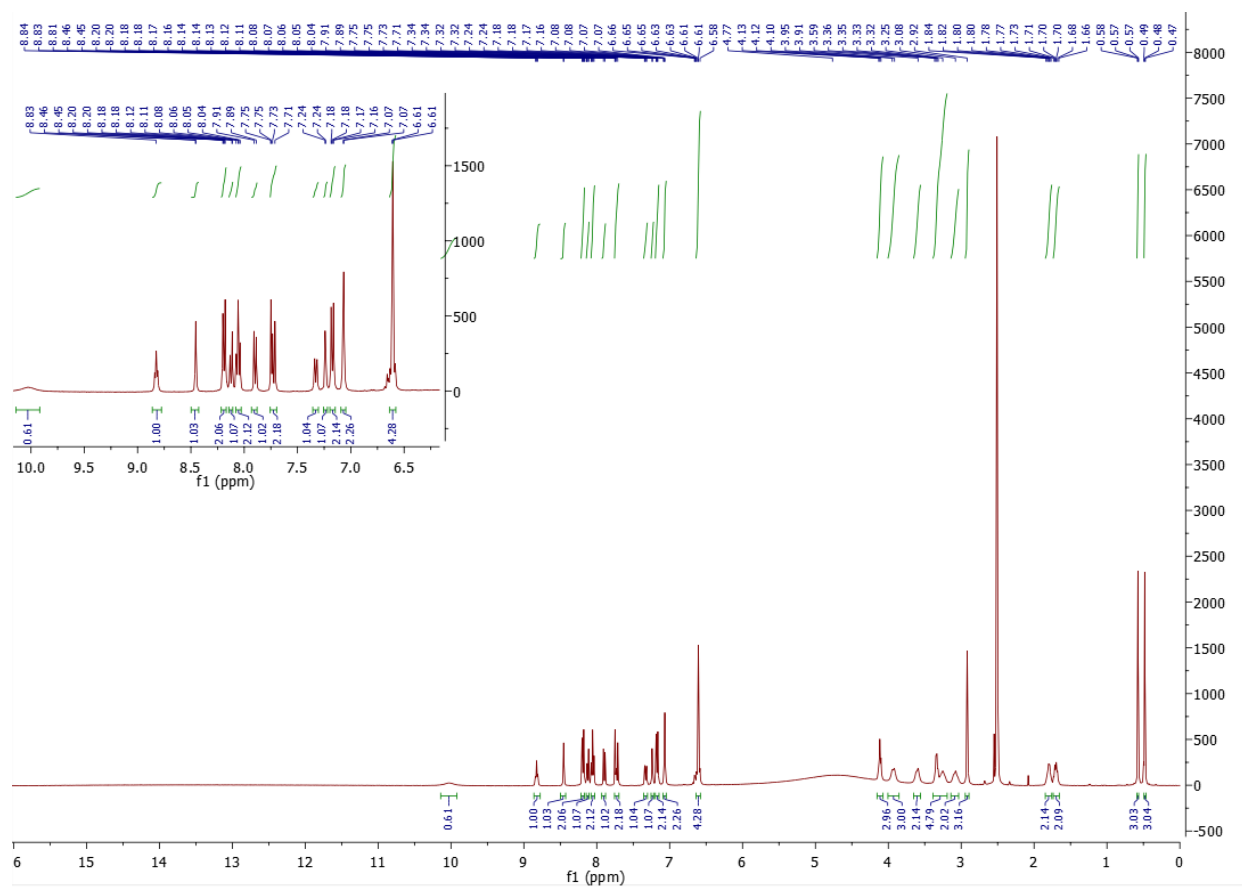
7.7.5   SiR595-Actin **19**
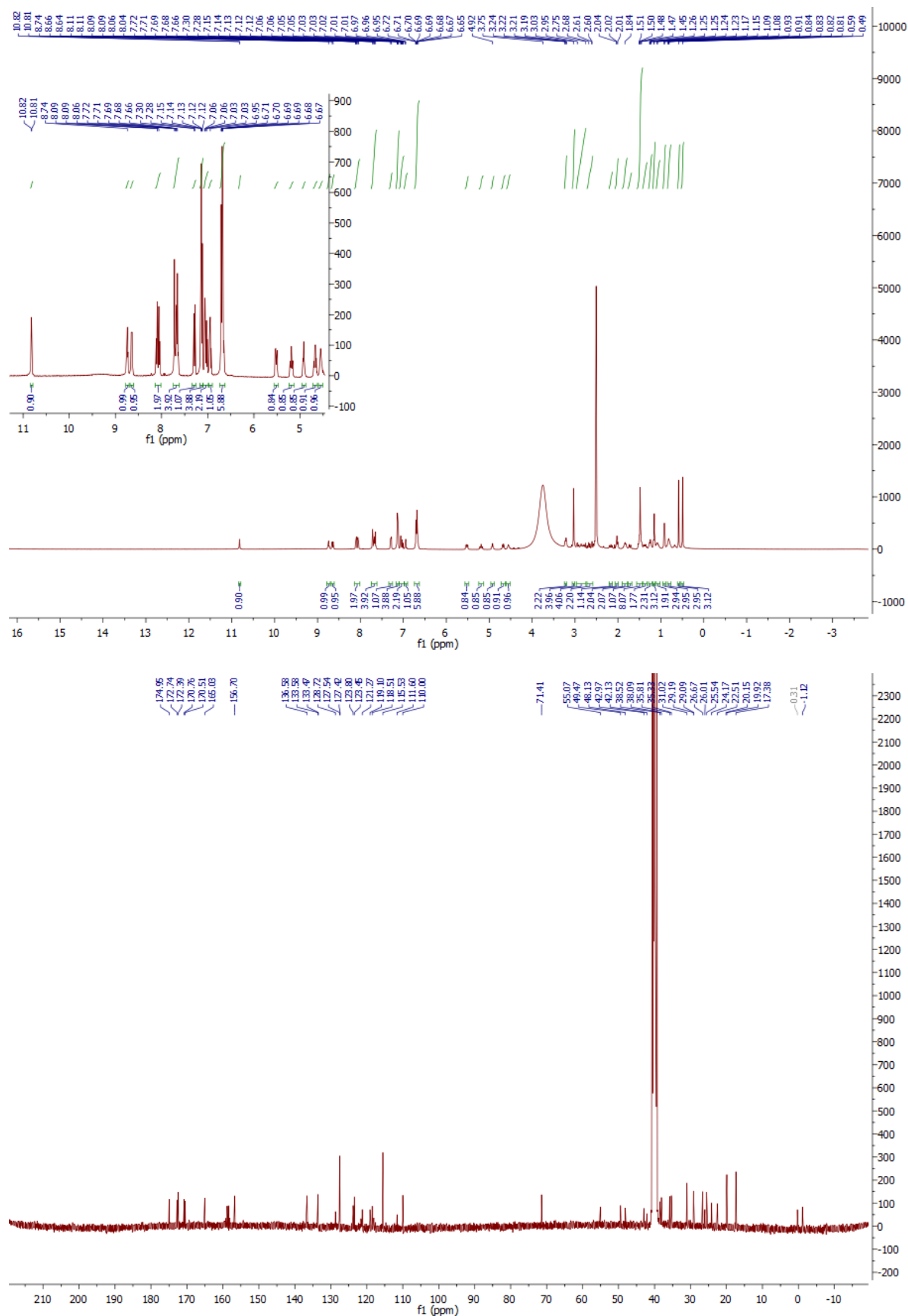
7.7.6   SiR595-C7-COOH **20**
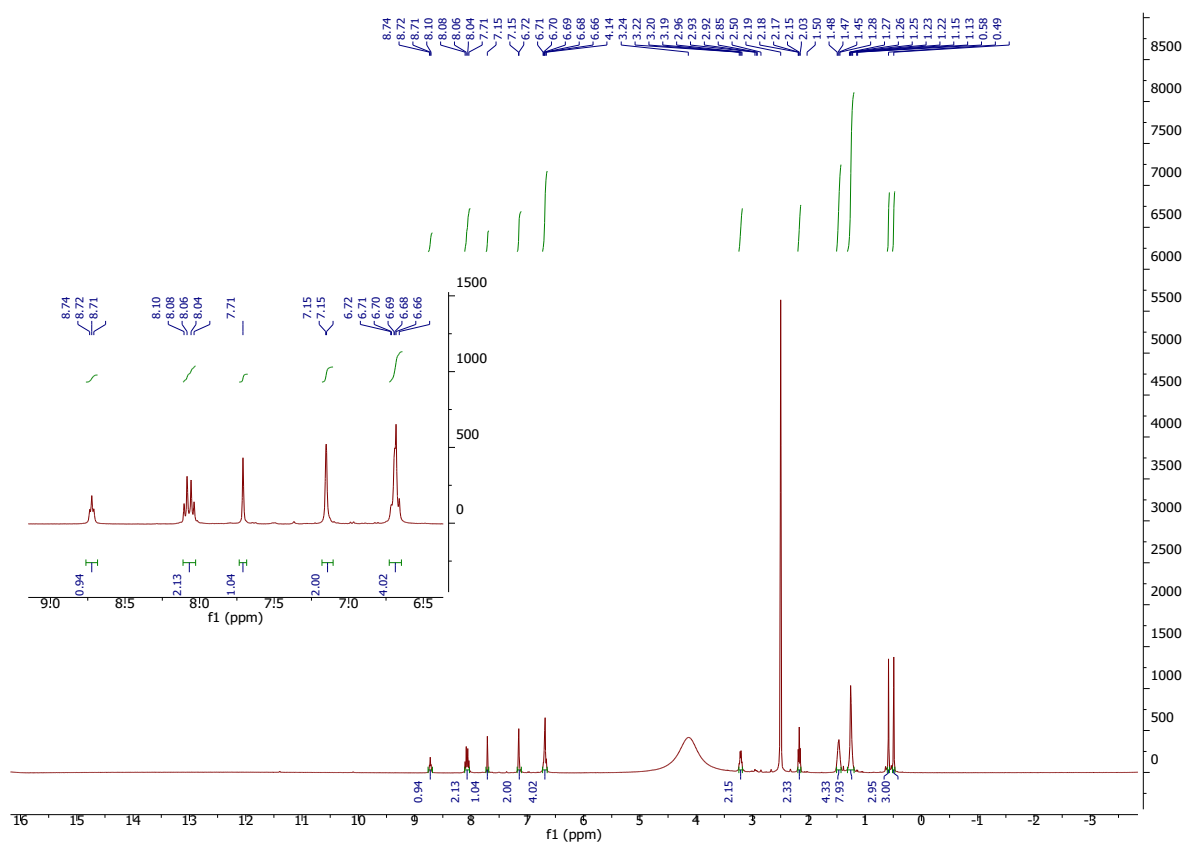
7.7.7 SiR595-Cabazitaxel **22b**

7.7.8 SiR595-6'-DNA **24b**

7.7.9 4,6-Dihydroxy-5-methoxy thiopyrimidine **27**
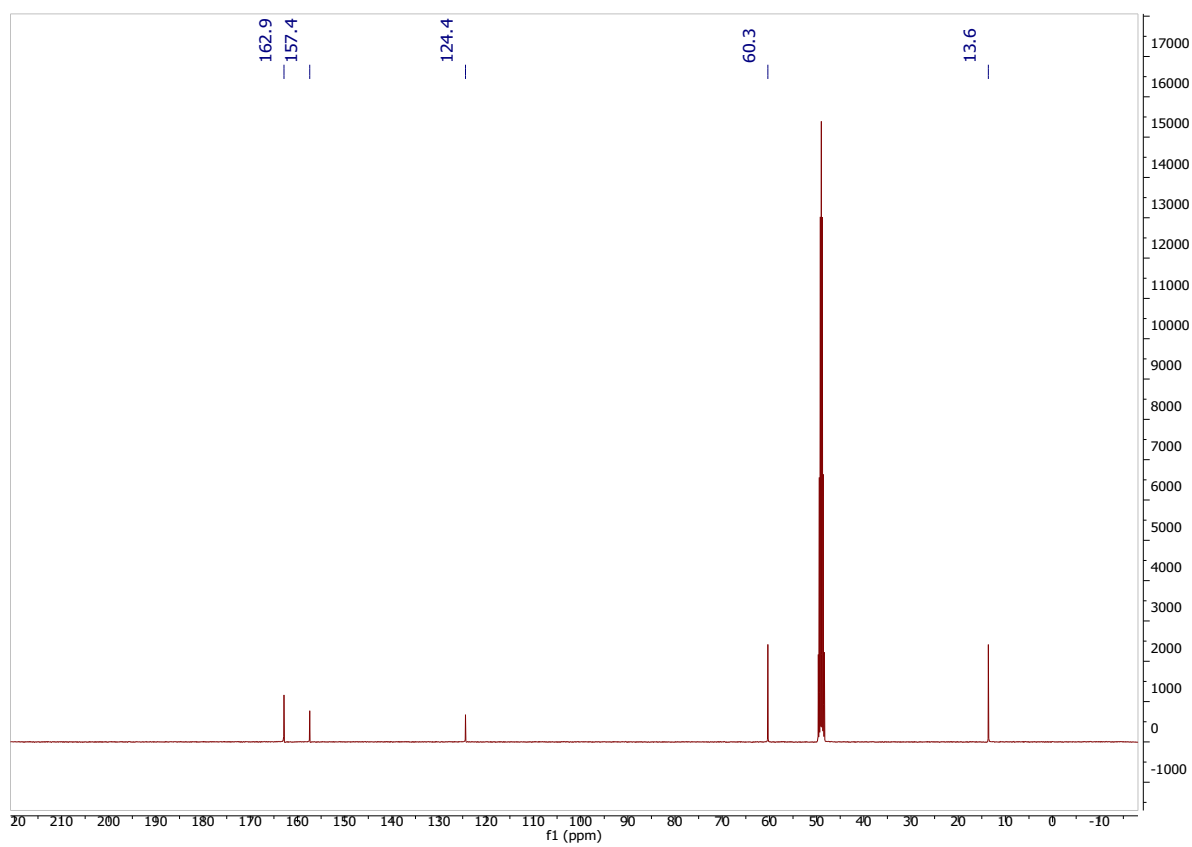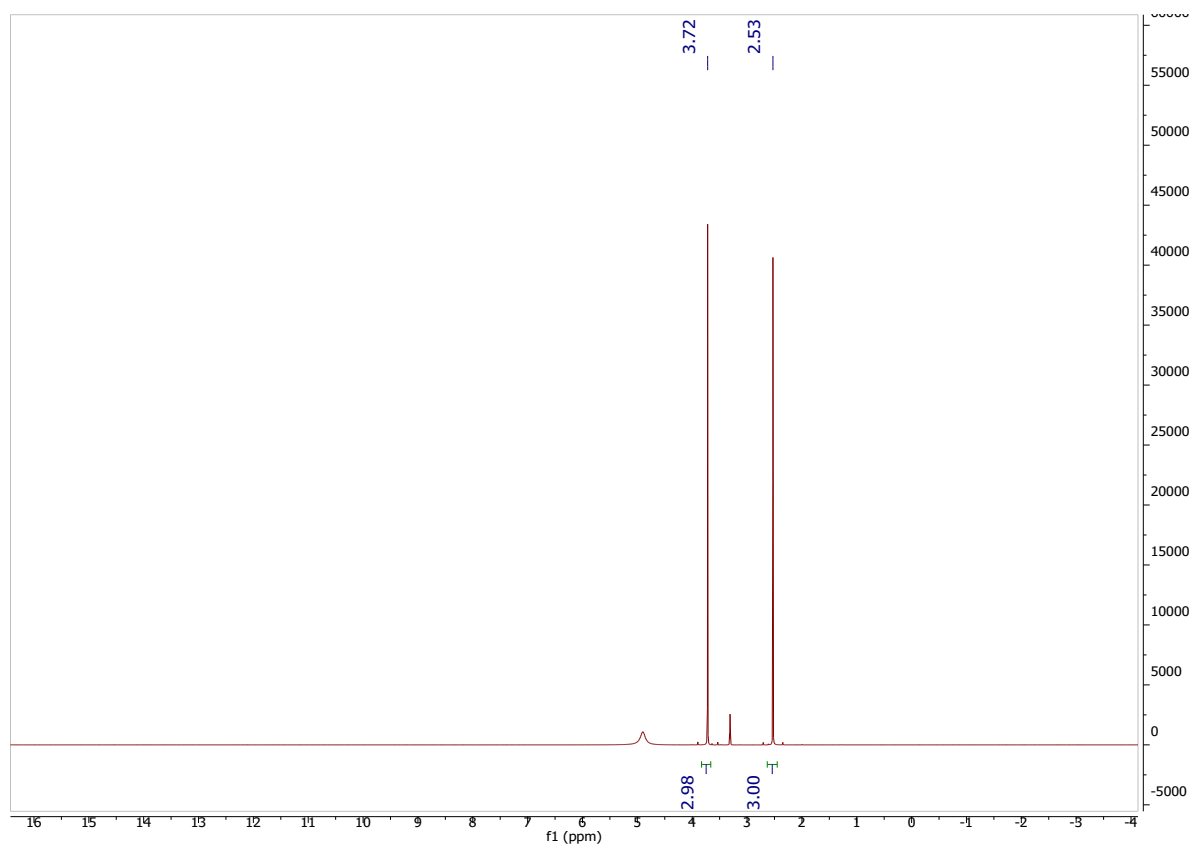
7.7.10 6-Chloro-5-methoxy-4-((methyl-*1H*-pyrazol-3-yl)amino)-2-(methylthio) pyrimidine **28**
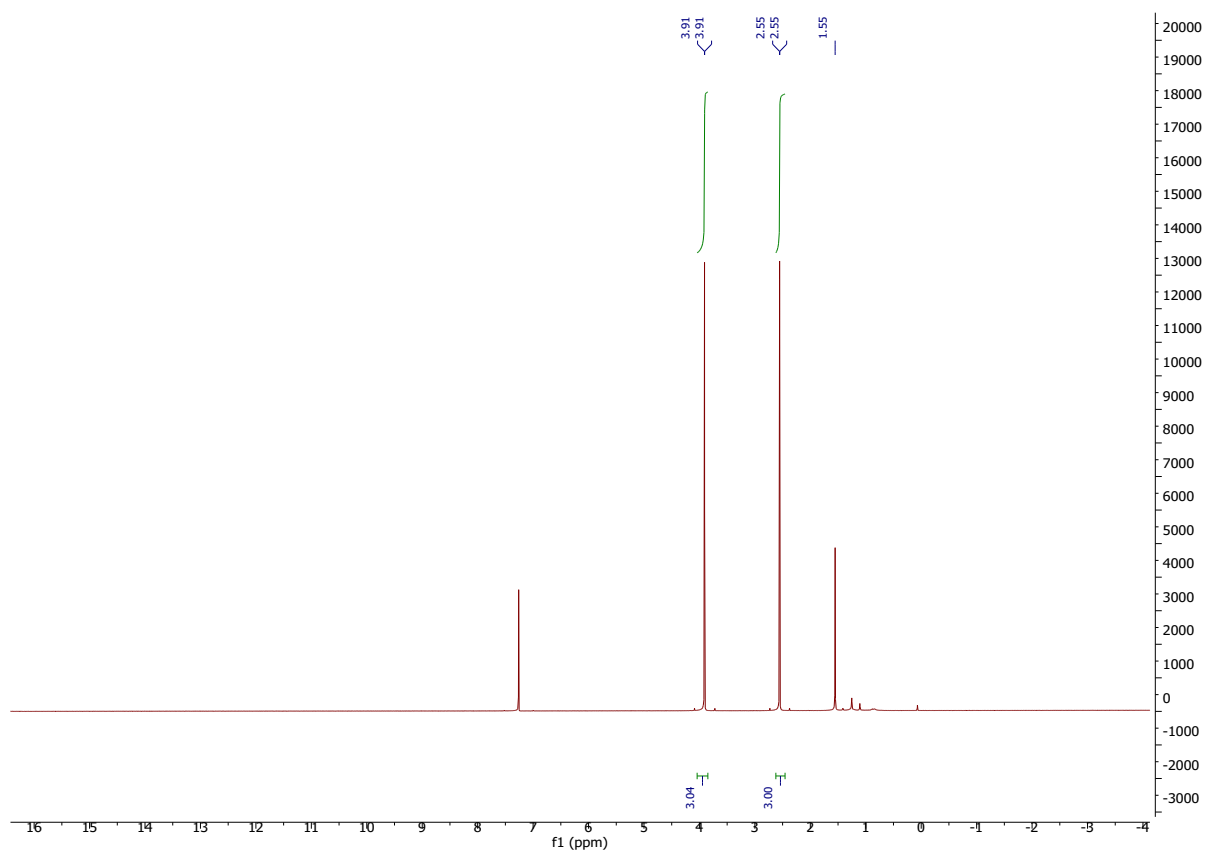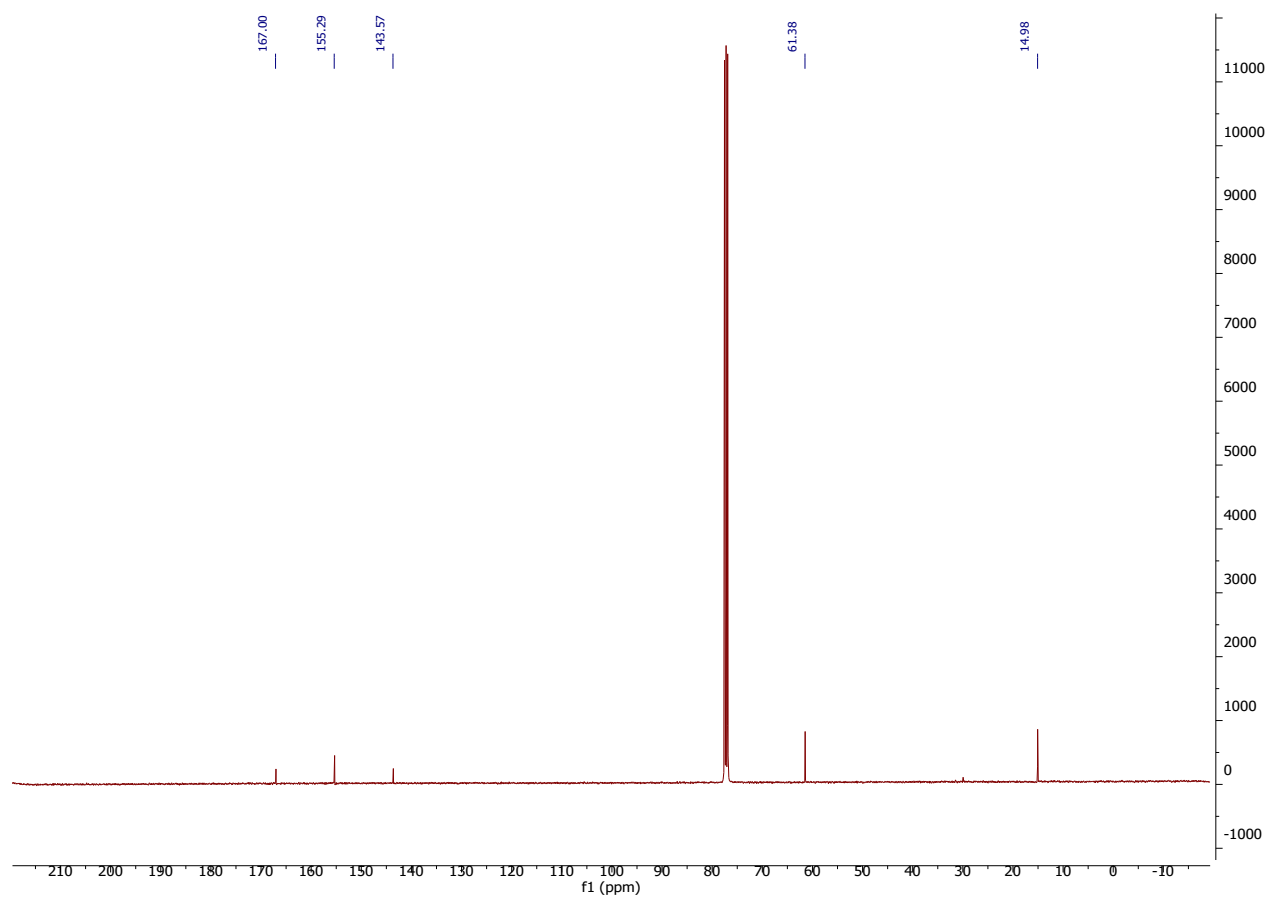
7.7.11 6-chloro-5-methoxy-4-((5-methyl-1H-pyrazol-3-yl)amino)-2-(methylsulfonyl) pyrimidine **30**
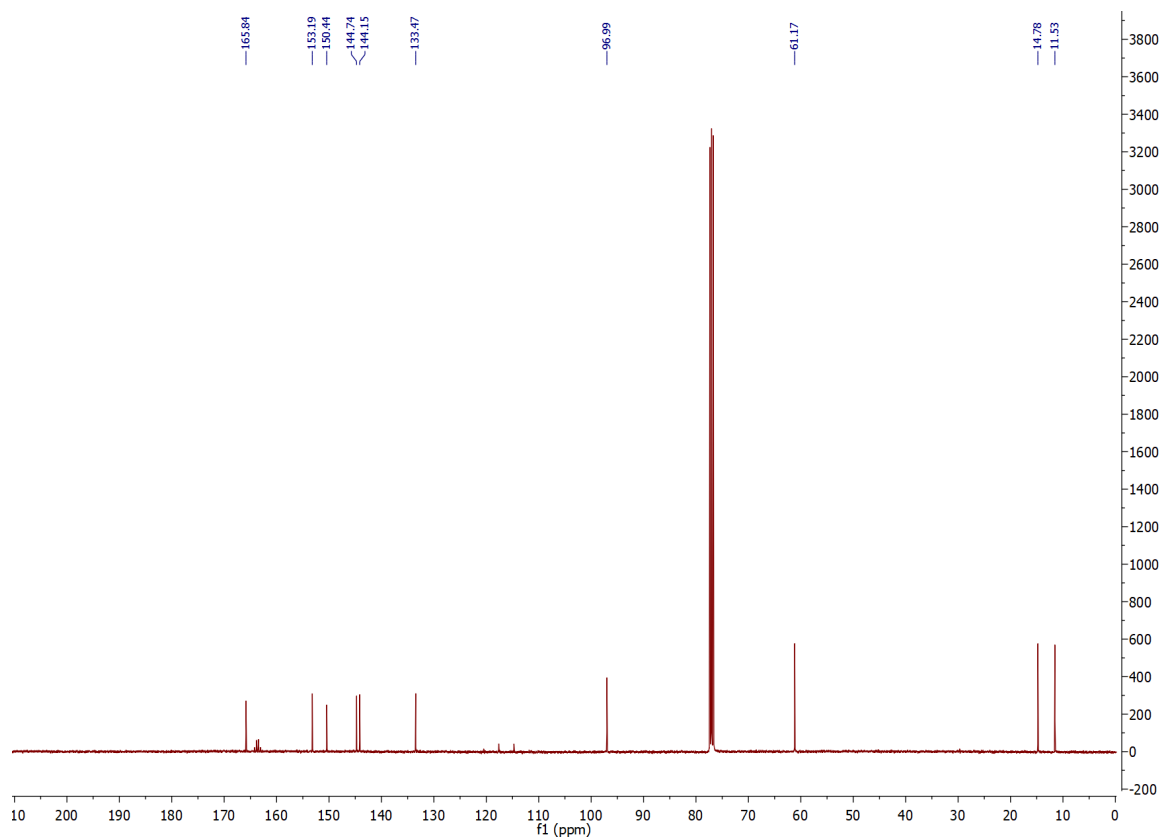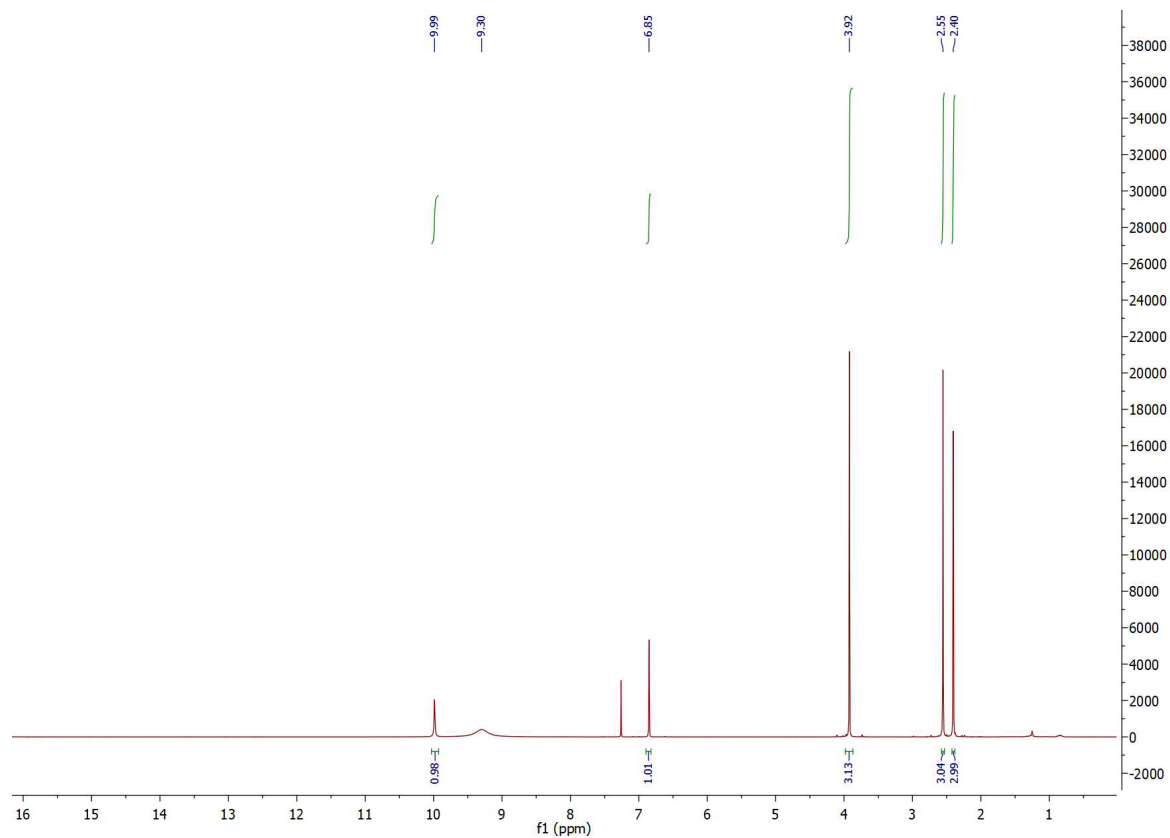
7.7.12 6-chloro-5-methoxy-4-((5-methyl-1H-pyrazol-3-yl)amino)-2-(methylsulfonyl) pyrimidine **31**
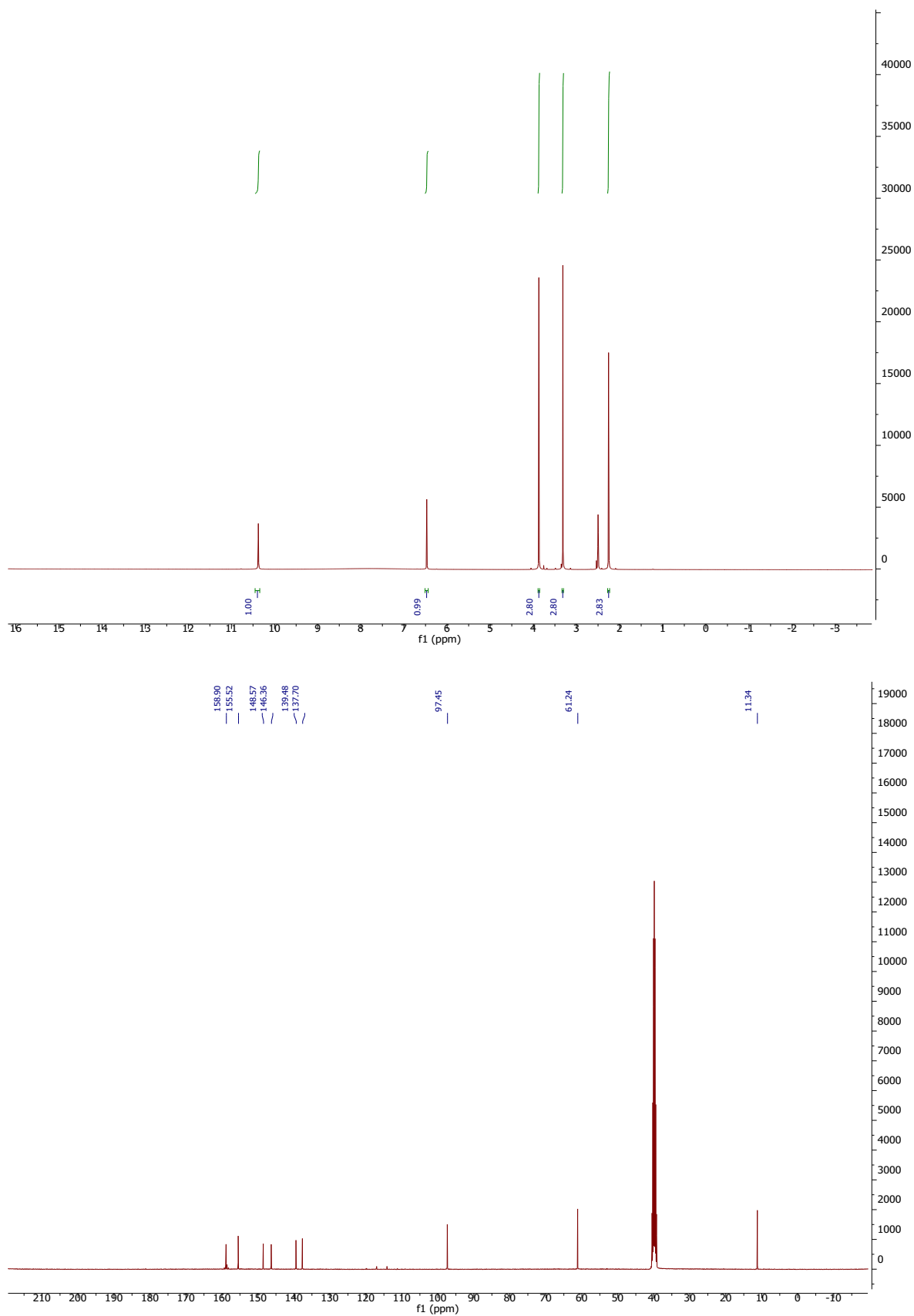
7.7.13 1-(bromomethyl)-2-fluoro-3-nitrobenzene **33**
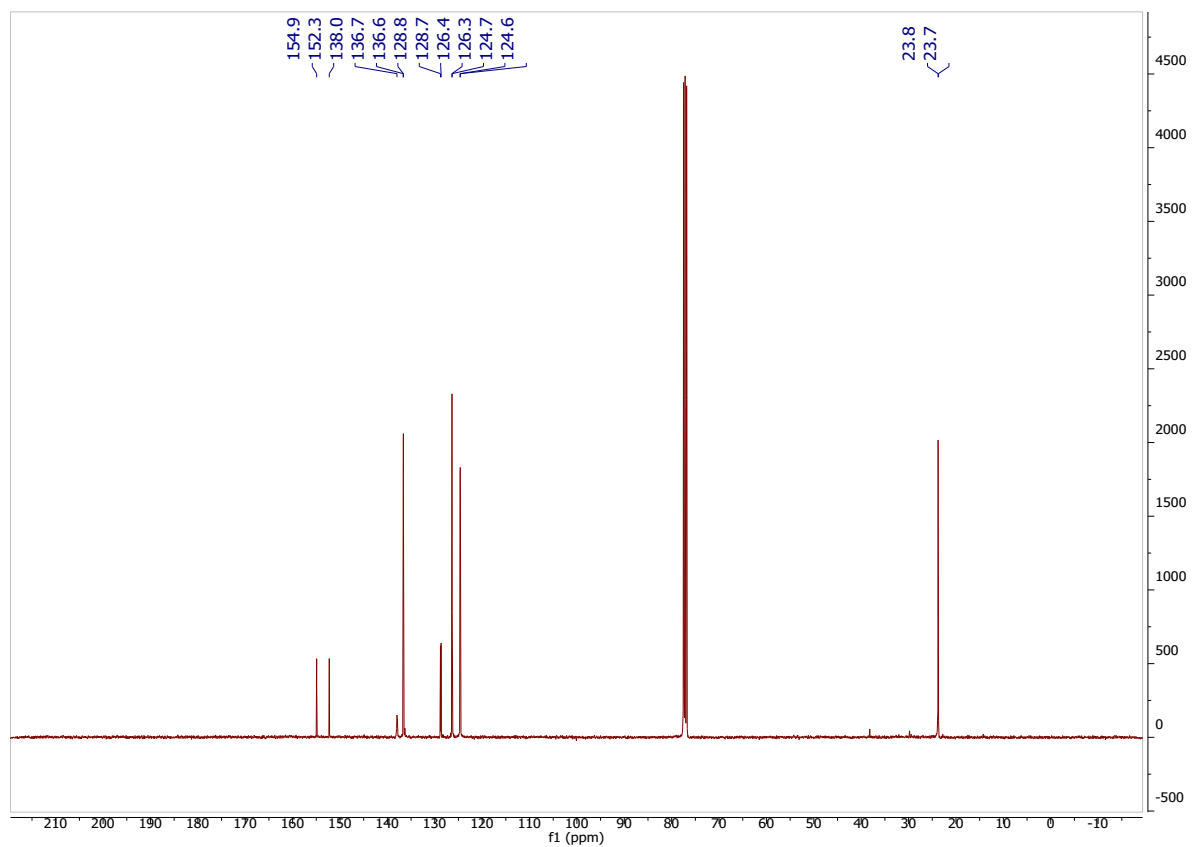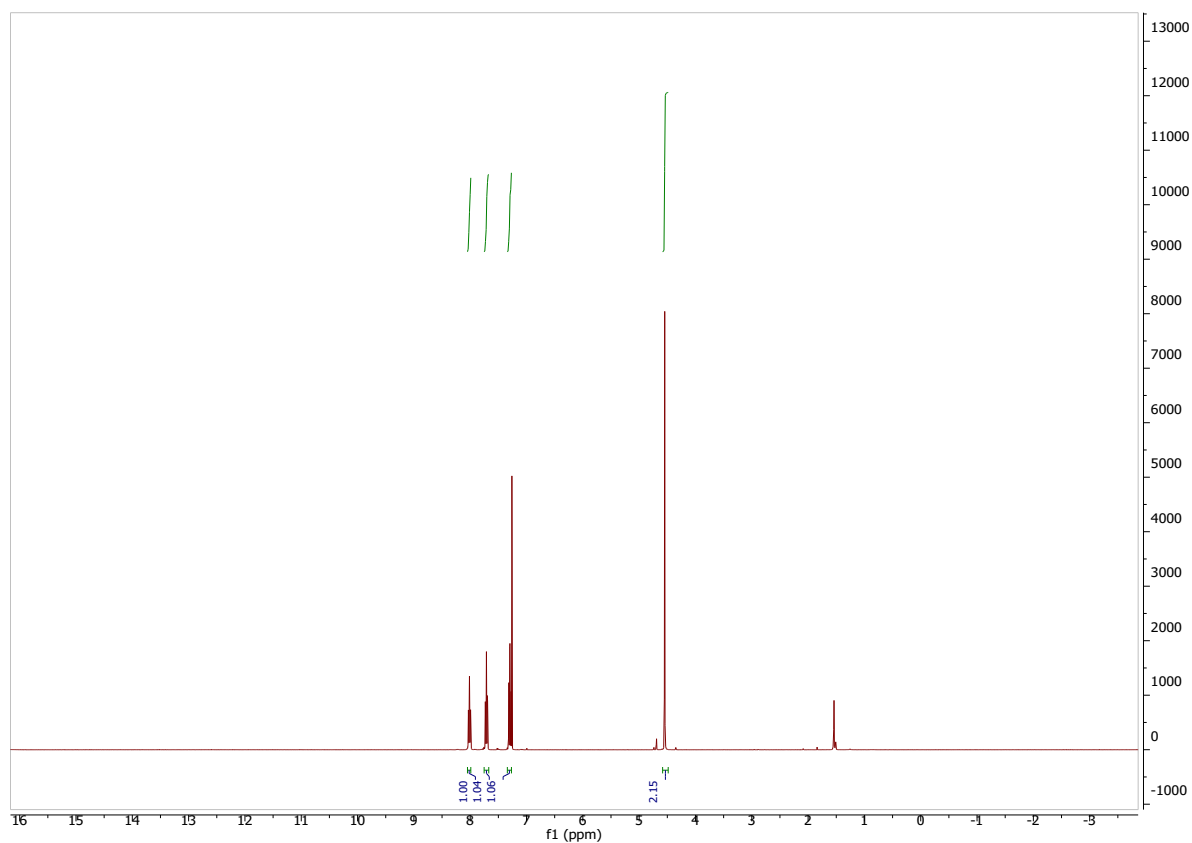
7.7.14 4-bromo-2-fluoro-1-(*tert*-butylthio) benzene **35**
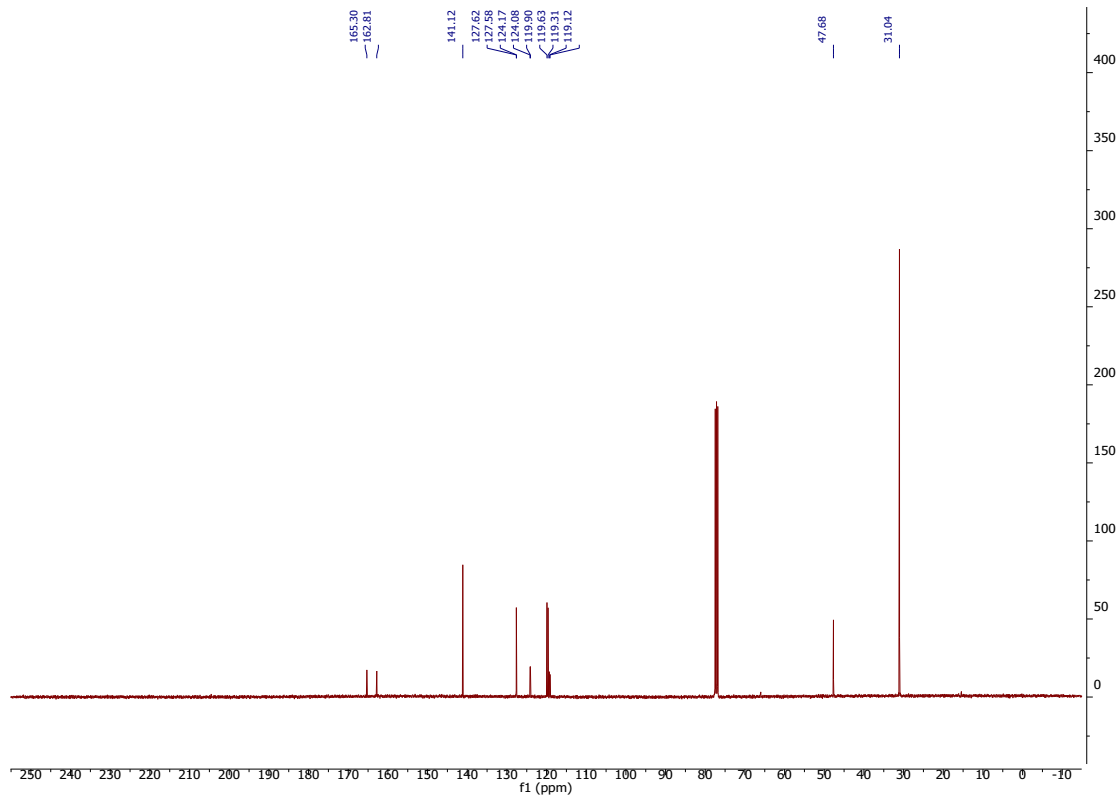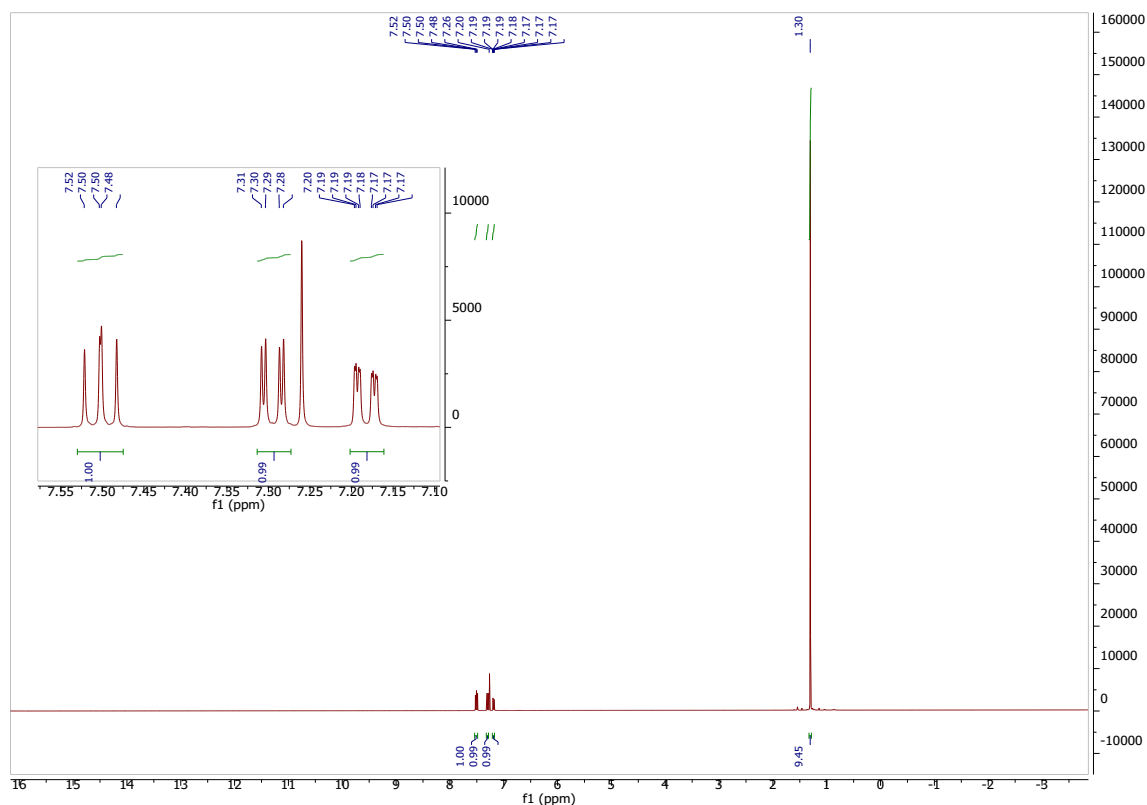
7.7.15 *tert*-Butyl (2-fluoro-4-((2-fluoro-3-nitrobenzyl) sulfonyl) phenyl) sulfane **37**
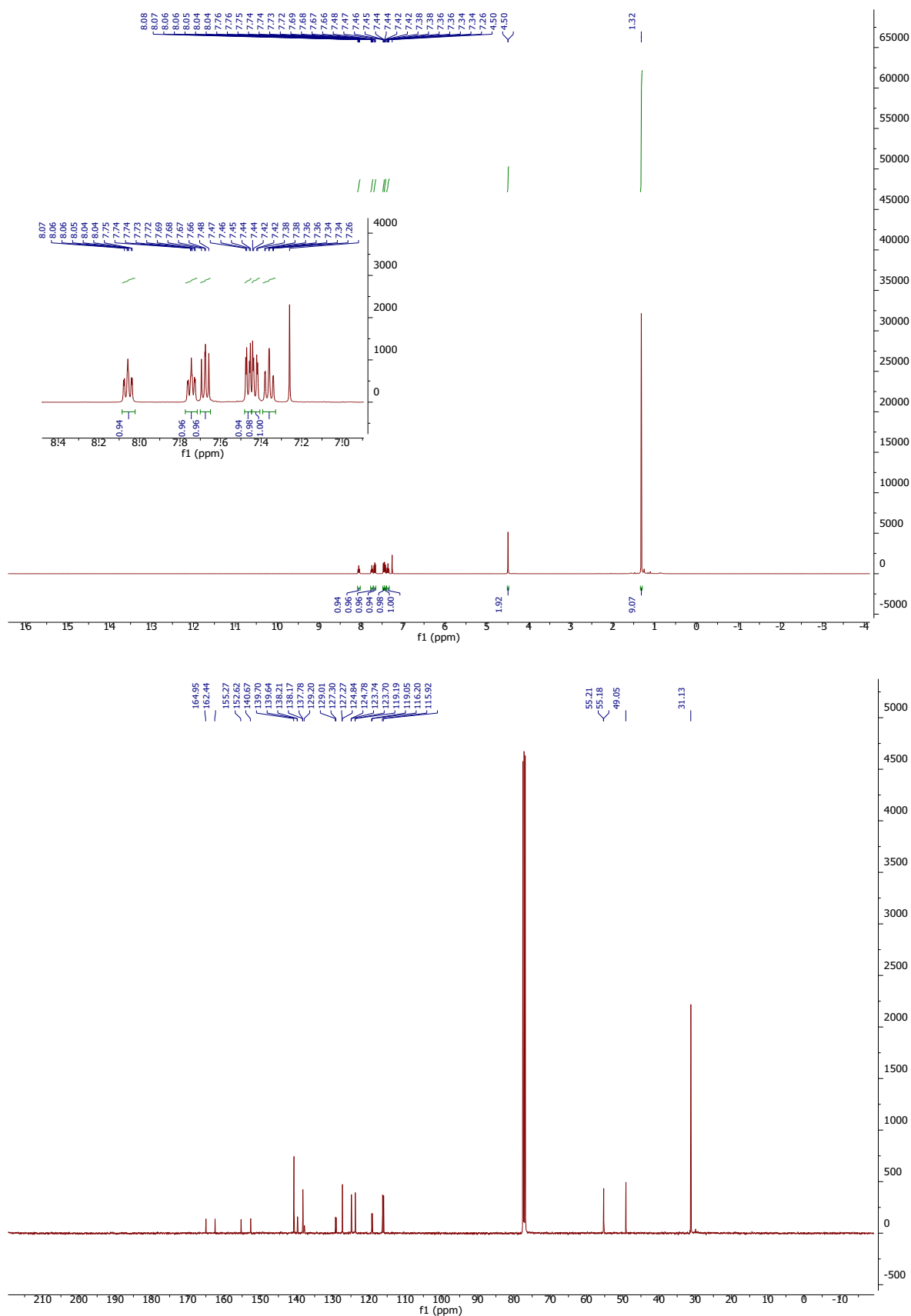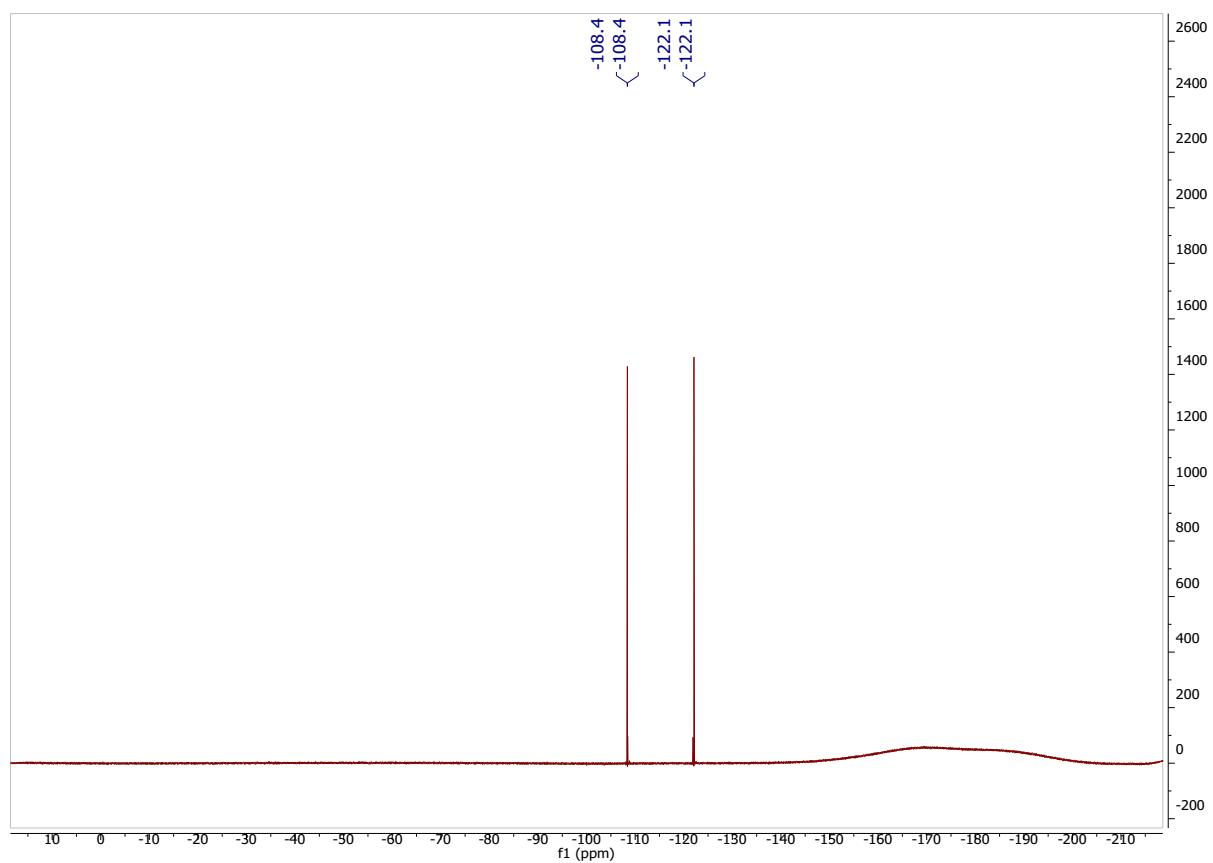
7.7.16 6-chloro-2-((2-fluoro-4-((2-fluoro-3-nitrobenzyl)sulfonyl)phenyl)thio)-5-methoxy-4-((5-methyl-1H-pyrazol-3-yl)amino) pyrimidine **38**
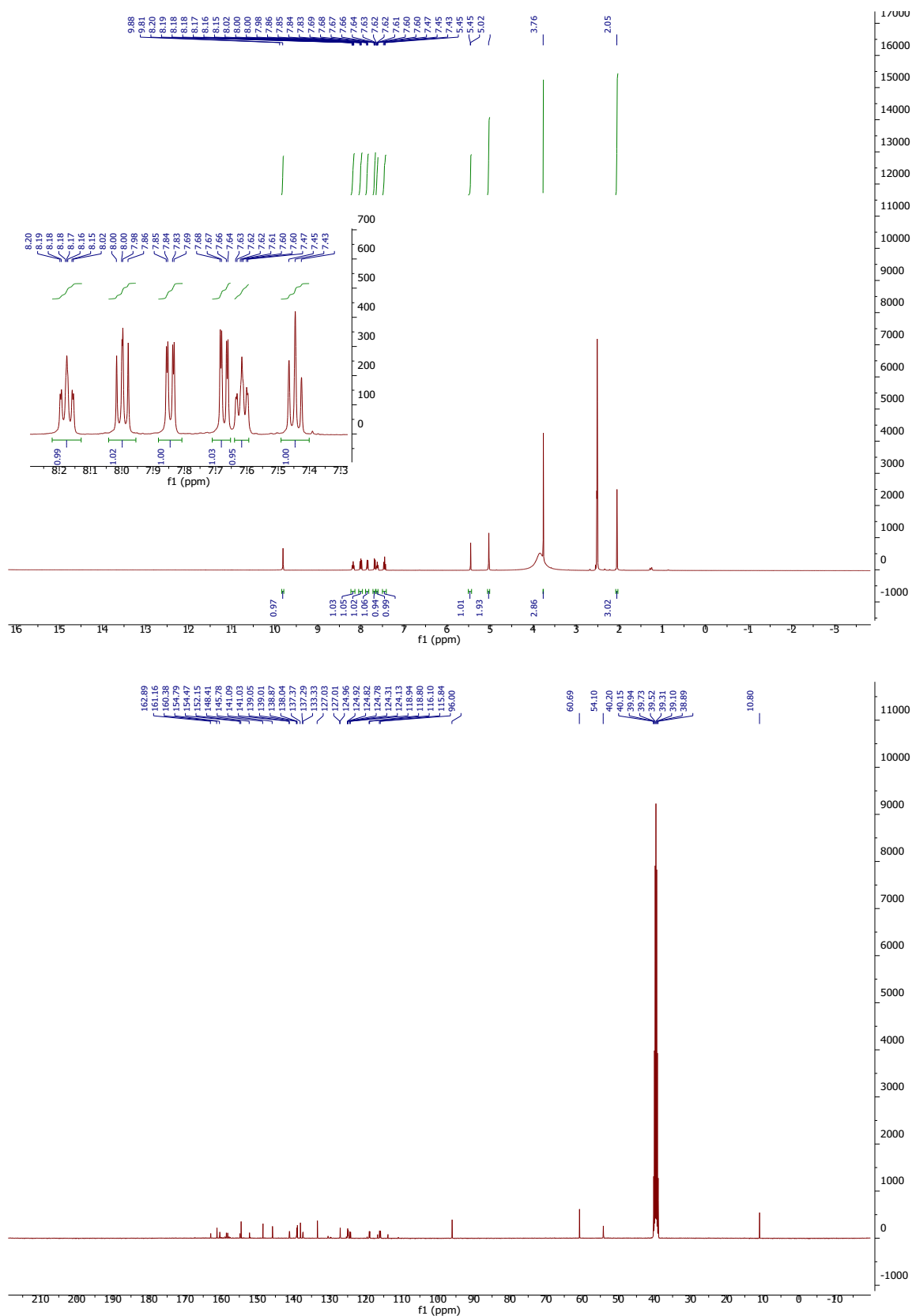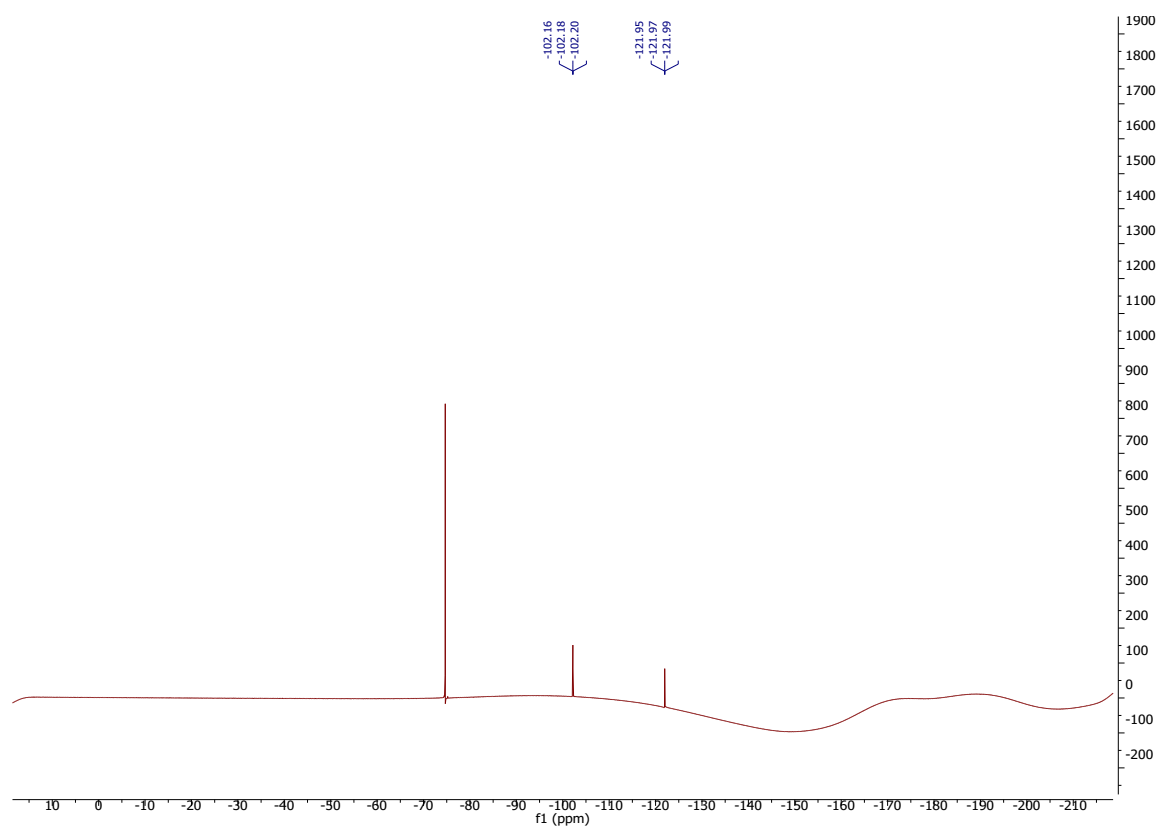
7.7.17 *tert*-Butyl 2-(4-(2-((2-fluoro-4-((2-fluoro-3-nitrobenzyl)sulfonyl)phenyl)thio)-5-methoxy-6-((5-methyl-1H-pyrazol-3-yl)amino)pyrimidin-4-yl)piperazin-1-yl)acetate **40a**
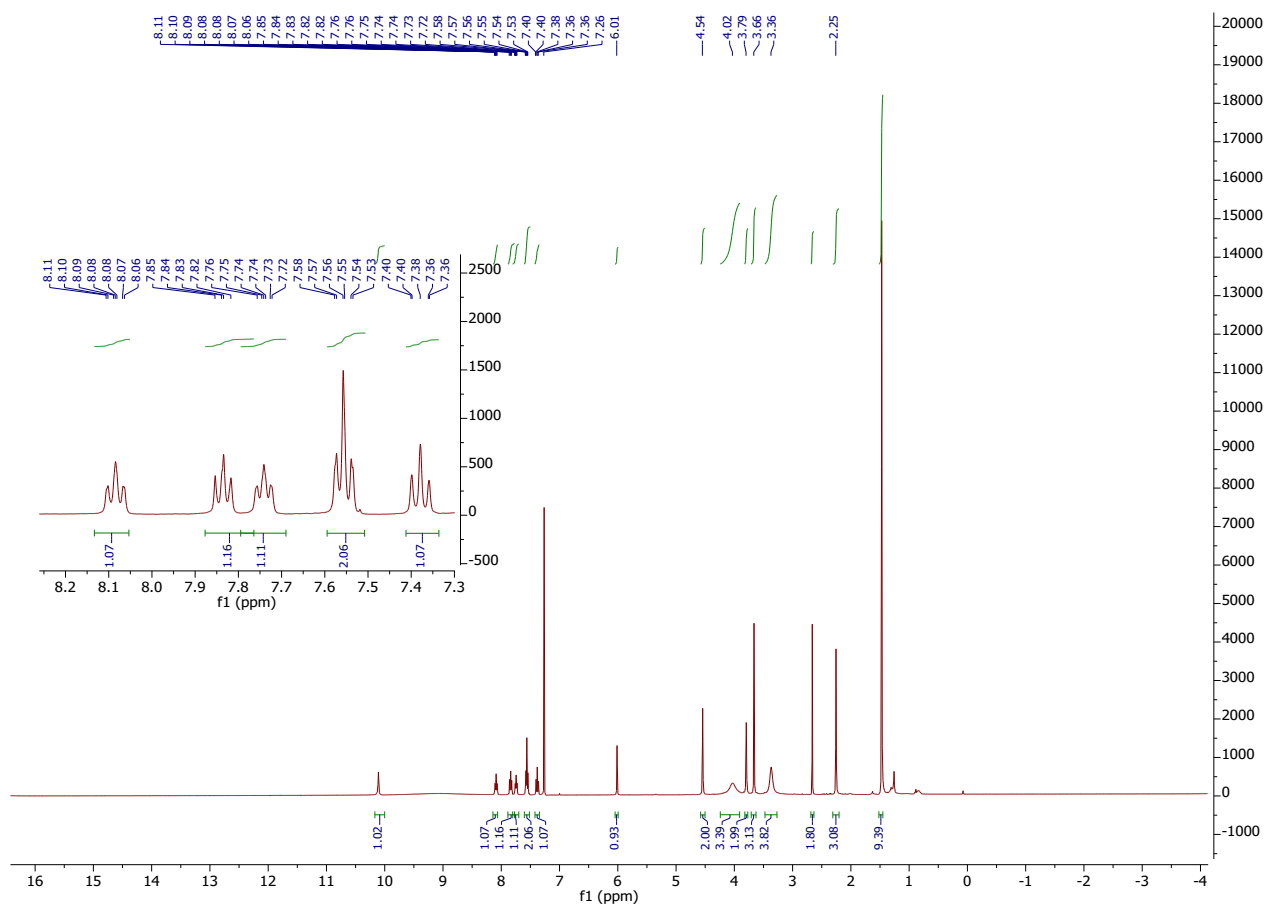
7.7.18 2-(4-(2-((2-fluoro-4-((2-fluoro-3-nitrobenzyl)sulfonyl)phenyl)thio)-5-methoxy-6-((5-methyl-1H-pyrazol-3-yl)amino)pyrimidin-4-yl)piperazin-1-yl)acetic acid **40b**
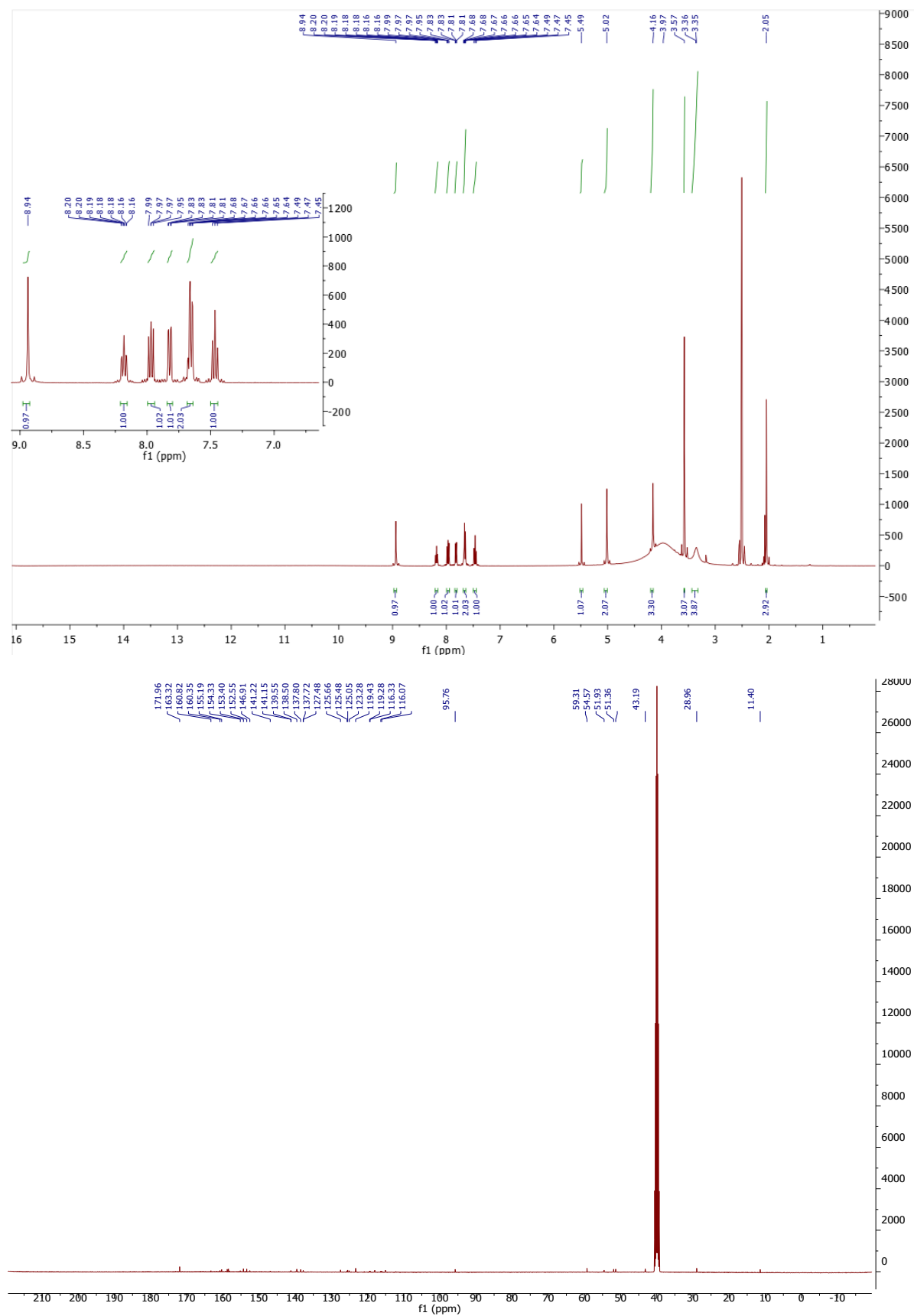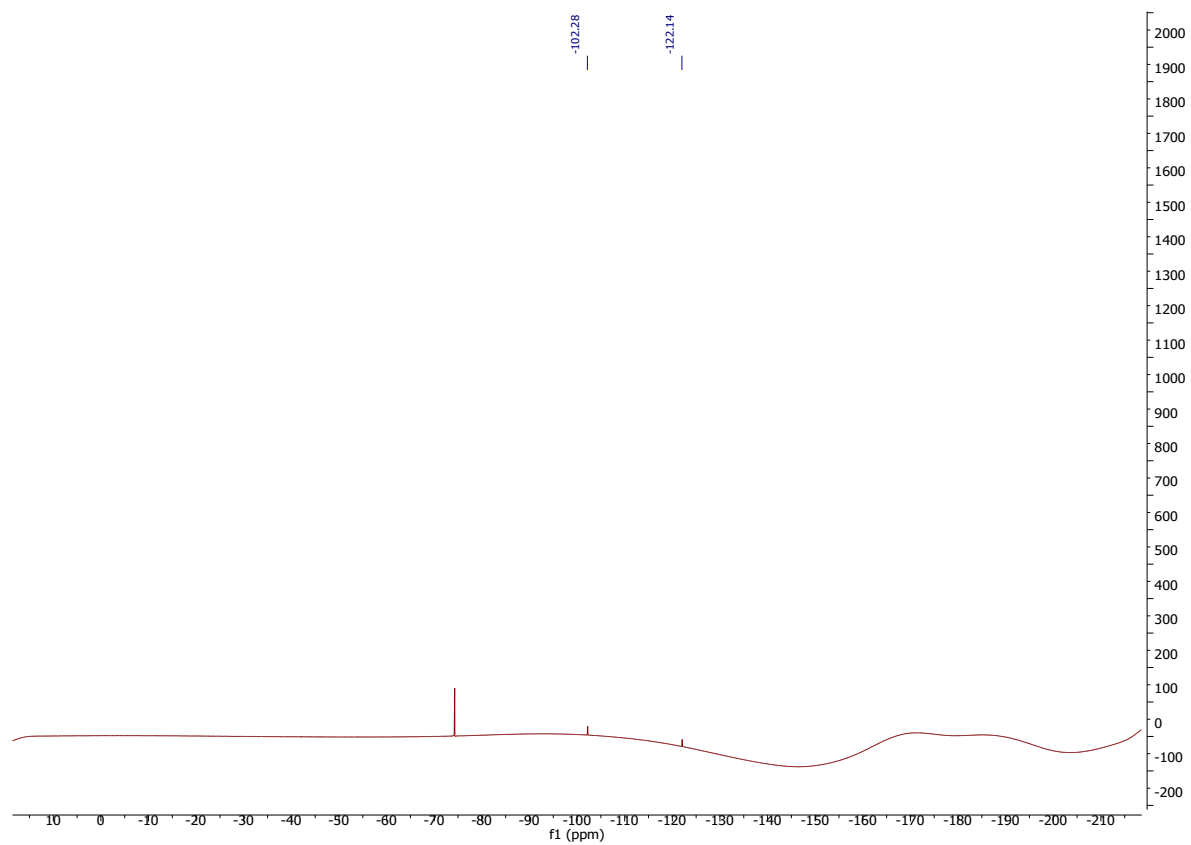
7.7.19 2-(4-(2-((2-fluoro-4-((2-fluoro-3-nitrobenzyl)sulfonyl)phenyl)thio)-5-methoxy-6-((5-methyl-1H-pyrazol-3-yl)amino)pyrimidin-4-yl)piperazin-1-yl)acetic acid **40c**
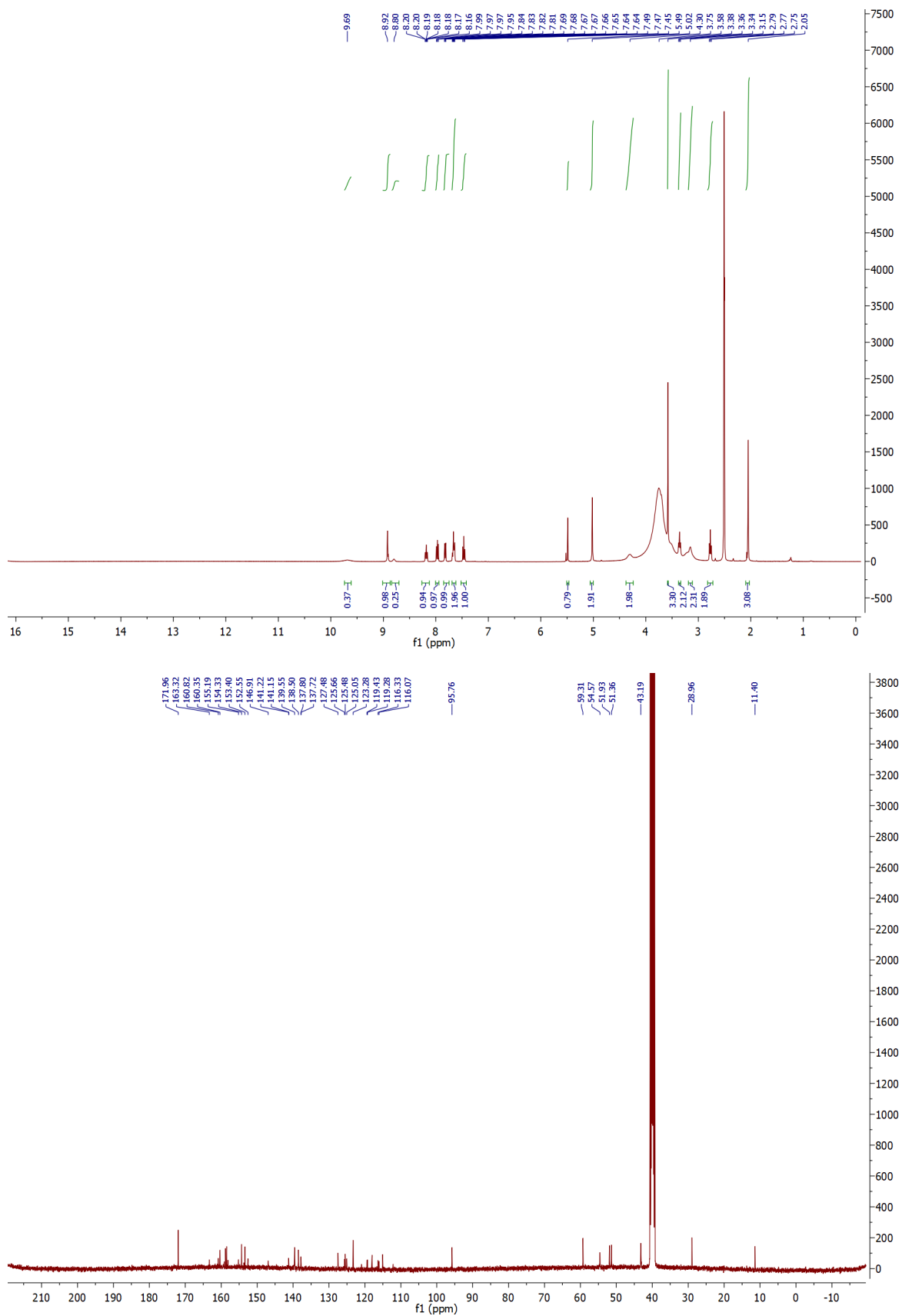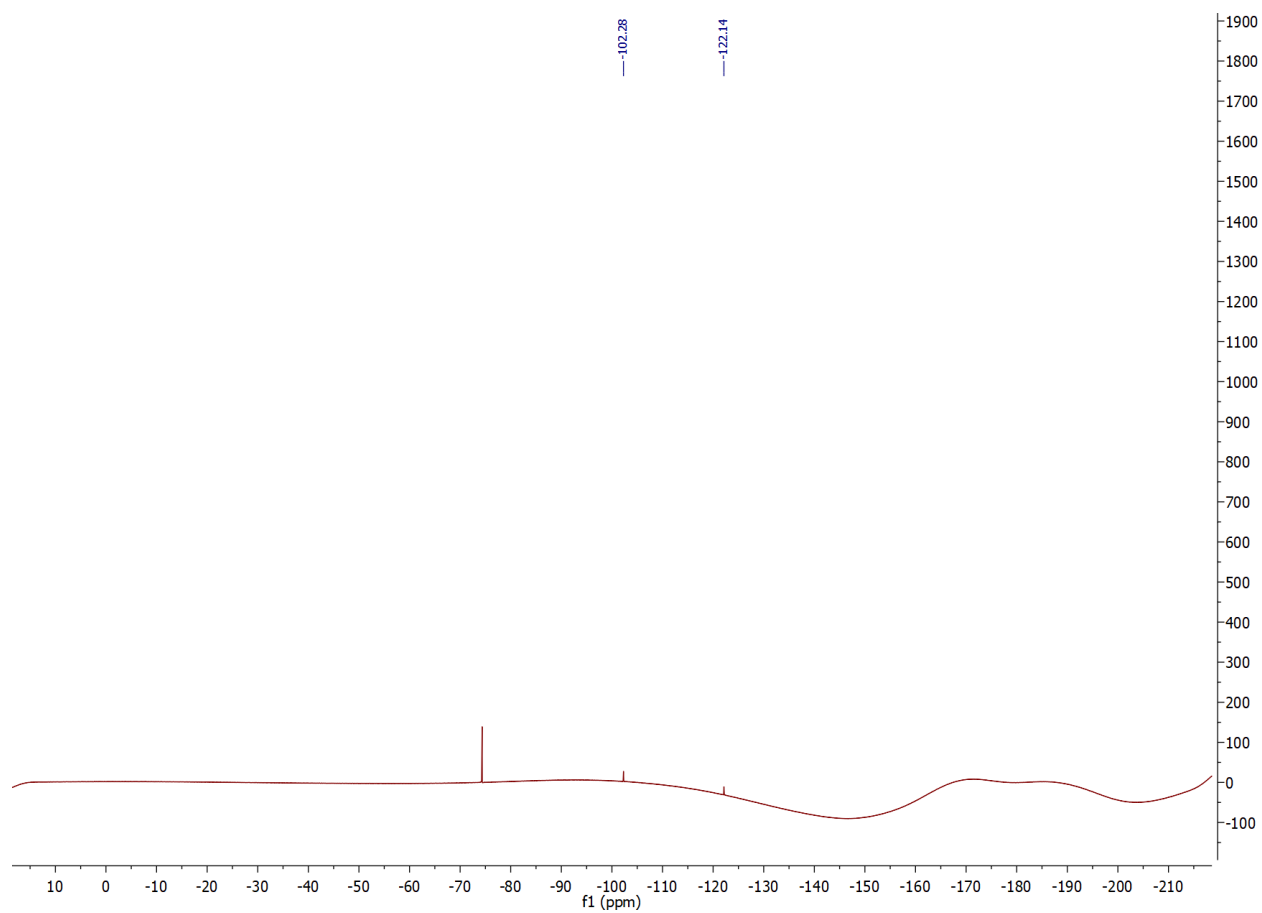
7.7.20 2-(1-(2-((2-fluoro-4-((2-fluoro-3-nitrobenzyl)sulfonyl)phenyl)thio)-5-methoxy-6-((5-methyl-1H-pyrazol-3-yl)amino)pyrimidin-4-yl)piperidin-4-yl) acetic acid **40d**
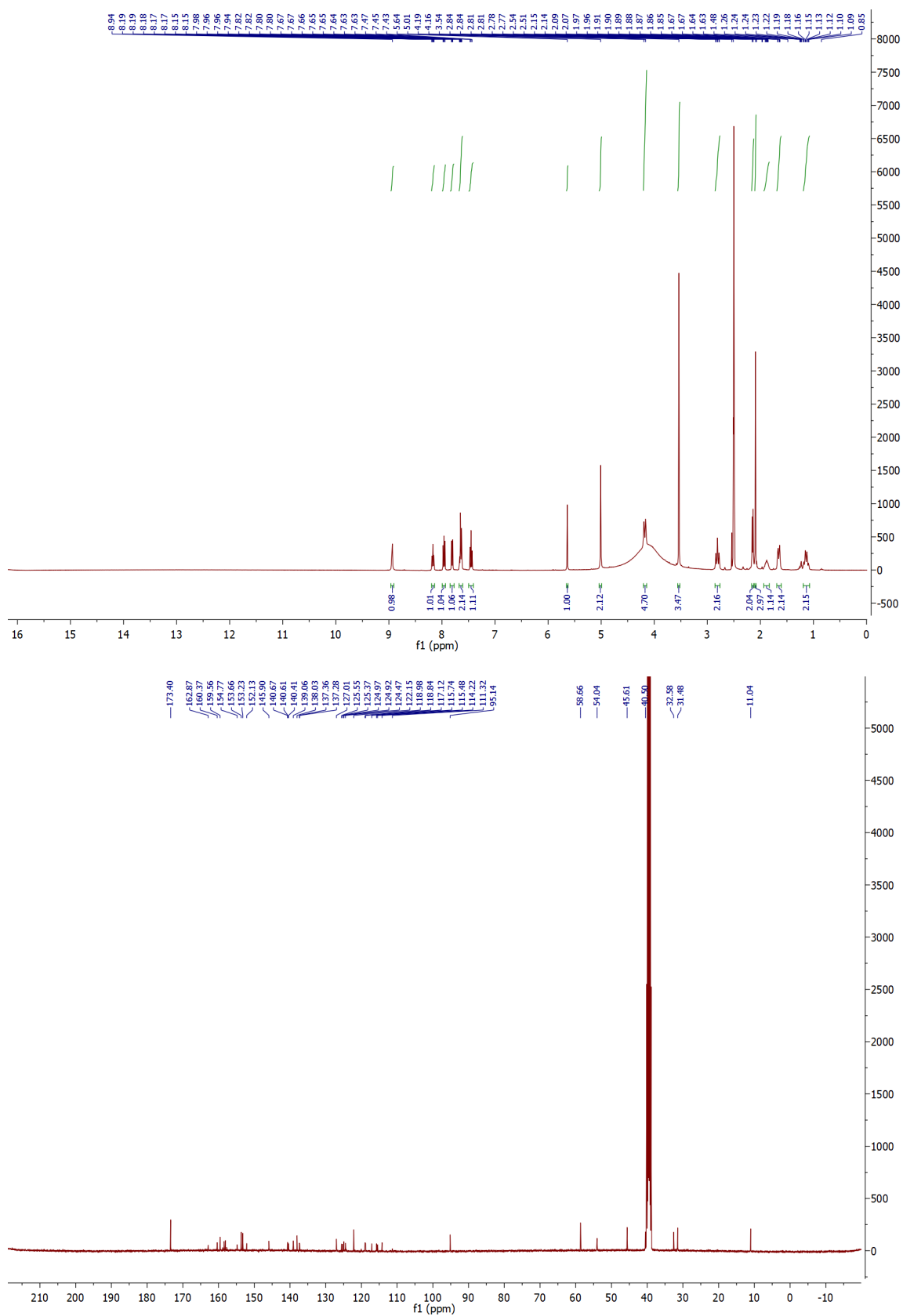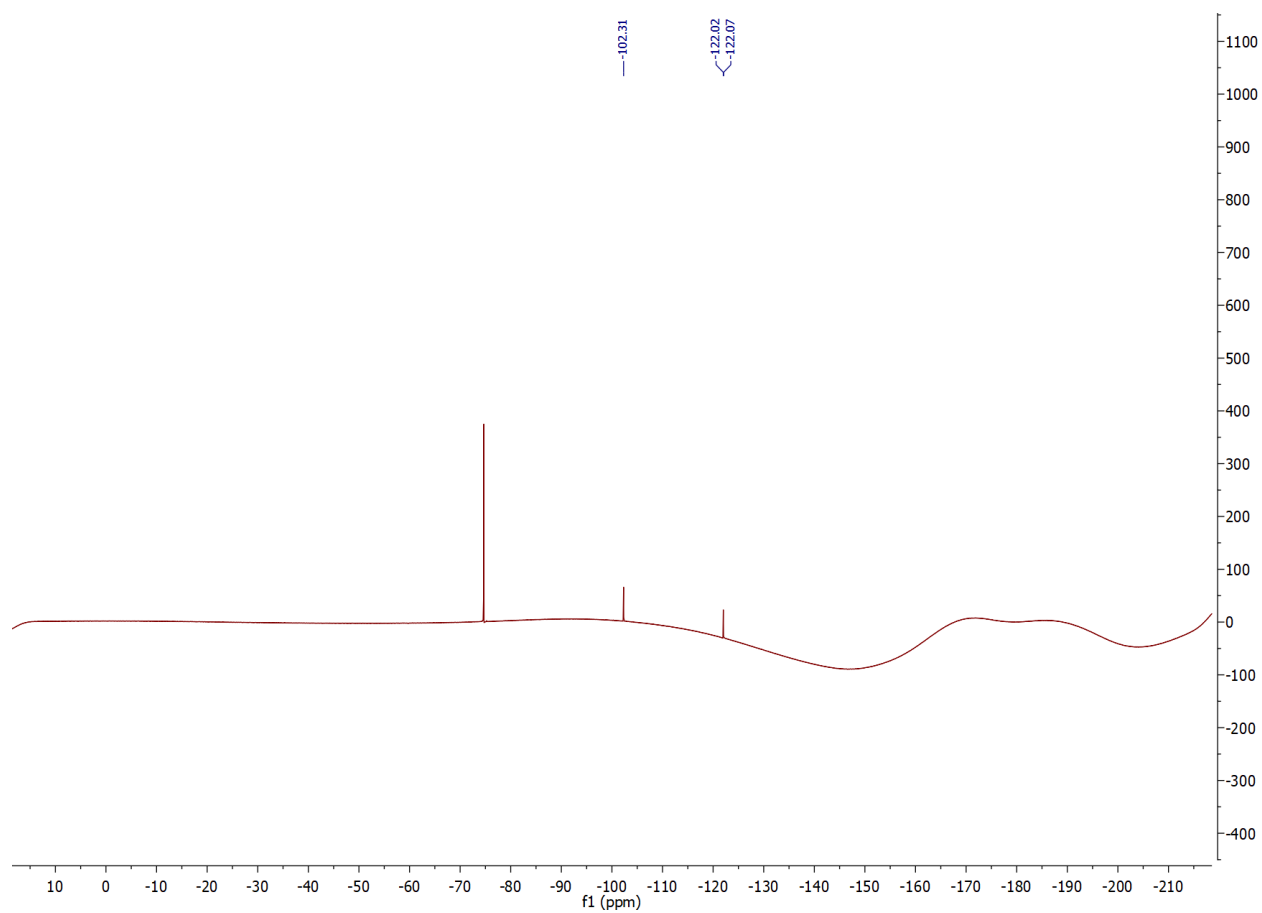
References

1. Lichtman, J. W.; Conchello, J. A., Fluorescence microscopy. *Nat Methods* **2005,** *2* (12), 910-9.

2. Sanderson, M. J.; Smith, I.; Parker, I.; Bootman, M. D., Fluorescence microscopy. *Cold Spring Harb Protoc* **2014,** *2014* (10).

3. Specht, E. A.; Braselmann, E.; Palmer, A. E., A Critical and Comparative Review of Fluorescent Tools for Live-Cell Imaging. *Annual Review of Physiology* **2017,** *79* (1), 93-117.

4. Lakowicz, J. R., *Principles of fluorescence spectroscopy*. 3rd ed.; Springer: New York, 2006; p xxvi, 954.

5. Liu, Z.; Lavis, Luke D.; Betzig, E., Imaging Live-Cell Dynamics and Structure at the Single-Molecule Level. *Molecular Cell* **2015,** *58* (4), 644-659.

6. Sydor, A. M.; Czymmek, K. J.; Puchner, E. M.; Mennella, V., Super-Resolution Microscopy: From Single Molecules to Supramolecular Assemblies. *Trends in Cell Biology* **2015,** *25* (12), 730-748.

7. Hell, S. W., Nanoscopy with Focused Light (Nobel Lecture). *Angewandte Chemie International Edition* **2015,** *54* (28), 8054-8066.

8. Moerner, W. E.; Kador, L., Optical detection and spectroscopy of single molecules in a solid. *Physical Review Letters* **1989,** *62* (21), 2535-2538.

9. Betzig, E.; Patterson, G. H.; Sougrat, R.; Lindwasser, O. W.; Olenych, S.; Bonifacino, J. S.; Davidson, M. W.; Lippincott-Schwartz, J.; Hess, H. F., Imaging Intracellular Fluorescent Proteins at Nanometer Resolution. *Science* **2006,** *313* (5793), 1642.

10. Hess, S. T.; Girirajan, T. P. K.; Mason, M. D., Ultra-High Resolution Imaging by Fluorescence Photoactivation Localization Microscopy. *Biophysical Journal* **2006,** *91* (11), 4258-4272.

11. Hell, S. W.; Wichmann, J., Breaking the diffraction resolution limit by stimulated emission: stimulated-emission-depletion fluorescence microscopy. *Opt. Lett.* **1994,** *19* (11), 780-782.

12. Sahl, S. J.; Hell, S. W.; Jakobs, S., Fluorescence nanoscopy in cell biology. *Nature Reviews Molecular Cell Biology* **2017,** *18*, 685.

13. Sauer, M.; Heilemann, M., Single-Molecule Localization Microscopy in Eukaryotes. *Chemical Reviews* **2017,** *117* (11), 7478-7509.

14. Wang, L.; Frei, M. S.; Salim, A.; Johnsson, K., Small-Molecule Fluorescent Probes for Live-Cell Super-Resolution Microscopy. *J Am Chem Soc* **2019,** *141* (7), 2770-2781.

15. van de Linde, S.; Heilemann, M.; Sauer, M., Live-cell super-resolution imaging with synthetic fluorophores. *Annu Rev Phys Chem* **2012,** *63*, 519-40.

16. Lavis, L. D.; Raines, R. T., Bright building blocks for chemical biology. *ACS Chem Biol* **2014,** *9* (4), 855-66.

17. Rodriguez, E. A.; Campbell, R. E.; Lin, J. Y.; Lin, M. Z.; Miyawaki, A.; Palmer, A. E.; Shu, X.; Zhang, J.; Tsien, R. Y., The Growing and Glowing Toolbox of Fluorescent and Photoactive Proteins. *Trends Biochem Sci* **2017,** *42* (2), 111-129.

18. Mishin, A. S.; Belousov, V. V.; Solntsev, K. M.; Lukyanov, K. A., Novel uses of fluorescent proteins. *Curr Opin Chem Biol* **2015,** *27*, 1-9.

19. Shcherbakova, D. M.; Sengupta, P.; Lippincott-Schwartz, J.; Verkhusha, V. V., Photocontrollable fluorescent proteins for superresolution imaging. *Annu Rev Biophys* **2014,** *43*, 303-29.

20. Chudakov, D. M.; Matz, M. V.; Lukyanov, S.; Lukyanov, K. A., Fluorescent Proteins and Their Applications in Imaging Living Cells and Tissues. *Physiological Reviews* **2010,** *90* (3), 1103-1163.

21. Jin, D.; Xi, P.; Wang, B.; Zhang, L.; Enderlein, J.; van Oijen, A. M., Nanoparticles for super-resolution microscopy and single-molecule tracking. *Nat Methods* **2018,** *15* (6), 415-423.

22. Wolfbeis, O. S., An overview of nanoparticles commonly used in fluorescent bioimaging. *Chem Soc Rev* **2015,** *44* (14), 4743-68.

23. Lavis, L. D., Teaching Old Dyes New Tricks: Biological Probes Built from Fluoresceins and Rhodamines. *Annu Rev Biochem* **2017,** *86*, 825-843.

24. Karstens, T.; Kobs, K., Rhodamine B and rhodamine 101 as reference substances for fluorescence quantum yield measurements. *The Journal of Physical Chemistry* **1980,** *84* (14), 1871-1872.

25.   Zhang, X.-F.; Su, N.; Lu, X.; Jia, W., Benzoate-modified rhodamine dyes: Large change in fluorescence properties due to photoinduced electron transfer. *Journal of Luminescence* **2016,** *179*, 511-517.

26.   Butkevich, A. N.; Mitronova, G. Y.; Sidenstein, S. C.; Klocke, J. L.; Kamin, D.; Meineke, D. N. H.; D'Este, E.; Kraemer, P.-T.; Danzl, J. G.; Belov, V. N.; Hell, S. W., Fluorescent Rhodamines and Fluorogenic Carbopyronines for Super-Resolution STED Microscopy in Living Cells. *Angewandte Chemie International Edition* **2016,** *55* (10), 3290-3294.

27.   Lukinavicius, G.; Umezawa, K.; Olivier, N.; Honigmann, A.; Yang, G.; Plass, T.; Mueller, V.; Reymond, L.; Correa, I. R., Jr.; Luo, Z. G.; Schultz, C.; Lemke, E. A.; Heppenstall, P.; Eggeling, C.; Manley, S.; Johnsson, K., A near-infrared fluorophore for live-cell super-resolution microscopy of cellular proteins. *Nat Chem* **2013,** *5* (2), 132-9.

28.   Lukinavicius, G.; Reymond, L.; Umezawa, K.; Sallin, O.; D'Este, E.; Gottfert, F.; Ta, H.; Hell, S. W.; Urano, Y.; Johnsson, K., Fluorogenic Probes for Multicolor Imaging in Living Cells. *J Am Chem Soc* **2016,** *138* (30), 9365-8.

29.   Wurm, C. A.; Kolmakov, K.; Göttfert, F.; Ta, H.; Bossi, M.; Schill, H.; Berning, S.; Jakobs, S.; Donnert, G.; Belov, V. N.; Hell, S. W., Novel red fluorophores with superior performance in STED microscopy. *Optical Nanoscopy* **2012,** *1* (1), 7.

30.   Mitronova, G. Y.; Belov, V. N.; Bossi, M. L.; Wurm, C. A.; Meyer, L.; Medda, R.; Moneron, G.; Bretschneider, S.; Eggeling, C.; Jakobs, S.; Hell, S. W., New Fluorinated Rhodamines for Optical Microscopy and Nanoscopy. *Chemistry – A European Journal* **2010,** *16* (15), 4477-4488.

31.   Kolmakov, K.; Wurm, C. A.; Meineke, D. N. H.; Göttfert, F.; Boyarskiy, V. P.; Belov, V. N.; Hell, S. W., Polar Red-Emitting Rhodamine Dyes with Reactive Groups: Synthesis, Photophysical Properties, and Two-Color STED Nanoscopy Applications. *Chemistry – A European Journal* **2014,** *20* (1), 146-157.

32.   Grimm, J. B.; English, B. P.; Chen, J.; Slaughter, J. P.; Zhang, Z.; Revyakin, A.; Patel, R.; Macklin, J. J.; Normanno, D.; Singer, R. H.; Lionnet, T.; Lavis, L. D., A general method to improve fluorophores for live-cell and single-molecule microscopy. *Nature Methods* **2015,** *12*, 244.

33.   Grimm, J. B.; Muthusamy, A. K.; Liang, Y.; Brown, T. A.; Lemon, W. C.; Patel, R.; Lu, R.; Macklin, J. J.; Keller, P. J.; Ji, N.; Lavis, L. D., A general method to fine-tune fluorophores for live-cell and in vivo imaging. *Nature Methods* **2017,** *14*, 987.

34.   Li, X.; Gao, X.; Shi, W.; Ma, H., Design Strategies for Water-Soluble Small Molecular Chromogenic and Fluorogenic Probes. *Chemical Reviews* **2014,** *114* (1), 590-659.

35.   Bubb, M. R.; Senderowicz, A. M.; Sausville, E. A.; Duncan, K. L.; Korn, E. D., Jasplakinolide, a cytotoxic natural product, induces actin polymerization and competitively inhibits the binding of phalloidin to F-actin. *Journal of Biological Chemistry* **1994,** *269* (21), 14869-14871.

36.   Lukinavicius, G.; Reymond, L.; D'Este, E.; Masharina, A.; Gottfert, F.; Ta, H.; Guther, A.; Fournier, M.; Rizzo, S.; Waldmann, H.; Blaukopf, C.; Sommer, C.; Gerlich, D. W.; Arndt, H. D.; Hell, S. W.; Johnsson, K., Fluorogenic probes for live-cell imaging of the cytoskeleton. *Nat Methods* **2014,** *11* (7), 731-3.

37.   Lukinavicius, G.; Mitronova, G. Y.; Schnorrenberg, S.; Butkevich, A. N.; Barthel, H.; Belov, V. N.; Hell, S. W., Fluorescent dyes and probes for super-resolution microscopy of microtubules and tracheoles in living cells and tissues. *Chem Sci* **2018,** *9* (13), 3324-3334.

38.   Lukinavicius, G.; Blaukopf, C.; Pershagen, E.; Schena, A.; Reymond, L.; Derivery, E.; Gonzalez-Gaitan, M.; D'Este, E.; Hell, S. W.; Wolfram Gerlich, D.; Johnsson, K., SiR-Hoechst is a far-red DNA stain for live-cell nanoscopy. *Nat Commun* **2015,** *6*, 8497.

39.   Thompson, A. D.; Bewersdorf, J.; Toomre, D.; Schepartz, A., HIDE Probes: A New Toolkit for Visualizing Organelle Dynamics, Longer and at Super-Resolution. *Biochemistry* **2017,** *56* (39), 5194-5201.

40.   Butkevich, A. N.; Belov, V. N.; Kolmakov, K.; Sokolov, V. V.; Shojaei, H.; Sidenstein, S. C.; Kamin, D.; Matthias, J.; Vlijm, R.; Engelhardt, J.; Hell, S. W., Hydroxylated Fluorescent Dyes for Live-Cell Labeling: Synthesis, Spectra and Super-Resolution STED. *Chemistry – A European Journal* **2017,** *23* (50), 12114-12119.

41.   Grimm, J. B.; Sung, A. J.; Legant, W. R.; Hulamm, P.; Matlosz, S. M.; Betzig, E.; Lavis, L. D., Carbofluoresceins and carborhodamines as scaffolds for high-contrast fluorogenic probes. *ACS chemical biology* **2013,** *8* (6), 1303-1310.

42.   Kozma, E.; Estrada Girona, G.; Paci, G.; Lemke, E. A.; Kele, P., Bioorthogonal double-fluorogenic siliconrhodamine probes for intracellular super-resolution microscopy. *Chemical Communications* **2017,** *53* (50), 6696-6699.

43.   Knorr, G.; Kozma, E.; Schaart, J. M.; Németh, K.; Török, G.; Kele, P., Bioorthogonally Applicable Fluorogenic Cyanine-Tetrazines for No-Wash Super-Resolution Imaging. *Bioconjugate Chemistry* **2018,** *29* (4), 1312-1318.

44.   Jones, S. A.; Shim, S.-H.; He, J.; Zhuang, X., Fast, three-dimensional super-resolution imaging of live cells. *Nature Methods* **2011,** *8* (6), 499-505.

45.   McNeil, P. L.; Warder, E., Glass beads load macromolecules into living cells. *Journal of Cell Science* **1987,** *88* (5), 669.

46.   Kollmannsperger, A.; Sharei, A.; Raulf, A.; Heilemann, M.; Langer, R.; Jensen, K. F.; Wieneke, R.; Tampé, R., Live-cell protein labelling with nanometre precision by cell squeezing. *Nature Communications* **2016,** *7* (1), 10372.

47.   Yang, N. J.; Hinner, M. J., Getting Across the Cell Membrane: An Overview for Small Molecules, Peptides, and Proteins. In *Site-Specific Protein Labeling: Methods and Protocols*, Gautier, A.; Hinner, M. J., Eds. Springer New York: New York, NY, 2015; pp 29-53.

48.   Lipinski, C. A.; Lombardo, F.; Dominy, B. W.; Feeney, P. J., Experimental and computational approaches to estimate solubility and permeability in drug discovery and development settings1PII of original article: S0169-409X(96)00423-1. The article was originally published in Advanced Drug Delivery Reviews 23 (1997) 3–25.1. *Advanced Drug Delivery Reviews* **2001,** *46* (1), 3-26.

49.   Wang, L.; Tran, M.; D'Este, E.; Roberti, J.; Koch, B.; Xue, L.; Johnsson, K., A general strategy to develop cell permeable and fluorogenic probes for multicolour nanoscopy. *Nature Chemistry* **2019**.

50.   Schnell, U.; Dijk, F.; Sjollema, K. A.; Giepmans, B. N. G., Immunolabeling artifacts and the need for live-cell imaging. *Nature Methods* **2012,** *9* (2), 152-158.

51.   Tsien, R. Y., THE GREEN FLUORESCENT PROTEIN. *Annual Review of Biochemistry* **1998,** *67* (1), 509-544.

52.   Keppler, A.; Gendreizig, S.; Gronemeyer, T.; Pick, H.; Vogel, H.; Johnsson, K., A general method for the covalent labeling of fusion proteins with small molecules in vivo. *Nature Biotechnology* **2003,** *21* (1), 86-89.

53.   Crivat, G.; Taraska, J. W., Imaging proteins inside cells with fluorescent tags. *Trends in Biotechnology* **2012,** *30* (1), 8-16.

54.   Xue, L.; Karpenko, I. A.; Hiblot, J.; Johnsson, K., Imaging and manipulating proteins in live cells through covalent labeling. *Nature Chemical Biology* **2015,** *11*, 917.

55.   Los, G. V.; Encell, L. P.; McDougall, M. G.; Hartzell, D. D.; Karassina, N.; Zimprich, C.; Wood, M. G.; Learish, R.; Ohana, R. F.; Urh, M.; Simpson, D.; Mendez, J.; Zimmerman, K.; Otto, P.; Vidugiris, G.; Zhu, J.; Darzins, A.; Klaubert, D. H.; Bulleit, R. F.; Wood, K. V., HaloTag: A Novel Protein Labeling Technology for Cell Imaging and Protein Analysis. *ACS Chemical Biology* **2008,** *3* (6), 373-382.

56.   Gautier, A.; Juillerat, A.; Heinis, C.; Corrêa, I. R., Jr.; Kindermann, M.; Beaufils, F.; Johnsson, K., An Engineered Protein Tag for Multiprotein Labeling in Living Cells. *Chemistry & Biology* **2008,** *15* (2), 128-136.

57.   Miller, L. W.; Cai, Y.; Sheetz, M. P.; Cornish, V. W., In vivo protein labeling with trimethoprim conjugates: a flexible chemical tag. *Nature Methods* **2005,** *2* (4), 255-257.

58.   Hauke, S.; Best, M.; Schmidt, T. T.; Baalmann, M.; Krause, A.; Wombacher, R., Two-Step Protein Labeling Utilizing Lipoic Acid Ligase and Sonogashira Cross-Coupling. *Bioconjugate Chemistry* **2014,** *25* (9), 1632-1637.

59.   Lukinavičius, G.; Lavogina, D.; Orpinell, M.; Umezawa, K.; Reymond, L.; Garin, N.; Gönczy, P.; Johnsson, K., Selective Chemical Crosslinking Reveals a Cep57-Cep63-Cep152 Centrosomal Complex. *Current Biology* **2013,** *23* (3), 265-270.

60.   Chin, J. W., Expanding and Reprogramming the Genetic Code of Cells and Animals. *Annual Review of Biochemistry* **2014,** *83* (1), 379-408.

61.   Lang, K.; Chin, J. W., Cellular Incorporation of Unnatural Amino Acids and Bioorthogonal Labeling of Proteins. *Chemical Reviews* **2014,** *114* (9), 4764-4806.

62.   Dumontet, C.; Jordan, M. A., Microtubule-binding agents: a dynamic field of cancer therapeutics. *Nat Rev Drug Discov* **2010,** *9* (10), 790-803.

63.   Banterle, N.; Gonczy, P., Centriole Biogenesis: From Identifying the Characters to Understanding the Plot. *Annu Rev Cell Dev Biol* **2017,** *33*, 23-49.

64.   Breslow, D. K.; Holland, A. J., Mechanism and Regulation of Centriole and Cilium Biogenesis. *Annu Rev Biochem* **2019,** *88*, 691-724.

65.   Nigg, E. A.; Holland, A. J., Once and only once: mechanisms of centriole duplication and their deregulation in disease. *Nat Rev Mol Cell Biol* **2018,** *19* (5), 297-312.

66.   Sillibourne, J. E.; Bornens, M., Polo-like kinase 4: the odd one out of the family. *Cell Division* **2010,** *5* (1), 25.

67.   Gonczy, P., Towards a molecular architecture of centriole assembly. *Nat Rev Mol Cell Biol* **2012,** *13* (7), 425-35.

68.   Guichard, P.; Hachet, V.; Majubu, N.; Neves, A.; Demurtas, D.; Olieric, N.; Fluckiger, I.; Yamada, A.; Kihara, K.; Nishida, Y.; Moriya, S.; Steinmetz, Michel O.; Hongoh, Y.; Gönczy, P., Native Architecture of the Centriole Proximal Region Reveals Features Underlying Its 9-Fold Radial Symmetry. *Current Biology* **2013,** *23* (17), 1620-1628.

69.   Andersen, J. S.; Wilkinson, C. J.; Mayor, T.; Mortensen, P.; Nigg, E. A.; Mann, M., Proteomic characterization of the human centrosome by protein correlation profiling. *Nature* **2003,** *426* (6966), 570-574.

70.   Sieben, C.; Banterle, N.; Douglass, K. M.; Gönczy, P.; Manley, S., Multicolor single-particle reconstruction of protein complexes. *Nature Methods* **2018,** *15* (10), 777-780.

71.   Kim, T. S.; Park, J. E.; Shukla, A.; Choi, S.; Murugan, R. N.; Lee, J. H.; Ahn, M.; Rhee, K.; Bang, J. K.; Kim, B. Y.; Loncarek, J.; Erikson, R. L.; Lee, K. S., Hierarchical recruitment of Plk4 and regulation of centriole biogenesis by two centrosomal scaffolds, Cep192 and Cep152. *Proc Natl Acad Sci U S A* **2013,** *110* (50), 4849-57.

72.   Sonnen, K. F.; Gabryjonczyk, A. M.; Anselm, E.; Stierhof, Y. D.; Nigg, E. A., Human Cep192 and Cep152 cooperate in Plk4 recruitment and centriole duplication. *J Cell Sci* **2013,** *126* (Pt 14), 3223-33.

73.   Sonnen, K. F.; Schermelleh, L.; Leonhardt, H.; Nigg, E. A., 3D-structured illumination microscopy provides novel insight into architecture of human centrosomes. *Biology Open* **2012,** *1* (10), 965.

74.   Park, S. Y.; Park, J. E.; Kim, T. S.; Kim, J. H.; Kwak, M. J.; Ku, B.; Tian, L.; Murugan, R. N.; Ahn, M.; Komiya, S.; Hojo, H.; Kim, N. H.; Kim, B. Y.; Bang, J. K.; Erikson, R. L.; Lee, K. W.; Kim, S. J.; Oh, B. H.; Yang, W.; Lee, K. S., Molecular basis for unidirectional scaffold switching of human Plk4 in centriole biogenesis. *Nat Struct Mol Biol* **2014,** *21* (8), 696-703.

75.   Arquint, C.; Nigg, E. A., The PLK4-STIL-SAS-6 module at the core of centriole duplication. *Biochem Soc Trans* **2016,** *44* (5), 1253-1263.

76.   Ohta, M.; Ashikawa, T.; Nozaki, Y.; Kozuka-Hata, H.; Goto, H.; Inagaki, M.; Oyama, M.; Kitagawa, D., Direct interaction of Plk4 with STIL ensures formation of a single procentriole per parental centriole. *Nat Commun* **2014,** *5*, 5267.

77.   Kitagawa, D.; Vakonakis, I.; Olieric, N.; Hilbert, M.; Keller, D.; Olieric, V.; Bortfeld, M.; Erat, M. C.; Flückiger, I.; Gönczy, P.; Steinmetz, M. O., Structural Basis of the 9-Fold Symmetry of Centrioles. *Cell* **2011,** *144* (3), 364-375.

78.   van Breugel, M.; Hirono, M.; Andreeva, A.; Yanagisawa, H.-a.; Yamaguchi, S.; Nakazawa, Y.; Morgner, N.; Petrovich, M.; Ebong, I.-O.; Robinson, C. V.; Johnson, C. M.; Veprintsev, D.; Zuber, B., Structures of SAS-6 Suggest Its Organization in Centrioles. *Science* **2011,** *331* (6021), 1196.

79.   Guichard, P.; Desfosses, A.; Maheshwari, A.; Hachet, V.; Dietrich, C.; Brune, A.; Ishikawa, T.; Sachse, C.; Gönczy, P., Cartwheel Architecture of Trichonymphas Basal Body. *Science* **2012,** *337* (6094), 553.

80.   Guichard, P.; Hamel, V.; Le Guennec, M.; Banterle, N.; Iacovache, I.; Nemčíková, V.; Flückiger, I.; Goldie, K. N.; Stahlberg, H.; Lévy, D.; Zuber, B.; Gönczy, P., Cell-free reconstitution reveals centriole cartwheel assembly mechanisms. *Nature Communications* **2017,** *8* (1), 14813.

81.   Hilbert, M.; Noga, A.; Frey, D.; Hamel, V.; Guichard, P.; Kraatz, S. H.; Pfreundschuh, M.; Hosner, S.; Fluckiger, I.; Jaussi, R.; Wieser, M. M.; Thieltges, K. M.; Deupi, X.; Muller, D. J.; Kammerer, R. A.; Gonczy, P.;

Hirono, M.; Steinmetz, M. O., SAS-6 engineering reveals interdependence between cartwheel and microtubules in determining centriole architecture. *Nat Cell Biol* **2016,** *18* (4), 393-403.

82.   Tang, C.-J. C.; Fu, R.-H.; Wu, K.-S.; Hsu, W.-B.; Tang, T. K., CPAP is a cell-cycle regulated protein that controls centriole length. *Nature Cell Biology* **2009,** *11* (7), 825-831.

83.   Lin, Y.-N.; Wu, C.-T.; Lin, Y.-C.; Hsu, W.-B.; Tang, C.-J. C.; Chang, C.-W.; Tang, T. K., CEP120 interacts with CPAP and positively regulates centriole elongation. *The Journal of Cell Biology* **2013,** *202* (2), 211.

84.   Schmidt, T. I.; Kleylein-Sohn, J.; Westendorf, J.; Le Clech, M.; Lavoie, S. B.; Stierhof, Y.-D.; Nigg, E. A., Control of Centriole Length by CPAP and CP110. *Current Biology* **2009,** *19* (12), 1005-1011.

85.   Lin, Y.-C.; Chang, C.-W.; Hsu, W.-B.; Tang, C.-J. C.; Lin, Y.-N.; Chou, E.-J.; Wu, C.-T.; Tang, T. K., Human microcephaly protein CEP135 binds to hSAS-6 and CPAP, and is required for centriole assembly. *The EMBO Journal* **2013,** *32* (8), 1141-1154.

86.   Comartin, D.; Gupta, Gagan D.; Fussner, E.; Coyaud, É.; Hasegan, M.; Archinti, M.; Cheung, Sally W. T.; Pinchev, D.; Lawo, S.; Raught, B.; Bazett-Jones, D. P.; Lüders, J.; Pelletier, L., CEP120 and SPICE1 Cooperate with CPAP in Centriole Elongation. *Current Biology* **2013,** *23* (14), 1360-1366.

87.   Sharma, A.; Aher, A.; Dynes, Nicola J.; Frey, D.; Katrukha, Eugene A.; Jaussi, R.; Grigoriev, I.; Croisier, M.; Kammerer, Richard A.; Akhmanova, A.; Gönczy, P.; Steinmetz, Michel O., Centriolar CPAP/SAS-4 Imparts Slow Processive Microtubule Growth. *Developmental Cell* **2016,** *37* (4), 362-376.

88.   Zheng, X.; Ramani, A.; Soni, K.; Gottardo, M.; Zheng, S.; Ming Gooi, L.; Li, W.; Feng, S.; Mariappan, A.; Wason, A.; Widlund, P.; Pozniakovsky, A.; Poser, I.; Deng, H.; Ou, G.; Riparbelli, M.; Giuliano, C.; Hyman, A. A.; Sattler, M.; Gopalakrishnan, J.; Li, H., Molecular basis for CPAP-tubulin interaction in controlling centriolar and ciliary length. *Nature Communications* **2016,** *7* (1), 11874.

89.   Gadadhar, S.; Bodakuntla, S.; Natarajan, K.; Janke, C., The tubulin code at a glance. *Journal of Cell Science* **2017,** *130* (8), 1347.

90.   Janke, C., The tubulin code: Molecular components, readout mechanisms, and functions. *The Journal of Cell Biology* **2014,** *206* (4), 461.

91.   Zitouni, S.; Nabais, C.; Jana, S. C.; Guerrero, A.; Bettencourt-Dias, M., Polo-like kinases: structural variations lead to multiple functions. *Nature Reviews Molecular Cell Biology* **2014,** *15*, 433.

92.   Jana, Swadhin C.; Bazan, J. F.; Dias, Mónica B., Polo Boxes Come out of the Crypt: A New View of PLK Function and Evolution. *Structure* **2012,** *20* (11), 1801-1804.

93.   Slevin, Lauren K.; Nye, J.; Pinkerton, Derek C.; Buster, Daniel W.; Rogers, Gregory C.; Slep, Kevin C., The Structure of the Plk4 Cryptic Polo Box Reveals Two Tandem Polo Boxes Required for Centriole Duplication. *Structure* **2012,** *20* (11), 1905-1917.

94.   Guderian, G.; Westendorf, J.; Uldschmid, A.; Nigg, E. A., Plk4 trans-autophosphorylation regulates centriole number by controlling βTrCP-mediated degradation. *Journal of Cell Science* **2010,** *123* (13), 2163.

95.   Cunha-Ferreira, I.; Rodrigues-Martins, A.; Bento, I.; Riparbelli, M.; Zhang, W.; Laue, E.; Callaini, G.; Glover, D. M.; Bettencourt-Dias, M., The SCF/Slimb Ubiquitin Ligase Limits Centrosome Amplification through Degradation of SAK/PLK4. *Current Biology* **2009,** *19* (1), 43-49.

96.   Sillibourne, J. E.; Tack, F.; Vloemans, N.; Boeckx, A.; Thambirajah, S.; Bonnet, P.; Ramaekers, F. C. S.; Bornens, M.; Grand-Perret, T., Autophosphorylation of Polo-like Kinase 4 and Its Role in Centriole Duplication. *Molecular Biology of the Cell* **2009,** *21* (4), 547-561.

97.   Holland, A. J.; Lan, W.; Niessen, S.; Hoover, H.; Cleveland, D. W., Polo-like kinase 4 kinase activity limits centrosome overduplication by autoregulating its own stability. *The Journal of Cell Biology* **2010,** *188* (2), 191.

98.   Rogers, G. C.; Rusan, N. M.; Roberts, D. M.; Peifer, M.; Rogers, S. L., The SCF&Slimb ubiquitin ligase regulates Plk4/Sak levels to block centriole reduplication. *The Journal of Cell Biology* **2009,** *184* (2), 225.

99.   Brownlee, C. W.; Klebba, J. E.; Buster, D. W.; Rogers, G. C., The Protein Phosphatase 2A regulatory subunit Twins stabilizes Plk4 to induce centriole amplification. *The Journal of Cell Biology* **2011,** *195* (2), 231.

100.   Arquint, C.; Gabryjonczyk, A.-M.; Imseng, S.; Böhm, R.; Sauer, E.; Hiller, S.; Nigg, E. A.; Maier, T., STIL binding to Polo-box 3 of PLK4 regulates centriole duplication. *eLife* **2015,** *4*, e07888.

101.   Lopes, Carla A. M.; Jana, Swadhin C.; Cunha-Ferreira, I.; Zitouni, S.; Bento, I.; Duarte, P.; Gilberto, S.; Freixo, F.; Guerrero, A.; Francia, M.; Lince-Faria, M.; Carneiro, J.; Bettencourt-Dias, M., PLK4 trans-Autoactivation Controls Centriole Biogenesis in Space. *Developmental Cell* **2015,** *35* (2), 222-235.

102.   Ohta, M.; Ashikawa, T.; Nozaki, Y.; Kozuka-Hata, H.; Goto, H.; Inagaki, M.; Oyama, M.; Kitagawa, D., Direct interaction of Plk4 with STIL ensures formation of a single procentriole per parental centriole. *Nature Communications* **2014,** *5* (1), 5267.

103.   Yamamoto, S.; Kitagawa, D., Self-organization of Plk4 regulates symmetry breaking in centriole duplication. *Nature Communications* **2019,** *10* (1), 1810.

104.   Kratz, A.-S.; Bärenz, F.; Richter, K. T.; Hoffmann, I., Plk4-dependent phosphorylation of STIL is required for centriole duplication. *Biology Open* **2015,** *4* (3), 370.

105.   Moyer, T. C.; Clutario, K. M.; Lambrus, B. G.; Daggubati, V.; Holland, A. J., Binding of STIL to Plk4 activates kinase activity to promote centriole assembly. *The Journal of Cell Biology* **2015,** *209* (6), 863.

106.   Montenegro Gouveia, S.; Zitouni, S.; Kong, D.; Duarte, P.; Ferreira Gomes, B.; Sousa, A. L.; Tranfield, E. M.; Hyman, A.; Loncarek, J.; Bettencourt-Dias, M., PLK4 is a microtubule-associated protein that self-assembles promoting de novo MTOC formation. *Journal of Cell Science* **2019,** *132* (4), jcs219501.

107.   Wong, Y. L.; Anzola, J. V.; Davis, R. L.; Yoon, M.; Motamedi, A.; Kroll, A.; Seo, C. P.; Hsia, J. E.; Kim, S. K.; Mitchell, J. W.; Mitchell, B. J.; Desai, A.; Gahman, T. C.; Shiau, A. K.; Oegema, K., Reversible centriole depletion with an inhibitor of Polo-like kinase 4. *Science* **2015,** *348* (6239), 1155.

108.   Grimm, J. B.; English, B. P.; Chen, J.; Slaughter, J. P.; Zhang, Z.; Revyakin, A.; Patel, R.; Macklin, J. J.; Normanno, D.; Singer, R. H.; Lionnet, T.; Lavis, L. D., A general method to improve fluorophores for live-cell and single-molecule microscopy. *Nat Methods* **2015,** *12* (3), 244-50, 3 p following 250.

109.   Wang, L.; Tran, M.; D'Este, E.; Roberti, J.; Koch, B.; Xue, L.; Johnsson, K., A general strategy to develop cell permeable and fluorogenic probes for multi-colour nanoscopy. *bioRxiv* **2019**, 690867.

110.   Zheng, Q.; Ayala, A. X.; Chung, I.; Weigel, A. V.; Ranjan, A.; Falco, N.; Grimm, J. B.; Tkachuk, A. N.; Wu, C.; Lippincott-Schwartz, J.; Singer, R. H.; Lavis, L. D., Rational Design of Fluorogenic and Spontaneously Blinking Labels for Super-Resolution Imaging. *ACS Central Science* **2019,** *5* (9), 1602-1613.

111.   Gache, V.; Waridel, P.; Winter, C.; Juhem, A.; Schroeder, M.; Shevchenko, A.; Popov, A. V., Xenopus meiotic microtubule-associated interactome. *PLoS One* **2010,** *5* (2), e9248.

112.   Mikhaylova, M.; Cloin, B. M.; Finan, K.; van den Berg, R.; Teeuw, J.; Kijanka, M. M.; Sokolowski, M.; Katrukha, E. A.; Maidorn, M.; Opazo, F.; Moutel, S.; Vantard, M.; Perez, F.; van Bergen en Henegouwen, P. M.; Hoogenraad, C. C.; Ewers, H.; Kapitein, L. C., Resolving bundled microtubules using anti-tubulin nanobodies. *Nat Commun* **2015,** *6*, 7933.

113.   Kellogg, E. H.; Hejab, N. M. A.; Howes, S.; Northcote, P.; Miller, J. H.; Diaz, J. F.; Downing, K. H.; Nogales, E., Insights into the Distinct Mechanisms of Action of Taxane and Non-Taxane Microtubule Stabilizers from Cryo-EM Structures. *J Mol Biol* **2017,** *429* (5), 633-646.

114.   D'Este, E.; Kamin, D.; Gottfert, F.; El-Hady, A.; Hell, S. W., STED nanoscopy reveals the ubiquity of subcortical cytoskeleton periodicity in living neurons. *Cell Rep* **2015,** *10* (8), 1246-51.

115.   Bucevicius, J.; Keller-Findeisen, J.; Gilat, T.; Hell, S. W.; Lukinavicius, G., Rhodamine-Hoechst positional isomers for highly efficient staining of heterochromatin. *Chem Sci* **2019,** *10* (7), 1962-1970.

116.   Beck, M.; Hurt, E., The nuclear pore complex: understanding its function through structural insight. *Nat Rev Mol Cell Biol* **2017,** *18* (2), 73-89.

117.   Emmett, E. J.; Hayter, B. R.; Willis, M. C., Palladium-catalyzed synthesis of ammonium sulfinates from aryl halides and a sulfur dioxide surrogate: a gas- and reductant-free process. *Angew Chem Int Ed Engl* **2014,** *53* (38), 10204-8.

118.   Rossi, A. M.; Taylor, C. W., Analysis of protein-ligand interactions by fluorescence polarization. *Nature Protocols* **2011,** *6* (3), 365-387.

119.   Farrants, H.; Hiblot, J.; Griss, R.; Johnsson, K., Rational Design and Applications of Semisynthetic Modular Biosensors: SNIFITs and LUCIDs. In *Synthetic Protein Switches: Methods and Protocols*, Stein, V., Ed. Springer New York: New York, NY, 2017; pp 101-117.

120.   Wong, Y. L.; Anzola, J. V.; Davis, R. L.; Yoon, M.; Motamedi, A.; Kroll, A.; Seo, C. P.; Hsia, J. E.; Kim, S. K.; Mitchell, J. W.; Mitchell, B. J.; Desai, A.; Gahman, T. C.; Shiau, A. K.; Oegema, K., Cell biology. Reversible centriole depletion with an inhibitor of Polo-like kinase 4. *Science* **2015,** *348* (6239), 1155-60.

121. Bauer, M.; Cubizolles, F.; Schmidt, A.; Nigg, E. A., Quantitative analysis of human centrosome architecture by targeted proteomics and fluorescence imaging. *The EMBO journal* **2016,** *35* (19), 2152-2166.

122. Habedanck, R.; Stierhof, Y.-D.; Wilkinson, C. J.; Nigg, E. A., The Polo kinase Plk4 functions in centriole duplication. *Nature Cell Biology* **2005,** *7* (11), 1140-1146.

123. Beliu, G.; Kurz, A. J.; Kuhlemann, A. C.; Behringer-Pliess, L.; Meub, M.; Wolf, N.; Seibel, J.; Shi, Z. D.; Schnermann, M.; Grimm, J. B.; Lavis, L. D.; Doose, S.; Sauer, M., Bioorthogonal labeling with tetrazine-dyes for super-resolution microscopy. *Commun Biol* **2019,** *2*, 261.

124. Lawo, S.; Hasegan, M.; Gupta, G. D.; Pelletier, L., Subdiffraction imaging of centrosomes reveals higher-order organizational features of pericentriolar material. *Nature Cell Biology* **2012,** *14*, 1148.

125. Takao, D.; Watanabe, K.; Kuroki, K.; Kitagawa, D. Feedback loops in the Plk4-STIL-HsSAS6 network coordinate site selection for procentriole formation *Biology Open*, 2019.

126. Takao, D.; Yamamoto, S.; Kitagawa, D., A theory of centriole duplication based on self-organized spatial pattern formation. *The Journal of Cell Biology* **2019,** *218* (11), 3537.

127. Yen-Pon, E.; Li, B.; Acebrón-Garcia-de-Eulate, M.; Tomkiewicz-Raulet, C.; Dawson, J.; Lietha, D.; Frame, M. C.; Coumoul, X.; Garbay, C.; Etheve-Quelquejeu, M.; Chen, H., Structure-Based Design, Synthesis, and Characterization of the First Irreversible Inhibitor of Focal Adhesion Kinase. *ACS Chemical Biology* **2018,** *13* (8), 2067-2073.

128. Tang, C.-J. C.; Lin, S.-Y.; Hsu, W.-B.; Lin, Y.-N.; Wu, C.-T.; Lin, Y.-C.; Chang, C.-W.; Wu, K.-S.; Tang, T. K., The human microcephaly protein STIL interacts with CPAP and is required for procentriole formation. *The EMBO Journal* **2011,** *30* (23), 4790-4804.

129. Strnad, P.; Leidel, S.; Vinogradova, T.; Euteneuer, U.; Khodjakov, A.; Gönczy, P., Regulated HsSAS-6 Levels Ensure Formation of a Single Procentriole per Centriole during the Centrosome Duplication Cycle. *Developmental Cell* **2007,** *13* (2), 203-213.

130. Los, G. V.; Encell, L. P.; McDougall, M. G.; Hartzell, D. D.; Karassina, N.; Zimprich, C.; Wood, M. G.; Learish, R.; Ohana, R. F.; Urh, M.; Simpson, D.; Mendez, J.; Zimmerman, K.; Otto, P.; Vidugiris, G.; Zhu, J.; Darzins, A.; Klaubert, D. H.; Bulleit, R. F.; Wood, K. V., HaloTag: a novel protein labeling technology for cell imaging and protein analysis. *ACS Chem Biol* **2008,** *3* (6), 373-82.

131. Piel, M.; Meyer, P.; Khodjakov, A.; Rieder, C. L.; Bornens, M., The Respective Contributions of the Mother and Daughter Centrioles to Centrosome Activity and Behavior in Vertebrate Cells. *The Journal of Cell Biology* **2000,** *149* (2), 317-330.

132. Karch, S.; Broichhagen, J.; Schneider, J.; Böning, D.; Hartmann, S.; Schmid, B.; Tripal, P.; Palmisano, R.; Alzheimer, C.; Johnsson, K.; Huth, T., A New Fluorogenic Small-Molecule Labeling Tool for Surface Diffusion Analysis and Advanced Fluorescence Imaging of β-Site Amyloid Precursor Protein-Cleaving Enzyme 1 Based on Silicone Rhodamine: SiR-BACE1. *Journal of Medicinal Chemistry* **2018,** *61* (14), 6121-6139.

Curriculum Vitae

Aleksandar Salim

Date of birth: 2nd February 1990
Place of birth: Kragujevac, Serbia

Location: 69115 Heidelberg
                   Germany

Phone: +49 176 8414 0757
E-mail: aleksandarsalim@mpimf-heidelberg.mpg.de
LinkedIn: linkedin.com/in/aleksandar-salim-bb2103159/

Education

2015-present	**PhD program- Chemistry and Chemical Engineering** EPFL | École polytechnique fédérale de Lausanne, Switzerland
2013-2015	**Master program**- Molecular and Biological chemistry; EPFL | École polytechnique fédérale de Lausanne, Switzerland GPA: **5.14 (scale 1 to 6)**
2009-2013	**Graduated Chemist**, University of Belgrade, Serbia (4-year system) GPA: **9.75 (scale 6 to 10)**
2005-2009	Course: **Chemical Technician**, Technical high school in Kragujevac, Serbia, GPA: **5.00 (scale 1 to 5)**

Languages

Serbian (Mother tongue)
English (Full Professional Proficiency)
French (A2)
German (Basics)

Academic experience

2015-present	**PhD Thesis.** Project: Fluorogenic probes for live-cell labelling of organelles. Advisor and Co-advisor: Prof. Kai Johnsson & Prof. Pierre Gönczy
2014/2015	**Master Thesis** in laboratory of Prof. Nicolai Cramer. Project: Pd(0)- catalyzed C_{sp2}-H alkylation; Supervisor: Julia Pedroni, ISIC, EPFL (duration: 4 months)
2013/14	**Semester project and Summer intern** in laboratory of Prof. PhD Kai Johnsson, Project: Synthesis and characterization of fluorogenic derivatives of silicon-rhodamine; Supervisor: PhD Luc Reymond, ISIC, EPFL (duration: 3 days a week during semester, plus 2 months)
2012/13	**Diploma thesis and Summer intern** in laboratory of Prof. PhD Eva Freisinger; Title: Spectroscopic characterization of metallothionein Neclu_MT2;

Supervisor; PhD Jens Loebus, Institute of Inorganic chemistry, University of Zurich (duration: 6 months)

2011/12/13	**Student lecturer** of "Zero" Courses of General and Inorganic Chemistry, organized by faculty with the goal to increase knowledge of first year undergraduate chemistry students
2009-present	**Senior assistant and advisor,** before junior assistant at Chemistry educational program at Petnica Science Center, Petnica, Serbia

Publications

Wang, L*; Frei, S. M.*.; <u>Salim, A.</u>*; Johnsson, K., Small-Molecule Fluorescent Probes for Live-Cell Super-Resolution Microscopy. *J Am Chem Soc* **2019,** *141* (7), 2770-2781 *Authors contributed equally

Presentations and Summer schools

29th Aug - 1st Sep 2018	"Development of fluorogenic probes for live-cell labelling of centrioles" – Poster; EMBO Workshop in Chemical Biology
9th-14th Jul 2018	EMBL training course- Super Resolution Microscopy
13th-16th Jan 2016	"Towards fluorogenic probes for live-cell labelling of centrioles" – Poster; NCCR International Symposium in Chemical Biology, Geneva, Switzerland
1st-5th Sep 2014	Summer school of chemical biology, Villar sur Ollon, Switzerland
Aug 28th - Sep 1st 2013	"Spectroscopic characterization of metallothionein Neclu_MT2"- Oral Communication; XII International Symposium on Inorganic Biochemistry, Wroclaw, Poland
Nov 15th 2012	"Spectroscopic characterization of metallothionein Neclu_MT2"- Oral Presentation on student's conference "Researchers' day", Belgrade

Fellowships

2016/2017	PhD fellowship of Boehringer Ingelheim Fonds
2013/14/15	Fellowship of Alfred Werner Foundation for best students in Chemistry Master programs at Swiss universities
2012/13	Fellowship of Fund for young talented students of Republic of Serbia "Dositeja"
2012/13	Fellowship of Hemofarm Foundation for 20 talented students of Serbia
2010/11	Fellowship of Fund "Dragoslav Srejovic" for the best students of Kragujevac

Non-Academic Activities

- Internal PhD representative of Chemical Biology department, MPI for Medical Research, Heidelberg, Germany
- Independent multiple time participations at "Science days" Festival, Europa park, Germany
- Representing Belgrade's Science Festival at "Science Days" Festival, Europa park, Germany
- Mini project leader at S++ summer school of science, Pozega, Croatia
- Workshop for Science communication, Belgrade, Serbia
- Working on Belgrade's Science Festival with team of chemistry department- preparation, presentation and organization of experimental presentation, Belgrade, Serbia
- "Night of Museums"- Involved in preparation and participation in an experimental show of chemistry department- Between Chemistry and Magic, Belgrade, Serbia
- Research's day- involved in preparation and chemistry presentation, Belgrade, Serbia

Personal interests

- Chess
- Philosophy
- Guitar